Magnetic Resonance Imaging and Spectroscopy at ultra high fields

Dissertation zur Erlangung des
naturwissenschaftlichen Doktorgrades
der Bayerischen Julius-Maximilians-Universität Würzburg
vorgelegt von

Thomas Neuberger

aus Miltenberg

Würzburg

2008

Eingereicht am: 26.02.2008

bei der Fakultät für Physik und Astronomie

1. Gutachter: Prof. Peter Jakob

2. Gutachter: Prof. Andrew Webb

der Dissertation.

1. Prüfer: Prof. Peter Jakob

2. Prüfer: Prof. Andrew Webb

3. Prüfer: Prof.Georg Reents

im Promotionskolloquium.

Tag des Promotionskolloquiums: 23.06.2009

Doktorurkunde ausgehändigt am:

Contents

Contents

1 Introduction

Magnetic resonance imaging (MRI) is one of the most important radiological diagnostic methodologies in the clinic. The first image of the human body using MRI was conducted only 30 years ago by Damadian, Goldsmith, and Minkoff. The experiment time for the 'crude' image which they acquired on 'Indomitable', their home built scanner took almost five hours (see Figure 1.1).
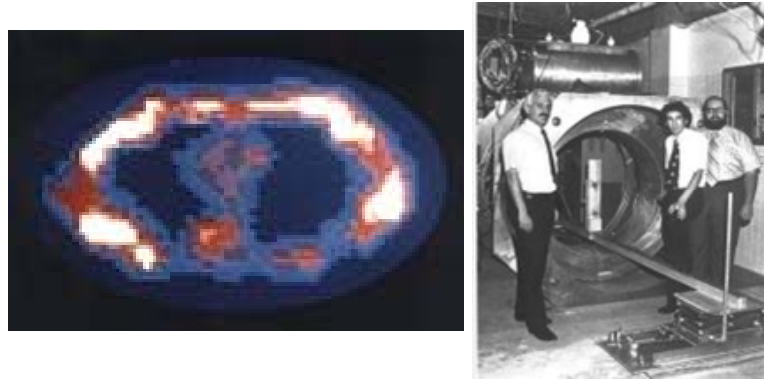
Figure 1.1: First Image from a human body (left) acquired by Damadian and co-workers 1977 in the first human scanner 'Indomitable'. Right: Dr. Damadian, Dr. Minkoff, and Dr. Goldsmith (left to right) in front of the scanner. (source: www.FONAR.com)

Since then major improvements in hardware and sequence development have improved the image quality and reduced the data acquisition time by several orders of magnitude. These improvements continue to evolve, with magnetic field strengths increasing every year.

Besides anatomical images, other applications such as measuring the blood flow, and perfusion, dynamic imaging of heart motion, and many more techniques have been implemented and are now used in today's clinical routine.

Because of the non-invasive character and the unique possibilities of MRI an increasing number of animal studies (especially studies conducted in rodents) are performed in preclinical studies leading to an even higher demand in spatial resolution because of the size of the observed object.

Introduction

Large numbers of academic and commercial laboratories are involved in the development of new hardware, processing algorithms and applications. Studies can be performed on size-scales ranging from humans to single neurons. One factor linking many recent developments in MRI is the continued trend towards higher magnetic fields. As shown in Figure 1.2 MRI now spans almost the entire radiofrequency spectrum and ranges from 4.2 up to 750 MHz. The benefits and the challenges of the very high fields are the basis of the work presented in this thesis, with all experiments being performed on systems operating at 500 MHz or 750 MHz, the highest commercially available frequency for MRI studies on animals.
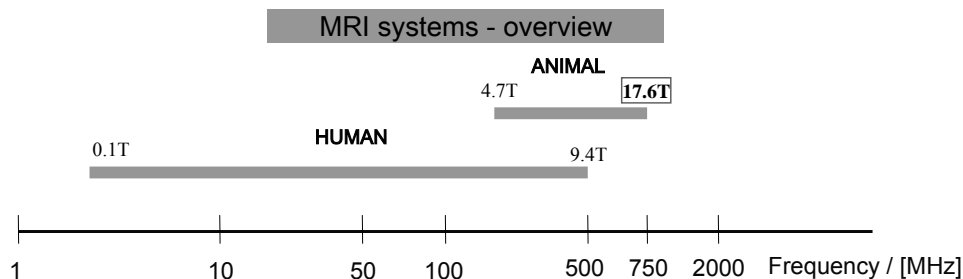
Figure 1.2: Operating frequencies of human and animal MRI systems. The corresponding static magnetic field strengths are given in Tesla.

To cover a wide range of applications three major magnetic resonance techniques were explored: Sodium magnetic resonance spectroscopic imaging (MRSI), proton magnetic resonance spectroscopy (MRS) and proton MRI.

The main advantages of high field NMR are the enhanced signal to noise ratio (SNR) and the increased spectral resolution.

The three specific advantages of high field that were utilized in this thesis are:

- the dramatically increased T2* contrast from iron-loaded contrast agent,

- the increased SNR and spectral resolution for localized NMR spectroscopy, and

- the increased SNR for quadrupolar nuclei such as sodium.

To show the possibilities and to determine the limits of very high fields proton MRI was used to explore the lower limit of detectable iron labeled stem cells in the living rat brain at 17.6 tesla. The importance of this method in the emerging field of stem cell research becomes obvious if the non invasive character of MRI to track/detect the labeled stem cells is considered. There are more than 2000 research papers on embryonic and adult stem cells being published every year (The UK Stem Cell Foundation). Stem cells can be divided in two major categories the embryonic and the adult stem cells. While the embryonic stem cells can differentiate in any cell of the body, the adult stem cells are already differentiated and do not have this ability. The embryonic stem cells have not jet found their way into the clinic, adult stem cells are already been used to treat diseases like leukemia or heart disease.

In this work embryonic stem cells were labeled with very small super paramagnetic iron oxide particles (VSOP). The iron oxide particles lead to a reduction of the MRI signal intensity and the stem cells can therefore be detected. Unlike in other studies, where usually thousands of cells were injected, in this work the smallest number of cells injected stereotactically into the striatum of the rat brain in vivo was 20. Significant hypo intense signal changes were measured after injecting 100 labeled stem cells. In the case of 20 cells the result was not unambiguous. Nevertheless, these results show that it is possible to detect very small numbers of labeled stem cells in vivo. This result was made possible due to the fact that the high static magnetic field (17.6 tesla) enhances the effect of signal reduction in the labeled cells and the surrounding tissue compared to lower static magnetic field strengths.

In vivo proton magnetic resonance spectroscopy (MRS), where spectra are obtained from specific regions in the observed tissue is the second topic of this work. Although it never gained the same importance as MRI in medical diagnosis it delivers a lot of spectroscopic information from insight the body and provides for example information about metabolites such as creatine or GABA. It is used for example to characterize neurological diseases by varying metabolite concentrations or lactate in cancerous regions. The major problems of MRS are the low concentrations of the observed metabolites. While the water concentra-

tion, used in MRI, is roughly 50 M the concentrations of the metabolites is in the millimolar range. As the major in vivo metabolites are located in a small spectral window of roughly 5 ppm, overlap of the resonances is a second problem of MRS. Higher magnetic fields will increase the spectral range and the SNR. Besides those benefits substantial problems arising from higher magnetic field strengths will be discussed. In this work the feasibility of in vivo proton MRS at 17.6 tesla will be shown in rat and mouse brains and the T1 times of the major brain metabolites will be measured at 11.7 as well as at 17.6 tesla. A method to measure T2 of the metabolites independently of the scanner will be presented.

The main focus of this work lies on sodium magnetic resonance spectroscopic imaging (MRSI). MRSI combines MRI and MRS. It provides a spectrum in each image voxel. Therefore, it is possible to create as many images as spectral points are acquired. One may ask the question why use MRSI for sodium, as a sodium spectrum usually has only one resonance? The reason lies in the necessary short echo time provided by the used MRSI sequence. Details will be discussed later.

Measuring the sodium distribution can be used to determine cell integrity and it has been used, therefore, to determine cancerous areas and stroke in animals as small as rats. In this study sodium imaging of the rat and the mouse brain and the mouse heart were explored. A further application of sodium MRSI is shown by monitoring kidney homeostasis in mice. Although the sodium MR signal is much weaker than the proton one, the use of very high static magnetic field and the construction of our own detectors made the presented studies possible. Due to insufficient SNR at lower field strengths previously unimaginable sodium imaging of mice was performed for the first time.

2   Theory

To perform an MRI experiment the subject is placed inside a most of the times superconducting magnet, which produces a static magnetic field. Atoms with a non-zero nuclear magnetic moment can be detected using MRI. Commonly used nucleii are listed in Table 2.1. Due to the high concentration of water in the body the most obvious atom used in MRI is the proton. This charged particle with angular momentum can be considered as acting as a small magnet, aligning either parallel or anti- parallel to the direction of the static magnetic field. From one million protons about one more is aligned in the parallel than in the anti-parallel state. The protons precess around the direction of the static magnetic field, in an analogous way to a spinning gyroscope under the influence of gravity. The frequency of precession is proportional to the strength of the static magnetic field.

Application of a weak radiofrequency (RF) field causes the protons to precess coherently, and the sum of all of the protons precessing is detected as an induced voltage in a tuned detector coil. Spatial information is encoded into the image using magnetic field gradients. These impose a linear variation in all three dimensions in the magnetic field. As a result, the precessional frequencies of the protons are also linearly dependent upon their spatial location. The frequency and phase of the precessing magnetization is measured by the RF coil, and the analog signal is digitized. An inverse two-dimensional Fourier transform is performed to convert the signal into the spatial domain to produce the image. By varying data acquisition parameters, differential contrast between soft-tissues can be introduced

2.1 Proton in a magnetic field

The proton with a nuclear spin of I = ½ has two nuclear energy levels (Zeemann splitting) as derived from quantum mechanical theory [1] when it is placed in a magnetic field. The two levels are characterized by magnetic quantum numbers m = ± ½. The anti-parallel aligned level has a higher energy than the parallel level (see Figure 2.1) and the energy gap between the levels is given by:

$$\Delta E = \frac{\gamma h B_0}{2\pi} \tag{2.1}$$

where h is Planck`s constant (h = 6.60×10^{-34} Js) and γ is a nucleus-specific constant called the gyromagnetic ratio. Examples of γ for different nuclei are shown in Table 2.1.

Energy

$$E = + \frac{\gamma h B_0}{4\pi}$$

antiparallel
m = + 1/2

ΔE

parallel
m = - 1/2

$$E = - \frac{\gamma h B_0}{4\pi}$$

$B_0 = 0$ $B_0 \neq 0$
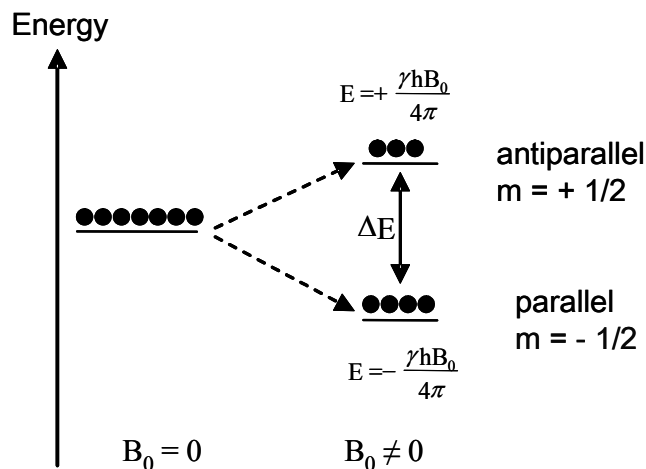
Figure 2.1: Proton (spin ½ nucleus) in a magnetic field B_0. There are slightly more protons in the "parallel state" with a lower energy compared to the anti- parallel state.

Isotope	Spin	γ in MHz/T	Frequency at 17.6T	natural abundance (%)
^{1}H	1/2	42.58	750	99.985
^{2}H	1	6.54	115	0.015
^{13}C	1/2	10.71	189	1.108
^{19}F	1/2	40.08	706	100
^{23}Na	3/2	11.27	198	100
^{31}P	1/2	17.25	304	100
^{39}K	3/2	1.99	35	4.672

Table 2.1: NMR properties of the most common nuclei in *in vivo* NMR

In order to stimulate transitions between the two energy levels, a magnetic field must be applied which has a frequency component given by:

$$\frac{h\omega}{2\pi} = \frac{\gamma h B_0}{2\pi} \tag{2.2}$$

$$\omega = \gamma B_0 \tag{2.3}$$

To calculate the relative number of nuclei in each energy level the Boltzmann equation can be used:

$$\frac{N_{anti-parallel}}{N_{parallel}} = \exp\left[-\frac{\Delta E}{kT}\right] = \exp\left[-\frac{\gamma h B_o}{2\pi kT}\right] \tag{2.4}$$

where k is the Boltzmann coefficient (1.38×10^{-23} J/K), and T is the temperature in Kelvin. With the approximation $e^{-x} \approx 1-x$, the net magnetization M_0 of the object is given by:

$$M_0 = \mu_z(N_{parallel} - N_{anti-parallel}) \tag{2.5}$$

$$M_0 = \frac{\gamma^2 h^2 B_0 N_s}{16\pi^2 kT} \tag{2.6}$$

(N_s: number of all spins in the sample)

This equation shows the dependence of the static magnetic field B_0 and the equilibrium magnetization. The higher B_0 the greater the equilibrium magnetization and therefore the higher the MR signal, as will be shown later.

The classical description of a proton in an external magnetic field B_0 shows that it precesses around the axis of B_0 due to the magnetic moment $\vec{\mu}$, at an angle θ to B_0, and a frequency ω which is proportional to the strength of B_0. This precession frequency is termed the Larmor frequency and Equation 2.3 is referred to as the Larmor equation.

2.2 Excitation

All the protons precess around B_0. They are randomly oriented around a cone and the lack of coherence results in a cancellation of all components of the magnetization in the xy – plane. The resulting net magnetization is denoted by M_0. It can be shown that application of a linearly polarized oscillating electromagnetic field (B_1) with a duration τ_{B1} at the Larmor frequency rotates the net magnetization M_0 towards the xy - plane. The resulting magnetization M_{xy} can be written as:

$$M_{xy} = M_0 \sin(\gamma B_1 \tau_{B1}) \tag{2.7}$$

where,

$$\alpha = \gamma B_1 \tau_{B1} \tag{2.8}$$

is the rotation angle of M_0 towards the xy - plane. The rotating xy component of the net magnetization induces a voltage U_{ind} in the radio frequency resonator:

$$U_{ind} = -\frac{d}{dt} \int \vec{B}_1(\vec{r}) \vec{M}_{xy}(\vec{r}) dV \tag{2.9}$$

which is then recorded by the NMR spectrometer.

2.3 Relaxation

Each of the magnetization components M_z, M_x and M_y must return to their thermal equilibrium values over time. The time-evolutions of M_z, M_x and M_y are characterized by differential equations, known as the Bloch equations [2]:

$$\frac{dM_x(t)}{dt} = \gamma \left(M_y(t) B_z(t) - M_z(t) B_y(t) \right) - \frac{M_x(t)}{T_2} \tag{2.10}$$

$$\frac{dM_y(t)}{dt} = \gamma (M_z(t) B_x(t) - M_x(t) B_z(t)) - \frac{M_y(t)}{T_2} \tag{2.11}$$

$$\frac{dM_z(t)}{dt} = \gamma (M_x(t) B_y(t) - M_y(t) B_x(t)) - \frac{M_z(t) - M_0}{T_1} \tag{2.12}$$

where T1 is the longitudinal or spin- lattice relaxation time and T2 is the transverse or spin- spin relaxation time. T1 describes the return of the equilibrium

(longitudinal) magnetization after an rf - pulse. Energy is transferred from the spins to the surrounding lattice. During T2 relaxation no net energy is transferred. Spins exchange energy between themselves causing a decrease in phase coherence which results in a loss off transverse magnetization.

Relaxation in general can be described as transitions induced by fluctuating magnetic fields, e.g. from the environment (lattice), oscillating close to the Larmor frequency. These dipole- dipole interactions where a magnetic moment of one spin affects the local field of another are the main sources of fluctuating magnetic fields and therefore for relaxation. The corresponding relaxation theory is generally referred to as Bloembergen- Purcell- Pound (BPP) theory [3]. To describe the behavior of the fluctuating magnetic field a correlation function $G(\tau)$ which describes an average over all spins in a macroscopic part of the sample as a function of time τ is given by:

$$G(\tau) = <B_{loc}(t)B_{loc}(t+\tau)>$$ (2.13)

where $B_{loc}(t)$ is the local magnetic field at time t. At short τ the local magnetic field does not change much and therefore the ensemble average will be large (i.e. high correlation). Due to Brownian motion and molecular tumbling the local magnetic field changes rapidly and G(t) decrease very quickly with longer τ. Therefore G(t) is usually taken as a decaying exponential:

$$G(\tau) = G(0)e^{-\frac{|\tau_c|}{\tau}}$$ (2.14)

where τ_c is the correlation time.

After Fourier transformation a spectral density function $J(\omega)$ results:

$$J(\omega) = \int_{-\infty}^{\infty} G(\tau)e^{-i\omega\tau}d\tau = \frac{2\tau_c}{1+\omega_0^2\tau_c^2}$$ (2.15)

By considering two spins (I = ½) the quantum mechanical calculations of Solomon [4] resulted in an analytical expression for dipolar longitudinal relaxation:

$$\frac{1}{T1} = \frac{3}{10}\frac{\gamma^4 h^2}{4\pi^2 r^6}\left(\frac{\tau_c}{1+\omega^2\tau_c^2} + \frac{4\tau_c}{1+4\omega^2\tau_c^2}\right)$$ (2.16)

where r is the distance between the two spins.

The relation between the relaxation time T1 and the spectral density function is shown in Equation 2.17:

$$\frac{1}{T1} = \frac{3}{10}\frac{\gamma^4 h^2}{4\pi^2 r^6}\left(J(\omega) + 4J(2\omega)\right) \tag{2.17}$$

Calculation of T2 yields:

$$\frac{1}{T2} = \frac{3}{20}\frac{\gamma^4 h^2}{4\pi^2 r^6}\left(3J(0) + 5J(\omega) + 2J(2\omega)\right) \tag{2.18}$$

These results led to the following conclusions for dipole-dipole relaxation:

- T1 relaxation is affected by the local magnetic field oscillating at the Larmor and twice the Larmor frequency
- T2 is in addition affected by low- frequency components
- in the case of very fast rotational motion: $\omega^2\tau_c^2 \ll 1$; T1 becomes equal to T2 (e.g.: fluids)
- in the case of very slow motion: $\tau_c < 10^{-9}$ s; T2 becomes very short (e.g.: solids) (see Figure 2.2)
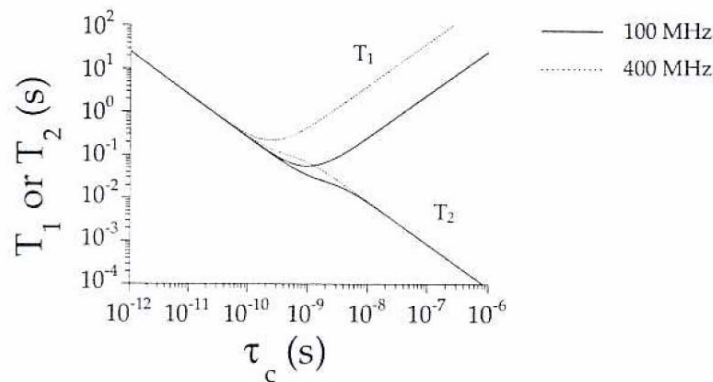
Figure 2.2: The dependence of the longitudinal and transversal relaxation times T1 and T2 as a function of the correlation time τ_c for two external magnetic fields. (taken from [5]).

- T1 relaxation shows a strong dependence on ω and therefore on the static magnetic field B_0 where $\tau_c < {\sim}10^{-7}$ s
- T2 shows virtually no dependence on B_0. (see Figure 2.3)
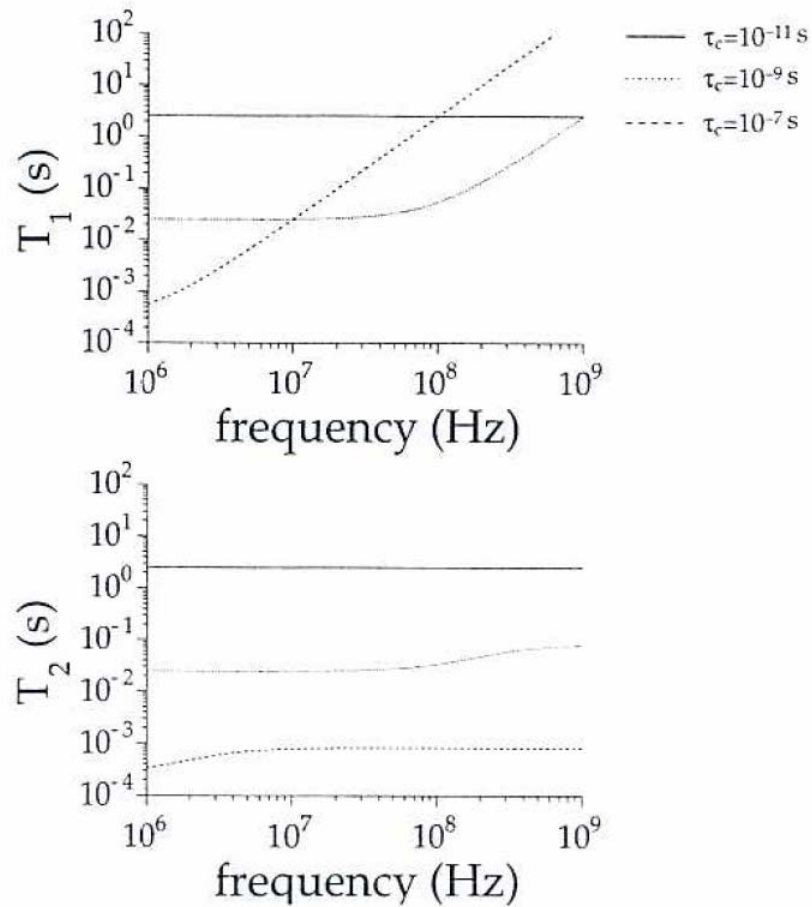
Figure 2.3: B_0 dependency of T1 and T2 for slow ($\tau_c = 10^{-7}$ s) and intermediate ($\tau_c = 10^{-9}$ / 10^{-11} s) rotational processes. Only pure dipole – dipole interaction is considered. (taken from [5]).

Additional transverse relaxation occurs if B_0 field inhomogeneities, i.e. locally different B_0`s, are present. The so-called T2* relaxation time is defined as:

$$\frac{1}{T2^*} = \frac{1}{T2} + \gamma \Delta B_0 \qquad (2.19)$$

where $\gamma \Delta B_0$ represents B_0 inhomogeneities. This effect is particularly useful to identify injected iron particles, which produce large B0 inhomogeneities, in the MRI image as will be seen later.

2.4 NMR Signal

The transverse magnetization after excitation by a flip angle α is a sinusoidal wave which is damped by T2*:

$$M_{xy}(t) = M_0 \sin\alpha \cdot e^{\left(i\omega_0 t - \frac{t}{T2^*}\right)}$$
(2.20)

If averaging has to be applied and the repetition time (TR) between two transitions is shorter than five times T1, saturation effects can not be neglected. After a few transitients as shown in [6] the system is in a steady state and the transverse magnetization ($M^{ss}_{xy}(t)$) can be written as [7]:

$$M^{ss}_{xy}(t) = M_0 \frac{1 - e^{-\frac{TR}{T1}}}{1 - \cos\alpha \cdot e^{-\frac{TR}{T1}}} \sin\alpha \cdot e^{\left(i\omega_0 t - \frac{t}{T2^*}\right)}$$
(2.21)

To achieve the highest signal the optimum flip angle for a given TR should be chosen. This so - called Ernst angle can be written as [8]:

$$\alpha_{ERNST} = \arccos \cdot e^{-\frac{TR}{T1}}$$
(2.22)

The signal in the time domain, the "Free Induction Decay (FID)" is:

$$s(t) = M \cdot e^{\left(i\omega_0 t - \frac{t}{T2^*}\right)}$$
(2.23)

where M represents the transverse magnetization. After Fourier transformation the signal in the frequency domain is:

$$s(\nu) = \int_0^\infty M \cdot e^{\left(i\omega_0 t - \frac{t}{T_2^*}\right)} e^{-i\omega t} dt = \frac{M}{1/T_2^* + i \cdot 2\pi(\nu - \nu_0)}$$
(2.24)

2.5 Signal to Noise Ratio (SNR)

The standard deviation of the noise voltage (Johnson noise) in an NMR experiment can be written in the time domain as:

$$\sigma_t = \sqrt{4kT_{RFR}R_{RFR}BW}$$
(2.25)

T_{RFR} and R_{RFR} are the temperature and the resistance of the rf – resonator and sample, and BW is the band width of the acquired signal. The SNR of a NMR experiment in the time domain is therefore defined as the first point of the FID divided by σ_t:

$$SNR_t = \frac{s(t=0)}{\sigma_t} \tag{2.26}$$

In the frequency domain the SNR is the maximum amplitude of a resonance divided by the standard deviation of the noise in the spectrum [9]:

$$SNR_\upsilon = \frac{s(\upsilon_0)}{\sigma_\upsilon} \tag{2.27}$$

A similar definition is used when the SNR of an image is determined. In this case the average signal from a region of interest (ROI) is divided by the standard deviation of the noise. A correction for magnitude images has to be applied: for Gaussian noise the correction factor is 0.655 [10]. Another common way to define the SNR in images is the ratio between the averaged signal intensity of a ROI and its standard deviation.

2.6 Chemical Shift

The electrons surrounding a nucleus produce a magnetic field which is in the opposite direction to B_0. This field, which is proportional to the static magnetic field B_0, shields the nucleus from B_0 and the resonance frequency of the nucleus changes slightly depending on the strength of the additional field. Nuclei in different chemical environments have distinct but different resonance frequencies. The effective magnetic field at the nucleus is described by:

$$B = B_0(1-\sigma) \tag{2.28}$$

where σ is the shielding constant. In this way different molecules can be identified in a NMR spectrum. As the frequency shifts are usually very small σ is measured in parts per million (ppm). For *in vivo* proton NMR spectroscopy all the peaks that occur in a spectrum are in the range of about 12 ppm.

2.7 Magnetic field gradients and a MRI experiment

Three separate gradient coils are required to encode unambiguously the three spatial dimensions in an MRI experiment. Since only the z-component of the magnetic field interacts with the proton magnetic moments, it is the spatial variation in the z-component of the magnetic field which is important.

Assume a linear gradient field applied in z- direction. The resulting magnetic field in z direction is:

$$B_z = B_0 + zG_z \tag{2.29}$$

and the corresponding precessional frequencies (ω_z) of the protons, as a function of their position in z, is given by:

$$\omega_z = \gamma B_z = \gamma(B_0 + zG_z) \tag{2.30}$$

where G_z is given in units of T/m. In a rotating reference frame the precessional frequency is:

$$\omega_z = \gamma z G_z \tag{2.31}$$

If analogous gradients are applied in the x and y direction the spatial dependence of the resonant frequencies is provided.

In general a MRI experiment can be divided in three parts, slice selection, phase-encoding and frequency-encoding.

- slice selection: The combination of a frequency selective 90° pulse and the slice gradient selectively excites protons within a thickness given by:

$$\Delta z = \frac{\Delta \omega_z}{\gamma G_{slice}} \tag{2.32}$$

  where $\Delta \omega$ is the frequency bandwidth of the pulse

- phase encoding: The phase encoding gradient G_{phase} imparts a spatially dependent phase shift into the signal.

- frequency encoding: During data acquisition the frequency encoding gradient generates a spatially dependent precessional frequency in the acquired signal.

Figure 2.4 shows as an example a gradient echo imaging sequence [11].
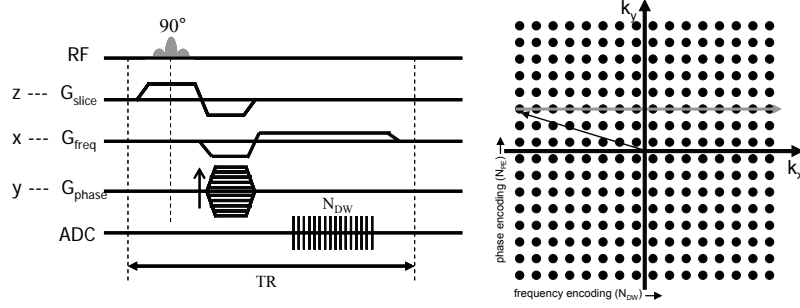
Figure 2.4: Basic scheme for a gradient-echo imaging sequence. The experiment is re-peated until all phase encoding gradient steps N_{PE} are scanned. The acquisition matrix is N_{DW} x N_{PE} data points, where N_{DW} is the number of points acquired in the frequency direc-tion (see right).

The detected signal can be written as:

$$s(G_x, t, G_y, \tau_{PE}) \propto \iint \rho(x, y) e^{-i\gamma G_x x t} e^{-i\gamma G_y y \tau_{PE}} dx dy \qquad (2.33)$$

and by introducing the k-space formalism [12]:

$$S(k_x, k_y) \propto \iint \rho(x, y) e^{-i2\pi k_x x} e^{-i2\pi k_y y} dx dy \qquad (2.34)$$

with:

$$k_x = \frac{\gamma}{2\pi} G_x t \qquad\qquad k_y = \frac{\gamma}{2\pi} G_y \tau_{PE} \qquad (2.35)$$

Applying an inverse two dimensional Fourier transformation results in the re-constructed image:

$$\rho(x, y) \propto \iint S(k_x, k_y) e^{i2\pi k_x x} e^{i2\pi k_y y} dk_x dk_y \qquad (2.36)$$

The field of view (FOV) of the image is defined by the distance between adja-cent k- space lines:

$$FOV_{x/y} = \frac{1}{\Delta k_{x/y}} \qquad (2.37)$$

and the resolution by the maximum gradient strength:

$$\Delta x = \frac{1}{N_x \Delta k_x} = \frac{1}{k_{x,\max}} \qquad\qquad \Delta y = \frac{1}{N_y \Delta k_y} = \frac{1}{k_{y,\max}} \qquad (2.38)$$

While all N_x data points in the frequency encoding direction are acquired in one transient, to record all phase encoding steps necessary for the reconstruction of the image the experiment has to be conducted N_y times with varying gradient strength from $-k_{y,max}$ to $+k_{y,max}$ in the G_y direction. A three dimensional image can be acquired by applying a phase encoding instead of slice selection in the third direction, followed by a three dimensional inverse Fourier transformation.

2.8 The MRS experiment

Unlike imaging MRS provides information about metabolite concentrations in localized areas. In order to obtain a spectrum only from a region of interest (ROI), three orthogonal gradients must be used.
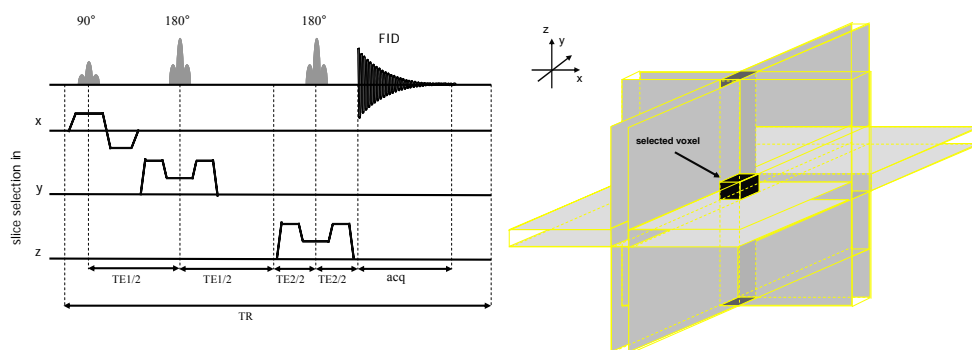
Figure 2.5: Point ReSolved Spectroscopy (PRESS) sequence. Each combination of an RF – pulse and gradient selects a plane in the object. The result is detected transverse magnetization at the intersection of the three planes.

Figure 2.5 shows the Point ReSolved Spectroscopy (PRESS) [13] pulse sequence which will be used later on in this work. The gradient in the x direction during the frequency selective pulse with a flip angle of 90 degree can be considered as initial slice selection followed by two frequency selective 180 degree pulses selecting slices in the remaining two dimensions. The additional gradients adjacent to the 180 degree pulses are used to eliminate unwanted signal arising from imperfections of the pulses. In this way each pulse selects a plane and the result is a spectrum from a voxel of interest. Fourier transformation of the acquired time domain signal results in the localized spectrum.

In the following some important details concerning MRS (most of which have direct analogies in MRI) are discussed:

Signal processing

Manipulation of the time domain signal prior to Fourier transformation is often performed to improve the SNR or the spectral resolution. A commonly used technique is multiplication of the time domain signal with a certain function (e.g. exponential, Gaussian function). By using an exponential weighting function on a FID signal for example, the SNR of the final spectrum will increase since the noise containing parts in the last section of the time domain signal will be suppressed. The trade off will be a broader line width of the resonances. Studies of the appropriate window function and the most commonly used functions can be found in [8][14]. An example of exponential filtering applied to a spectrum achieved from a rat brain is shown in Figure 2.6.
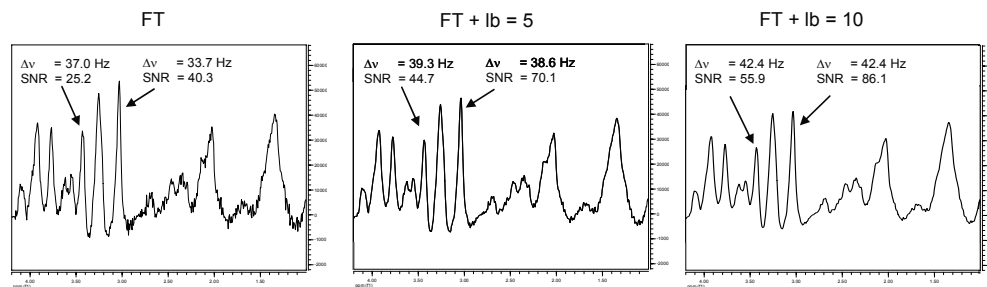
Figure 2.6: Effect of an applied exponential filter (signal in time domain multiplied by exp(-t/lb); lb is the filter width) on spectral resolution and signal-to-noise. Both, the line width and the SNR increase. While the increase in SNR is beneficial, the increase in line width may make previously, without filtering, resolved resonances indistinguishable.

Another useful tool to enhance the spectral quality is called "zero filling". In this technique a number of zeroes are added to the end of the time domain signal. Zero filling by a factor of two improves the spectral quality and the resonances can be seen more clearly. An example is shown in Figure 2.7. However, it should be stressed that zero filling does not add any new information to the acquired data.
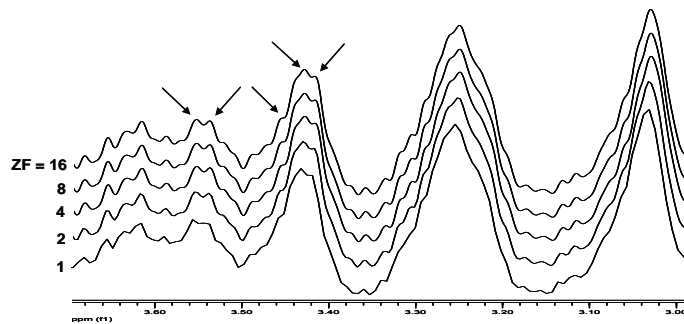
Figure 2.7: Zero filling applied to a single voxel spectrum from a mouse brain. The resonances marked with arrows are more distinguishable after applying zerofilling with a factor of two. Additional zero filling does not improve the spectral resolution.

J - Coupling

Besides dipolar spin-spin interactions between nuclei a second coupling mechanism through chemical bonds (scalar coupling) leads to the splitting of a resonance line into several smaller ones. This scalar or 'J – coupling' is the interaction of the magnetic nuclear moments through the much larger electronic magnetic momentum of the electrons in chemical bonds. The splitting of the lines is independent of the static magnetic field B_0, and the J coupling constant for proton NMR is usually between 1 and 15 Hz. An example is given in Figure 2.8 where the splitting for gamma aminobutric acid the main inhibitory neurotransmitter in the brain of all vertebrates is shown. More information about J – coupling can be found in [15].
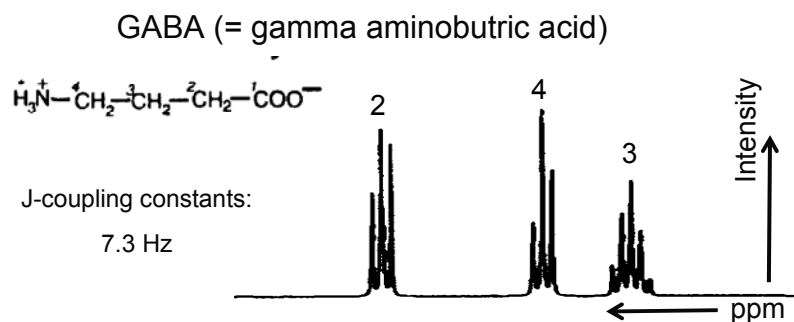
Figure 2.8: J – coupling of .gamma aminobutric acid. For example: the protons at the 4 - C atom have two neighboring protons (at the 3 – C atom) and will therefore split into 2 +1 lines with the binomial intensity distribution of 1:2:1. The distance between the peaks is the J – coupling constant of 7.3 Hz in this case.

Water suppression

Since metabolites *in vivo* have usually a concentration of a few millimol/l, which is four orders of magnitude smaller than the water concentration (50 mol/l), a water suppression technique is usually applied prior to the spectroscopic sequence to be able to use the full dynamic range of the receiver and to detect the resonances of the metabolites at all. There are several possibilities to achieve the water suppression. Among the first water suppression methods a combination of short block pulses interleaved with delays resulting in a sinusoidal excitation profile in the frequency domain was used. By choosing the right delays only the metabolites and not the water signal are excited [16], [17]. Other methods which selectively dephase the water signal while the signal from the metabolites of interest is rephased during a spin echo period are WATERGATE [18], MEGA [19] or excitation sculpting [20]. A third approach is the selective excitation of the water signal followed by coherence destruction using B_0 field gradients. This sequence was first described by Haase et al. and is called CHESS (CHEmical Shift Selective imaging) [21]. Derivatives thereof are DRYSTEAM [22], VAPOR [23] or DRYPRESS [24].

A recent approach shows metabolite spectra from the rat brain acquired without water suppression. In this case the water signal was modeled and removed by the matrix pencil method [25].

Artifacts in MRS

The main errors sources at high fields are summarized below. A general overview of artifacts in clinical proton MRS can be found in [26].

Chemical shift artifact

Since spins from nuclei in a different chemical environment have slightly different resonance frequencies, this results in the acquisition of metabolite spectra from voxels that are shifted by:

$$\Delta x_{ChemicalShift} = \frac{\omega_{meta1} - \omega_{meta2}}{\gamma G_x} \tag{2.39}$$

where G_x is the gradient strength for slice selection and $\omega_{meta1/2}$ are the resonance frequencies of the two different metabolites. An overview and an example of the "chemical shift artifact" for MRS experiments are shown in Figure 2.9.

Theory

In MRI the same artifact can be seen in the frequency encoding and slice selection direction, leading to a spatial shift of the fat containing tissue compared to the water containing tissue.

Resonance frequency (B$_0$ = 17.6 T) = 750 MHz
Maximum gradient strength = 200 mT/m

Example:

Voxel size:	3 mm
Used gradient strength:	29.6 %
Maximum gradient strength:	200 mT/m
(H20 – NAA) resonance:	(4.7 – 2.0) ppm

Chemical shift displacement: $\Delta x = \dfrac{(4.7 - 2.0) * 750 \text{ MHz}}{0.2 * 0.296 \text{ T/m} * 42.58 \text{ MHz/T}}$

$\Delta x = 0.8$ mm
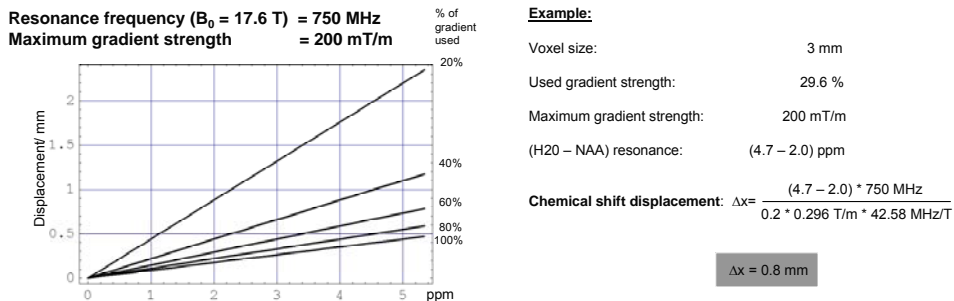
Figure 2.9: Chemical shift artifact. Due to the slightly different resonance frequencies of the nuclei in different metabolites resulting from the shielding of the electrons, spectra from shifted voxels are acquired for each metabolite.

Radiation Damping

The phenomenon of radiation damping occurs especially at high static magnetic fields B$_0$. The induced voltage U$_{ind}$ in the RF resonator produces a B$_{rd}$ – field which interacts with the magnetization and forces M$_{xy}$ to nutate back towards the z plane. This produces phenomena such as unexpected echoes, signal peak heights that are proportional to the flip angle and signal peaks which can not be phased are just some examples of radiation damping. An overview of radiation damping can be found in [26] [28]. One method to reduce or avoid radiation damping is detuning of the RF resonator, as shown in [29].

Eddy currents

The major source of eddy currents is the fast gradient switching. Special efforts have to be taken to adjust the pre-emphasis, the gradient switching control of each NMR system. Eddy currents lead to asymmetric line shapes in the spectrum and/or signal drop. Within certain limits the effect of eddy currents on the line shape can be compensated by using reference spectra to calculate phase corrections [30][31][32]. Another way of correction is the use of a general line shape function in the data fitting model [33].

2.9 Spectroscopic imaging

Spectroscopic imaging is a combination of the before mentioned methods. Though it does not reach the resolution of images acquired from water protons, it provides maps from single resonances (metabolites). The most common spectroscopic imaging methods are based on chemical shift imaging (CSI). In the three dimensional case, after an excitation pulse, phase encoding is applied in all three spatial dimensions followed by the acquisition of the FID. The basic pulse sequence is shown in Figure 2.10.
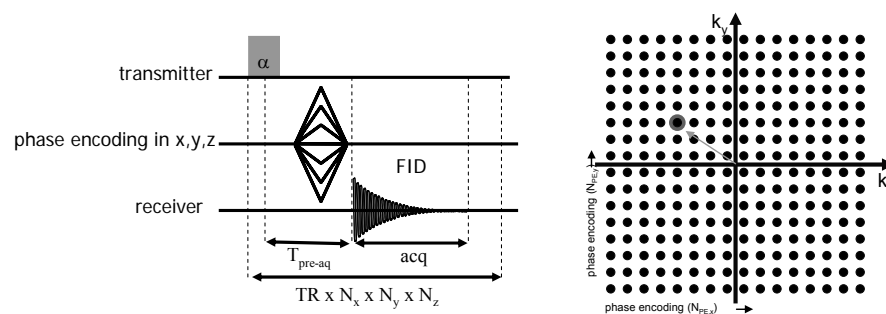
Figure 2.10: Chemical Shift Imaging sequence. Phase encoding is conducted in all three directions. The right image shows a two dimensional acquisition scheme of CSI. Each transient acquires only one point in k- space.

The biggest advantages of CSI experiments are:

- no chemical shift artifact, as there is no gradient during excitation or acquisition
- acquisition of multi voxel spectra covering a large ROI
- very short delay after excitation before the acquisition (pre acquisition delay: T_{pre-aq}). This is essential if resonances with short relaxation times are to be detected (e.g. sodium).

The biggest trade-off is the long acquisition time since every point in k- space has to be acquired in a different transient and the total experimental time is: T_{exp} = ($N_{PE,x}$ x $N_{PE,y}$ x $N_{PE,z}$ x TR). Nevertheless, if averaging has to be applied in a MRS experiment due to the low SNR of the achieved spectra, CSI is an effective strategy as it yields spectra from multiple voxels in the same time. The low resolution of the reconstructed images can lead to partial volume effects depending on the size of the investigated subject.

Another serious problem of CSI is the low number of sampling points in each direction of k- space resulting in artifacts in the reconstructed image. The Fourier transform of a time domain signal S(k), sampled at discrete points w(k) results in a convolution of S(k) and w(k). A one dimensional example of only eight phase encoding steps is shown in Figure 2.11.

The point spread function (PSF) [9] is the Fourier transform of the sampling grid and can be written as:

$$PSF(x_n, x_0) = \frac{\sin(\pi(x_n - x_0)/\Delta x)}{N \sin(\pi(x_n - x_0)/N\Delta x)}$$

(2.40)

where Δx is the spatial resolution. The PSF represents the propagation of a signal from point x_0 in the object to all points x_n in the image. It is a discrete function with N points. Keeping x_n fixed the continuous function is called the spatial response function (SRF) [7], [34], [35] and shows the contribution of each point from the object to the spectrum of a point x_n in the image. To avoid signal contamination from outside the FOV special care has to be taken by choosing the optimum SRF/PSF for each MRSI experiment.
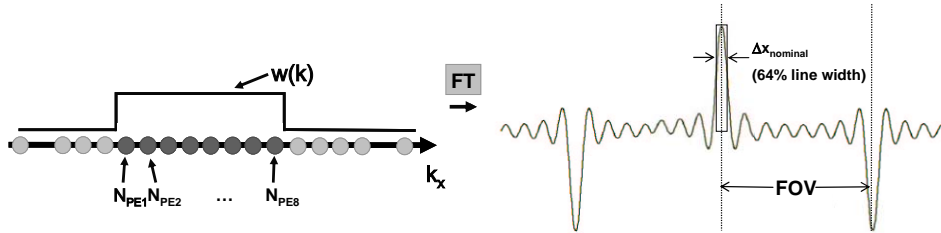
Figure 2.11: One dimensional SRF/PSF with eight phase encoding steps N_{PE}. The FOV of the experiment is given by the period of the SRF/PSF and the nominal resolution by the 64% height of the line width of the main peak.

Reconstruction of this four dimensional MRSI data set consists of a Fourier transformation in the spectral dimension followed by a inverse three dimensional Fourier transformation in the spatial directions, yielding three dimensional images for each spectral point. "Metabolite maps" of each metabolite resonance in the spectrum can be reconstructed from this data in different ways, examples are a simple integration of the spectral points (SUM), the calculating of the maximum intensity projection (MIP) or the sum of squares (SOS) projection (see Figure 2.12) [36].

$$I(x, y, z) = \sum f(x, y, z)$$ $$I(x, y, z) = \max(f(x, y, z))$$ $$I(x, y, z) = \sqrt{\Sigma \, |f(x, y, z)|^2}$$
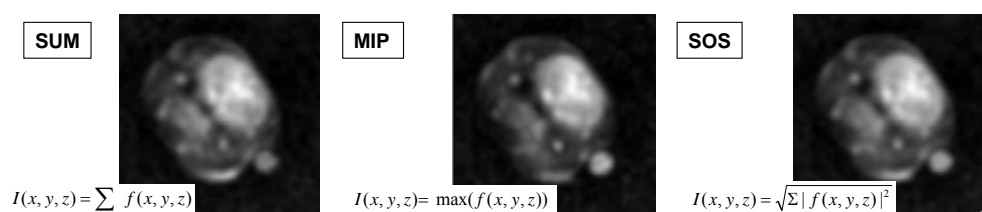
Figure 2.12: Sodium CSI maps reconstructed in three different ways. The SOS reconstruction shows the best image quality.

Before Fourier transformation filtering (see chapter 2.8) and/or zero filling in all directions can be applied to achieve a better image quality.

2.10 **NMR properties of sodium**

Since sodium is the major nucleus of interest in this work and the NMR properties differ from those of protons they are summarized here. The natural abundance of sodium is 100% and its NMR sensitivity is 9.3 % of the proton sensitivity. The relaxation times, T1 and T2, are about two orders of magnitude shorter than those of protons. Sodium is always dissolved as a cation *in vivo*. Its diffusion coefficient in solution at 37°C is 1.9 µm^2/ms [37] which is of the same order of magnitude as the diffusion coefficient of water (3.0 µm^2/ms) at 37 °C. It is a spin 3/2 nucleus exhibiting a quadrupole moment, which does not have a spherically symmetric charge distribution.
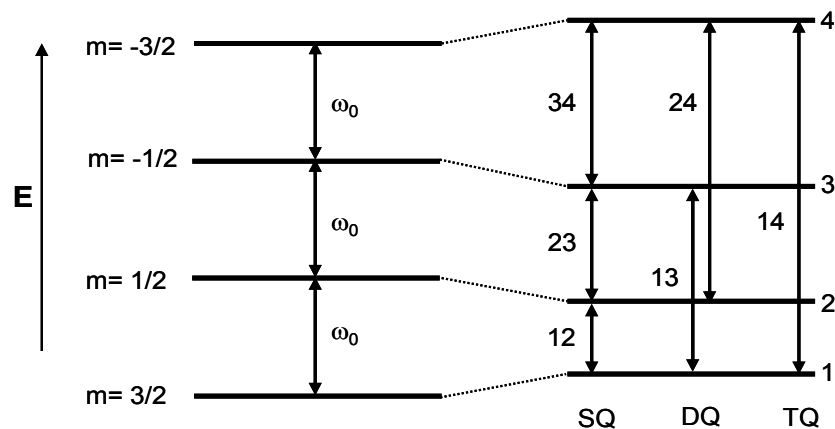
Figure 2.13: Zeeman diagram for sodium (I = 3/2) in a magnetic field. The left shows the distribution with zero and the right with non – zero averaged electric field gradients. Single (SQ), double (DQ) and triple quantum (TQ) NMR transitions are possible as indicated on the right.

A nucleus with a spin ≥ 1 has more than one allowed single quantum (SQ) transition. The energy level (Zeeman) diagram for a spin I = 3/2 is shown in Figure 2.13. It can be seen that four energy levels with m= 3/2, 1/2, -1/2 and -3/2 are formed in the presence of a large magnetic field.

As long as the local electrical field gradients average to zero the allowed states are degenerate and all transitions have the same resonance frequency and the same relaxation times T1 = T2. The relative intensities of the transitions are 30 % for each outer transition and 40% for the inner transition as calculated by time dependent quantum mechanical perturbation theory. Sodium would be in this case 100% NMR visible.

A static electrical field gradient at the nucleus shifts the resonance frequencies of the outer transitions away from that of the inner transition. The resonance frequency of the inner transition is, to first order, insensitive to static field gradients. This effect is dependent on the orientation and the strength of the static electrical field gradient. Since biological tissue is (usually) macroscopically not orientated, random orientations of the static electrical field gradients exist, and the resonance frequencies of the outer transitions will be dispersed over a large spectral range (= heterogeneous broadening).

Time dependent fluctuations of electrical fields at the nucleus generate dynamic quadrupolar effects. Even if the quadrupolar splitting averages to zero over the

fluctuations, relaxation of the resonances can be induced. Miller at al [38] described the relaxation times as a function of the correlation time τ_c and the Larmor frequency ω_0:

T1 relaxation:

$$\frac{1}{T_{1,I}} \propto \tau_c \left[\frac{1}{1+\omega_0^2 \tau_c^2} \right] \tag{2.41}$$

$$\frac{1}{T_{1,II}} \propto \tau_c \left[\frac{1}{1+4\omega_0^2 \tau_c^2} \right] \tag{2.42}$$

T2 relaxation:

$$\frac{1}{T_{2,I}} \propto \tau_c / 2 \left[\frac{1}{1+\omega_0^2 \tau_c^2} + \frac{1}{1+4\omega_0^2 \tau_c^2} \right] \tag{2.43}$$

$$\frac{1}{T_{2,II}} \propto \tau_c / 2 \left[\frac{1}{1+\omega_0^2 \tau_c^2} + 1 \right] \tag{2.44}$$

In the regime where $\tau_c << 1/\omega_0$ the term in the brackets converges and all relaxation times are proportional to $1/\tau_c$. T1 and T2 decay mono exponentially with the same time constant. These conditions are present in solutions, where fast fluctuations occur. Evan in the extra cellular space in biological tissue mono exponential decay exists. The relaxation times are of the order of 20 to 70 ms.

The thermal movement of the intracellular sodium cation relative to the mostly negative loaded macromolecules causes a biexponential relaxation. In this case the intra cellular τ_c of the sodium cations is longer than $1/\omega_0$, but shorter than the time constant of the quadrupolar interaction. As a result the T2 relaxation times of the outer transitions (T2,II) are shorter than those of the inner transition (T2,I) as can be derived from Equations 2.43 – 2.44. Therefore 60% of the total signal has a T2 relaxation time of less than 3ms, resulting in a broad line in the spectrum and is therefore in standard NMR sequences invisible.

Besides the single quantum transitions, double quantum (DQ) and triple quantum (TQ) transitions (see Figure 2.13) are possible.

2.11 **RF Resonators**

Radiofrequency coils for MR differ from conventional antennas. They are designed to maximize the near-field magnetic energy. A high B1 field with a homogeneous distribution within the subject and low resonator losses are the most desirable properties of such a coil. Since most RF coils are used to image either the brain or torso of an animal, the form of the coil is usually cylindrical. Consider an infinitely long cylindrical surface carrying a surface current, J_s, given by:

$$J_s = \hat{z} J_0 \sin \phi \tag{2.45}$$

Then the field inside the cylinder is given by:

$$B(\rho, \phi) = -\hat{\rho} \sum_{m=1}^{\infty} m \rho^{m-1} \left(A_m \cos m\phi + B_m \sin m\phi \right) + \hat{\phi} \sum_{m=1}^{\infty} m \rho^{m-1} \left(A_m \sin m\phi - B_m \cos m\phi \right) \tag{2.46}$$

By applying boundary conditions at the cylinder surface (considering the B field created outside the cylinder), all B_m coefficients are zero and the only non-zero A_m coefficients are given by:

$$A_1 = -\mu_0 \vartheta_0 / 2 \tag{2.47}$$

$$B(\rho, \phi) = \frac{\mu_0 J_0}{2} \left(\hat{\rho} \cos \phi - \hat{\phi} \sin \phi \right) = \hat{x} \frac{\mu_0 J_0}{2} \tag{2.48}$$

This shows that a perfectly uniform B field, directed along x, is produced by a sinusoidal current along the surface of a cylinder of infinite length. An approximate realization of this infinite long cylinder is called the "birdcage" resonator [39]. The "high-pass" configuration [40], with a series of equidistantly spaced "legs", and two "end-rings" is shown schematically in Figure 2.14. For an n-leg high-pass birdcage the highest frequency mode is the so-called end-ring mode, the next n/2-1 modes are each doubly-degenerate with the highest being the one which produces a homogeneous transverse B1 field, and there is one final n-1 mode at the lowest frequency.

Impedance matching the coil to 50 Ohms must be performed in order to ensure maximum power transmission and efficient reception. A balanced impedance-matching network, with variable capacitors to adjust for different loads, should be used to reduce electric field losses in the sample.
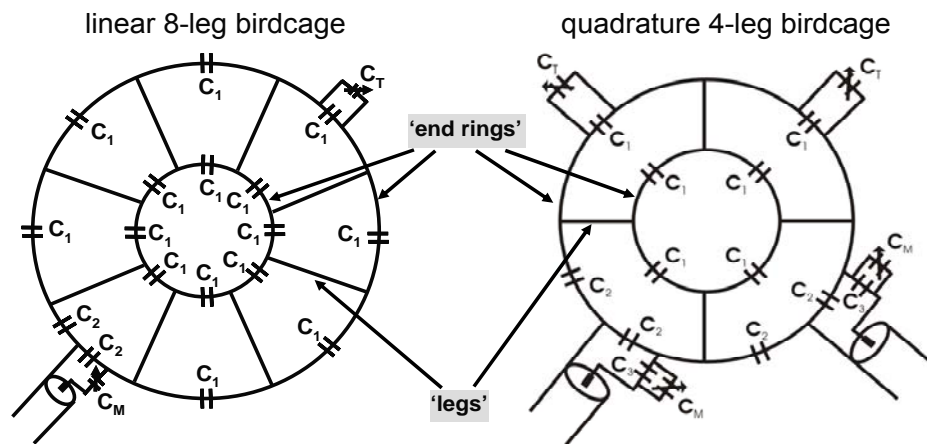
Figure 2.14: Schematic of a linear 8- leg (left) and a quadrature driven 4- leg birdcage resonator (right). The C_M and the C_T are the matching and tuning capacitors to optimize the impedance matching of the resonator for different loads. Because of symmetry reasons C_2 has twice the value of C_1.

Birdcage resonators can be driven in quadrature mode [41](see Figure 2.14). This reduces the power required to achieve for example a 90 degree flip angle by a factor of two, and increases the image SNR by $\sqrt{2}$. Since the homogeneous mode of the birdcage coil is doubly degenerate, exciting one mode with a B1 which is 90 degrees out of phase with the other mode produces a circularly polarized B1 field. If the two modes are not perfectly decoupled additional losses can occur [42]. More details can be found in [43].

In order to determine the quality of a resonator, a variety of methods can be used. To characterize a resonator on the workbench the quality factor Q is often measured. The quality factor Q of a resonator is a measure for the effective resistance R of the resonator:

$$Q = \frac{\omega_{res} * L}{R} = \sqrt{\frac{L}{C}} * \frac{1}{R}$$

(2.49)

The total resistance R of a resonator consists of the resistance of the sample R_s, and the resistance of the resonator R_{res}:

$$R = R_s + R_{res}$$

(2.50)

The quality factors Q_l for a loaded and Q_{ul} for an unloaded resonator are therefore:

$$Q_l = \sqrt{\frac{L}{C}} * \frac{1}{R_s + R_{res}} \qquad\qquad Q_{ul} = \sqrt{\frac{L}{C}} * \frac{1}{R_{res}} \qquad \textbf{(2.51)}$$

The dependence between SNR and Q is given by [44]:

$$SNR \propto \sqrt{Q} \qquad (2.52)$$

For an optimal SNR_{opt} the resonator resistance should be negligible compared to the resistance of the sample ($R_s \gg R_{res}$) and therefore [45]:

$$\frac{SNR_{exp}}{SNR_{opt}} = \sqrt{1 - \frac{Q_l}{Q_{ul}}} \qquad (2.53)$$

If $Q_{ul} \gg Q_l$ the optimum experiment is reached and a higher SNR cannot be achieved by improving the quality of the coil.

The quality factor Q can be measured in several different ways as described in [46] and references therein. In our case Q was always measured through its coupling network: with the probehead properly tuned and matched, one determines the frequency response of the reflected power. Dividing the center frequency by the -7 dB bandwidth yields Q [47]:

$$Q = \frac{f_{res}}{\Delta f} \qquad (2.54)$$

The absolute resonator sensitivity is finally defined as:

$$absolute\ resonator\ sensitivity = \sqrt{\eta * Q} \qquad (2.55)$$

The filling factor η is defined as the ratio of sample volume to total resonator volume.

There are two different basic methods to characterize a RF resonator in the spectrometer:

<u>Spectroscopic method</u>

In this method pulses with increasing pulse length are applied and the length of a 360°- pulse and the signal heights of the 90° and 270° - pulses are determined. The pulse length is directly coupled to the B_1 - field strength (Equation 2.8) and the difference of the signal heights at 270° and 90 ° provide rough information about the homogeneity of the resonator. Furthermore, if the resonator is driven in quadrature mode, it is possible to compare the two channels driven in linear mode and the quadrature driven mode with this method.

Considering a 360° pulse length ($t_{360°}$) the B_1 - field strength can be determined using the following equation:

$$B_1 = \frac{2\pi}{\gamma * t_{360°}}$$

(2.56)

An example of this method is shown in Figure 2.15. The length of the 360°- pulse, the signal heights at 270° and 90 °, and therefore the advantages of a quadrature driven resonator can be easily extracted.

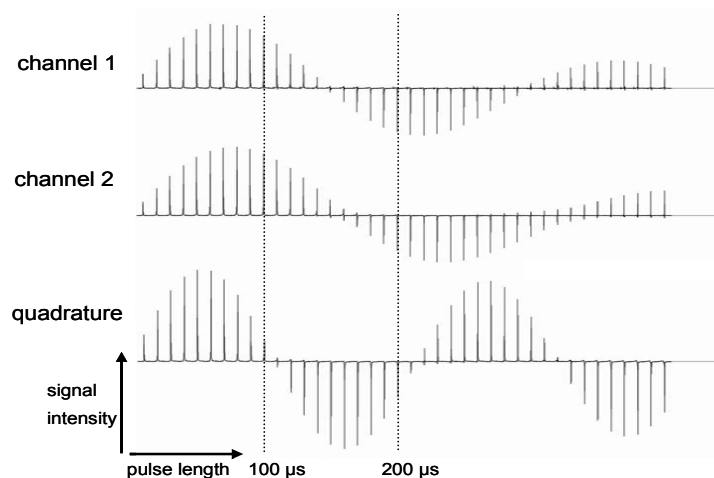**Figure 2.15:** Spectroscopic method to characterize a quadrature birdcage. The 180 degree pulse length for the quadrature mode is by a factor of $\sqrt{2}$ shorter than the linear mode. While the absolute value of the signal height at 90 and 270 degrees is about the same for the quadrature mode, it is apparently reduced in the linear mode. Furthermore is the absolute signal intensity in the quadrature case $\sqrt{2}$ higher.

However, the information achieved with this method does not present detailed information about the local field distribution inside the resonator. It rather shows its overall quality.

<u>Imaging methods</u>

The first more qualitatively method consists of a long preparation pulse given prior to the imaging experiment. The result is an image with black and white signal regions. Adjacent bright signal areas in the images represent a flip angle difference of 180°. In this way the homogeneity could be observed locally.
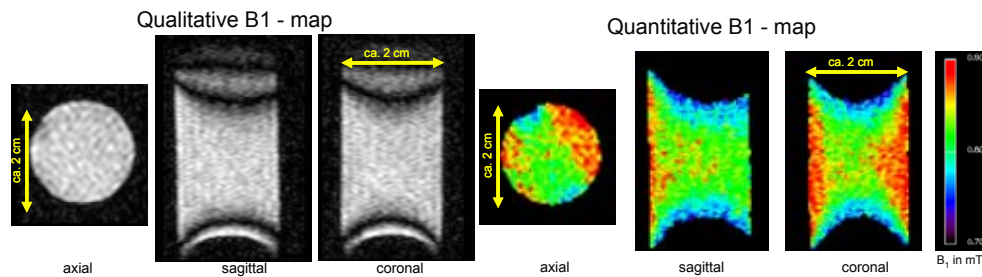
Figure 2.16: Imaging methods to characterize a resonator. In the more qualitative method (left) pulses with a high flip angle are given prior to the imaging sequence resulting in black and bright stripes in the phantom showing the homogenous area of the resonator. The more quantitative method is the 'rotating frame imaging' (right). It allows one to calculate actual B1 values locally.

A more quantitative method is the 'rotating frame imaging' [48]. It allows one to calculate the B_1 – field strength at every location in the resonator. A series of three dimensional imaging experiments with increasing flip angle is performed. Through a Fourier transformation in the pulse angle dimension every point in the image has a frequency (ν_1) which is related to B_1 as:

$$B_1 = \frac{2\pi * \nu_1}{\gamma} \tag{2.57}$$

As long as the Nyquist theorem is fulfilled (1/pulse increments $\geq 2* \nu_{max}$) a quantitative B_1 – map of the whole resonator can be calculated. The images on the right of Figure 2.16 show an example of the B1 distribution of a quadrature driven sodium birdcage resonator.

2.12 **Biological background**

<u>Proton containing metabolites</u>

As mentioned above the compared to water low concentrated in vivo metabolites are the aim proton MRS is heading for. They provide a lot of information on the health status of a subject. Metabolite concentrations are specific signatures for disease. Figure 2.17 was taken from Ross and Bluml [49] and shows an overview of the most important brain metabolites detected by proton MRS, and the associated diseases. An overview of all brain metabolites detected by proton MRS with their chemical shifts and coupling constants can be found in [50]. The three major metabolites that will be discussed in detail in this work are N – Acetyl Aspertate (NAA), Creatine (Cr) and Choline (Cho).

TABLE 5. Differential diagnostic uses of magnetic resonance spectroscopy		
Metabolite (normal cerebral concentration)	Increased	Decreased
Lactate (Lac) (1 mM; not visible)	often Hypoxia, anoxia, near-drowning, ICH, stroke, hypoventilation (inborn errors of TCA, etc), Canavan, Alexander, hydrocephalus	unknown
N-acetylaspartate (NAA) (5, 10, or 15 mM)	rarely Canavan	often Developmental delay, infancy, hypoxia, anoxia, ischemia, ICH, herpes II, encephalitis, near-drowning, hydrocephalus, Alexander, epilepsy, neoplasm, multiple sclerosis, stroke, NPH, diabetes mellitus, closed head trauma
Glutamate (Glu) or glutamine (Gln) (Glu = ? 10 mM; Gln = ? 5 mM)	Chronic hepatic encephalopathy (HE), acute HE, hypoxia, near-drowning, OTC deficiency	unknown Possibly Alzheimer disease
Myo-inositol (mI) (5 mM)	Neonate, Alzheimer disease, diabetes mellitus, recovered hypoxia, hyperosmolar states	Chronic HE, hypoxic encephalopathy, stroke, tumor
Creatine (Cr) + phosphocreatine (PCr) (8 mM)	Trauma, hyperosmolar, increasing with age	Hypoxia, stroke, tumor, infant
Glucose (G) (~1 mM)	Diabetes mellitus, ? parental feeding (G), ? hypoxic encephalopathy	Not detectable
Choline (Cho) (1.5 mM)	Trauma, diabetes, "white" vs. "gray", neonates, post-liver transplant, tumor, chronic hypoxia, hyperosmolar, elderly normal, ? Alzheimer disease	Asymptomatic liver disease, HE, stroke, nonspecific dementias
Acetoacetate; acetone; ethanol; aromatic amino acids; xenobiotics (propanediol; mannitol)	Detectable in specific settings Diabetic coma; ketogenic diet (Seymour et al., 1998) etc.	

ICH, intracerebral hemorrhage; TCA, tricarboxylic acid cycle; NPH, normal pressure hydrocephalus; OTC, ornithine transcarbamylase.

Figure 2.17: Table 5 from Ross and Bluml [49]. Overview of the major brain metabolites and diseases associated with abnormal levels.

NAA is found in the central and peripheral nervous system and is therefore used as a neuronal marker. The concentration of NAA rises during the development of an animal/ human (newborn rat < 1mM – adult >5mM) [51] and the concentration in the brain varies [52] depending on the location. The grey matter has for example a higher concentration of NAA than the white matter [53].

Creatine acts as an energy buffer in the cell in the form of phosphorylated creatine, keeping the level of highly energetic adenosine tri phosphate (ATP) in the myofibrils constant. Furthermore it operates as an energy shuttle in the cell. ATP (produced in the mitochondria) and Cr are turned into adenosine di phosphate (ADP) and phosphocreatine (PCr) in the creatine kinase reaction. The PCr molecule, much smaller than the ATP molecule, diffuses to the myofibrilles and converts ADP into energy rich ATP (Figure 2.18).
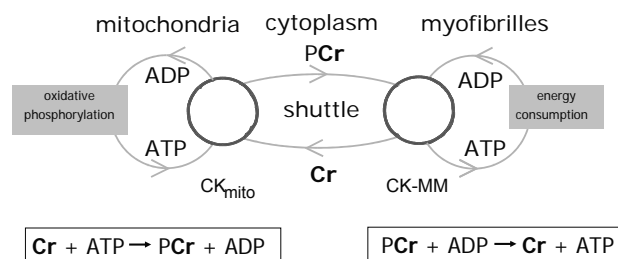
Figure 2.18: The role of Cr as an energy shuttle from the Mitochondria to the myofibrilles. The reaction is called creatine kinase reaction.

As the difference in the resonance frequency of Cr and PCr is much smaller than the linewidth achievable in *in vivo* experiments, often only the total creatine (tCr) signal is discussed. Special care has to be taken in the absolute quantification of the tCr concentration as it is partly NMR invisible due to bonding to macromolecules [54].

Choline and choline-containing compounds are located specifically in membranes. Therefore, during tumor growth the signal for choline increases as shown for example in [55].

Sodium

Heart attack and stroke are two of the most dangerous and wide-spread human diseases in the western hemisphere. Monitoring the sodium homeostasis pro-

vides additional information to characterize the dimension of the injury and the progress of healing [56][57][58]. Another, no less dangerous disease that can be studied by monitoring the sodium distribution is cancer [59][60].

Sodium is the second most abundant element in biological tissue after hydrogen. About 23% of the available energy in form of ATP in humans at rest is utilized by the so called sodium - potassium pump. Na^+, K^+-ATPase is an integral membrane protein which is responsible for translocating sodium and potassium ions across the cell membrane utilizing ATP as the driving force. In one cycle three sodium ions are pumped out and two potassium ions are pumped into the cell [61]. Under normal conditions the intracellular concentration of sodium in human tissue is about 15 mM and the extracellular concentration approximately 145 mM. This chemical and electrical gradient across the cell is necessary to maintain the resting potential of the cell and for the excitable activity of muscle and nerve tissue. In addition it is essential for driving numerous transport processes in the cell. Among other processes, the Na^+, K^+-ATPase regulates fluid reabsorption and electrolyte movement by establishing an ionic gradient across epithelial membranes in the kidneys and the intestines [62].
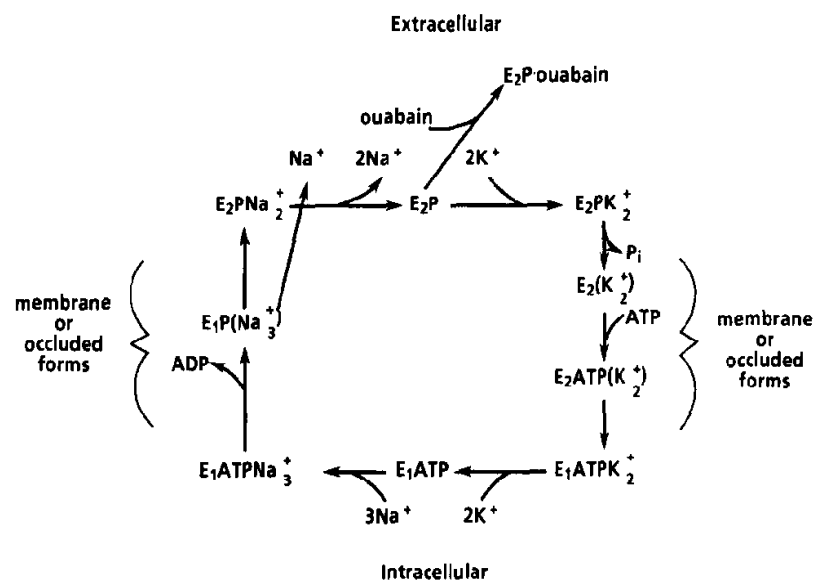

Figure 2.19: Intermediates of NA^+, K^+ - ATPase transport. For each pair of K^+ ions that is transported into the cell, three Na^+ ions are pumped out of the cell into the interstitium. (from [61] adapted from [63])

In those pathologies in which the production of ATP is hampered, the sodium - potassium pump fails and as a result the ion gradient between intra and extra cellular space cannot be obtained. Due to diffusion more and more sodium ions enter the cell. The sodium homeostasis is linked to the calcium homeostasis and therefore a high concentration of calcium builds up in the cells. Increased calcium concentration is suggested to lead to cell death. Hence, measuring the sodium homeostasis may be a useful indicator to monitor the viability of the effected tissue.

A two compartment model of stroke is shown in Figure 2.20 as proposed by Thulborn et al [56]. The table on the left describes healthy tissue whereas the one on the right the situation after an ischemic event. While the total sodium concentration in healthy tissue is around 30 mM, the increase in ischemic tissue can be several hundred percent.

vascular compartment (3%) [Na] = 140 mM		vascular compartment (4%) [Na] = 140 mM		
intra-cellular compartment (85%) [Na] = 10 mM	extra-cellular compartment (12%) [Na] = 140 mM	intra-cellular compartment (intact ??%) [Na] = 10 mM	intra-cellular compartment (damaged ??%) [Na] > 10 mM	extra-cellular compartment (12%) [Na] = 140 mM

Figure 2.20: Two compartment model of stroke taken from [56]. A rise of the sodium concentration in the damaged area up to several hundred percent is possible.

In the case of cancer, the increase in the total sodium signal has two main causes. In the early state of a tumor, cellular proliferation and the acidic extra cellular microenvironment are associated with an increase in intracellular sodium concentration [64]. Hence it is difficult to distinguish between a malignant tumor or, for example, a peritumoral edema [65]. In the later stages of tumor growth, when complete cell destruction takes place, an increase of a factor of 4 in total sodium concentration can occur due to the expansion of the extra cellular space. An increase of up to approximately 1.5 times has been detected in a study of human brain tumors [59].

3 Hardware Setup

3.1 The Avance 750 Spectrometer

Accept parts of the proton spectroscopy, all experiments were performed on an Avance 750 WB spectrometer (BRUKER BIOSPIN, Rheinstetten, Germany). At 17.6 T it is the highest commercially available magnetic field strength for imaging. The bore diameter is 89 mm. The spectrometer is equipped with two gradient systems for imaging. The MINI 0.5 gradient system has an inner diameter of 57 mm and a maximum gradient strength of 200 mT/m. The stronger MICRO 2.5 gradient system has a maximum gradient strength of 1 T/m but only 40 mm inner diameter. The transmitter for ^{1}H experiments has a maximum power output of 300 W and the two transmitters for low frequency nuclei have 300 and 500W, respectively. The system is equipped with four receiver channels.

Figure 3.1: Avance 750. Magnet and preamplifiers of the four channels are shown (bottom right).

3.2 **RF Resonators**

In our setup there is very limited space for the RF-resonator compared to a human-sized scanner. Although surface coils would leave more space for the animal, the use of volume resonators is preferred due to the more homogenous B_1 field throughout the sample. Due to the relatively homogeneous B_1 - field distribution, bird cage resonators were constructed and used for the *in vivo* experiments in this work.

3.2.1 Sodium Resonators for the 200mT/m gradient system

Two birdcage resonators were used for this gradient system. The first bird cage is a commercially available linear eight - leg resonator (BRUKER BIOSPIN, Rheinstetten, Germany) with an outer diameter of 57 mm and an inner diameter of 38 mm, fitting into the 200 mT/m gradient system. To achieve a higher SNR a second bird cage with the same geometry but driven in quadrature mode was constructed. The theoretical gain in SNR of $\sqrt{2}$ was fully achieved. The characteristics of these resonators can be found in [66]. The probe base for the BRUKER resonator was a commercially available probe base from BRUKER and the one for the quadrature bird cage was a home built copy.

3.2.2 Sodium Resonator for the 1T/m gradient system

Since sodium has very short relaxation times (T1 and T2), short echo times (TE) in the imaging sequence are essential for good SNR. Furthermore short repetition times (TR) are achievable, again to increase the SNR per scan time. With a maximum gradient strength of 200mT/m the minimal TE and TR are relatively long due to the slew rate of the gradients. This and the fact that the coil sensitivity increases with smaller size of the resonator and the higher filling factor of a smaller coil gave rise to the decision to build a resonator for the 1 T/m gradient system.

However the design demands for this bird cage and the corresponding probe base were manifold, especially as the space inside the resonator had to be big enough to hold mice up to ~ 30 g. Furthermore the clear bore of the probe base

had to have a certain diameter for the tubes for the anesthetic gas, the ECG and breath trigger, and lines for optional drug applications.

3.2.2.1 Construction

Because of the above mentioned demands and the limited space the design of the resonator for the 1T/m gradient system was a four leg bird cage driven in quadrature mode. The conducting elements of the resonator (height: 4cm) were etched on a 60 µm thick copper – polyamide composite (DuPont Pyralux, Willmington, USA) which is placed onto a GFK-tube with an outer diameter of 28 mm and an inner diameter of 27 mm, which defines the total useable space inside the resonator. Standard chip capacitors (CHB-series, Tekelec Temex, Sophia-Antipolis, France) with a value of C_1= 43 pF were used in the ring of the resonator. The variable capacitors for matching and tuning (Voltronics Corp., Denville, NJ, USA) had a range from 1 to 30 pF. In the case of the matching capacitors additional capacity (C_3 = 12 pF) had to be added to enlarge the matching range of the resonator. The tunable capacitors were placed on a ring (machined out of circuit board, inner diameter: 28 mm, outer diameter: 37 mm) directly below the etched coil. To obtain a more homogenous B_1 field the matching capacitors are coupled between two capacitors (C_2 = 91 pF) with about twice the value of the ring capacitors. A scheme of the resonator can be seen on the right side of Figure 2.14.

The high frequency shield of the resonator consists of an eight µm thick copper foil on a GFK-tube (inner diameter: 38 mm, outer diameter: 39.5 mm, length: 125 mm). Because of the limited space the shield in this design was very close to the capacitors of the resonator and therefore had a large effect on the resonance frequency: without the shield the resonance frequency was shifted by ~38 MHz down field.

The probe base also had to be redesigned and machined. The outside is a GFK-tube (outer diameter: 39 mm, inner diameter: 37 mm) which is 66 cm long. The bottom of the base which contains the BNC connectors to the transmit/receive chain of the spectrometer was machined out of aluminum. The inside of the probe base is constructed from four additional circuit board rings, two semi rigid cables (for signal transmission), and two copper tubes for stabili-

zation. The top of the base is a PVC-socket which is connected on one side to the semi-rigid cable and the copper tubes and on the other side to the resonator. Two rods for matching and two for tuning protruded through the circuit board rings and the PVC-socket to the resonator. The whole setup can be seen in Figure 3.2.
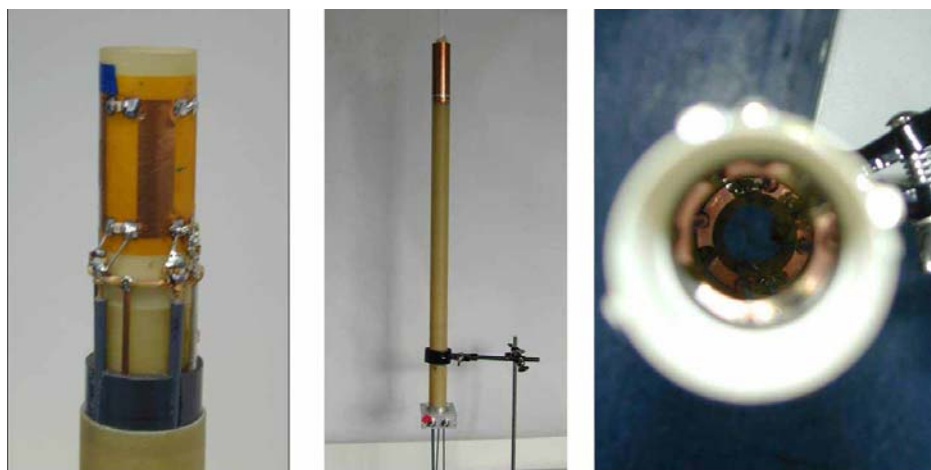
Figure 3.2: Sodium four rung birdcage driven in qudrature mode. Rf – coil with matching and tuning network (left). Picture of the whole resonator (middle) and view through the resonator (right).

3.2.2.2 Characterization on the work bench

For all measurements on the work bench and in the spectrometer a standard solution of 200 mM NaCl in a 20 mm Ø NMR tube was used. Characterization on the work bench was done using a HP network analyzer (HP 8712 ET, Agilent, Palo Alto, CA, USA). The quality factors Q of the linear modes were measured in reflection-mode with a span of 50 MHz. The results are shown in Table 3.1:

	Q – unloaded	Q - loaded	Q-unloaded /Q-loaded
channel 1	157	132	1.19
channel 2	150	132	1.14

Table 3.1: Measured Q values of the four leg quadrature sodium birdcage for the MICRO 2.5 gradient system.

The ratio between Q_u and Q_l was approximately 1.2. This means that the contribution of the sample noise was low compared to the noise in the resonator itself. The reason for this small drop in Q is most likely the short distance between the shield and the resonator itself (~5 mm between resonator legs and shield). Due to the limited space inside the gradient system (40 mm Ø) and the necessary volume for the sample (27 mm Ø) it was not possible to increase this distance. The transmission from channel 1 to channel 2 was measured to be -24 dB. This means that they are extremely well-decoupled and the full quadrature gain should be achieved.

3.2.2.3 Characterization in the Magnet

<u>Spectroscopic method</u>

The two channels were investigated separately and in quadrature mode in this method. The variable pulse had an initial length of 10 µs and an attenuation of 6 dB. The following pulses had increasing pulse length of 10 µs. The achieved spectra are plotted in Figure 2.15 and a summary of the results is shown in Table 3.2. The theoretically expected gain of the quadrature mode (factor of $\sqrt{2}$ in signal intensity and B_1 – field strength) was fully achieved. Furthermore, the ratio of the signal intensity of the 90° and the 270° pulse of 95% shows the very high homogeneity of the B_1 field distribution.

	360° pulse length [µs]	B_1 [µT]	B_1 gain	signal int. 270°/90°	signal int. gain
channel 1	295	500	1.08	0.71	1.06
channel 2	320	461	1.0	0,67	1.0
quadrature	214	690	1.50	0.95	1.42

Table 3.2: Spectroscopic characterization of the quadrature driven sodium bird cage for the 1 T/m gradient system.

<u>Imaging methods</u>

To characterize the B1 field distribution qualitative and quantitative B1 maps were acquired as described in chapter 2.11. Since relaxation times of sodium

are very short, an excitation pulse with a high flip angle was given before each phase encoding step instead of only one long preparation pulse prior to the whole imaging experiment to acquire qualitative B_1 maps. Taking this into account a longer repetition time (3*T1) had to be chosen to avoid saturation effects. An image with an excitation pulse of 450° is shown on the left hand side of Figure 2.16. With this qualitative method the excellent homogeneity in the middle of the resonator can be clearly seen.

To calculate a quantitative B1 map three dimensional images with varying pulse attenuations (30 dB – 0 dB) were acquired as described in chapter 2.11. The pulse length of the hard pulse was 250 μs. The right hand side of Figure 2.16 shows the calculated B_1 – map for the quadrature mode of the bird cage. The homogeneous region in the middle of the resonator is larger than 20 mm. Hence, the variation of the B_1 field strength in the whole sample is less than 10 %. The absolute value of B_1 agrees well with the spectroscopic finding.

3.2.3 Proton Resonators for the 200 mT/m gradient system

The resonators used for proton *in vivo* experiments were an 8 leg linear driven (38 mm inner diameter) commercially available (BRUKER) birdcage resonator and a home built, more homogeneous rebuild of the first. The characterization of both can be found in [67].

3.3 **Animal Handling System**

For each resonator with a different inner diameter a different animal handling system had to be constructed.

The rodent lays on the animal handling system as shown in Figure 3.3. The teeth were placed onto a toothpick and an additional fixation with surgical tape was necessary (not shown) as the animal was vertical in the magnet. Special care had to be taken not to hinder the animal from free breathing. Next to the rodent two tubes, one for the isoflurane/oxygen mixture for the anesthesia and the second for ventilation (not shown, as only necessary for bigger animals) were mounted. The respiratory sensor, used for triggering, consisted of an air pad. It is connected to the blue tube. The electrodes for ECG triggering are also

not shown on the picture, but in the heart studies the ECG leads were connected to the front paws with standard electrodes.

In the case of rats, only the head could be investigated as the animal was too big to fit into the volume resonator.
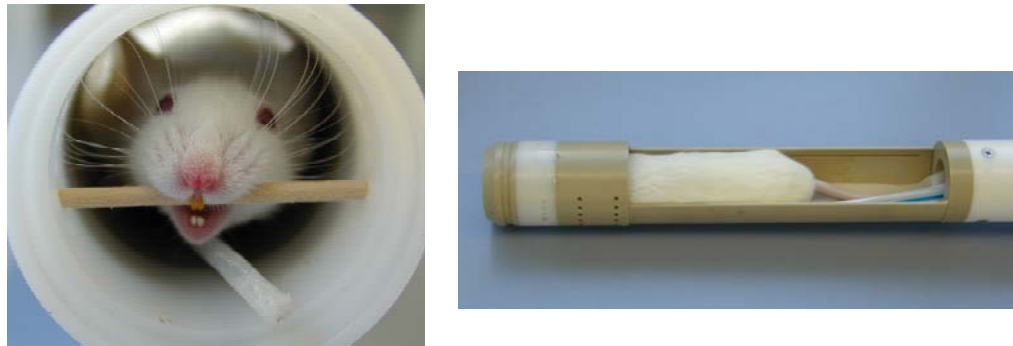
Figure 3.3: Animal handling system for the Bruker 38 mm birdcages and the Mini 0.5 gradient system.

For respiratory and ECG triggering a specially designed triggering unit (RAPID Biomedical, Wuerzburg, Germany) was used. Figure 3.4 shows parts of the actual system with the monitored signal on the screen. Due to the high sensitivity of the breath trigger, a signal from the heart beat could be observed and was used alternatively for heart beat triggering. If no triggering was necessary (brain, kidney studies) the system served to monitor the vitality of the animal.
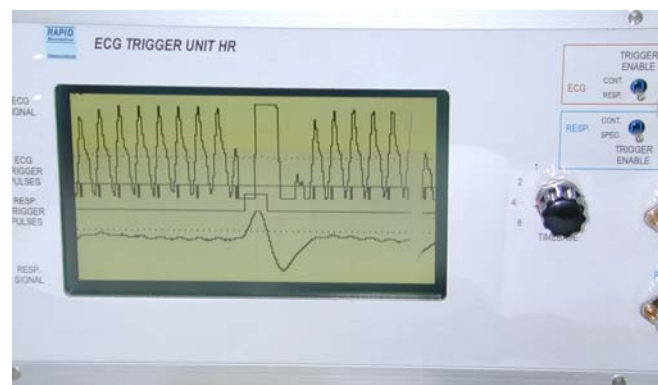
Figure 3.4: Breath and ECG triggering unit (RAPID Biomedical, Wuerzburg, Germany)

4 ^{23}**Na Imaging of Rodents**

4.1 **Methods**

For *in vivo* sodium imaging there are significant constraints in terms of the total data acquisition time, dictated by the duration of anesthesia, and the available SNR. Since sodium is a quadrupolar nucleus, the T_2 value of parts of the signal in tissue is extremely short, ~2-3 ms, and so specialized pulse sequences must be employed. Various techniques such as single point imaging and variants thereof [68][69] and twisted projections [70][71] have been used, as well as standard chemical shift imaging (CSI) [72]. The major disadvantage of the CSI method is the inherently long data acquisition times for four-dimensional (three spatial and one spectral) datasets. This means that only a relatively sparse three-dimensional k-space matrix can be sampled, and the resulting point spread function (PSF) has significant side-lobes. A number of techniques have been developed to improve the PSF, including acquisition weighting via a variable number of signal averages [73][74] or variable tip-angle and relaxation delays [75][76]. A promising recent approach, termed density-weighted phase encoding, uses a variable density k-space coverage [77]. In addition to an improved PSF compared to conventional CSI, the variable-density approach also has a significant advantage in requiring a smaller number of k-space samples to achieve a given spatial resolution over a given field-of-view than is the case for uniform k-space coverage.

Pure phase-encoding (PE) in all spatially resolved dimensions is still the gold standard in sensitivity-limited metabolic *in vivo* MR experiments [78]. Due to the short relaxation times and the low concentrations chemical shift imaging is one of the most appropriate methods for sodium imaging. In this work density weighted CSI (DWCSI), a purely phase encoded three dimensional method with a non-uniform k-space sampling scheme is used. It was first proposed by Greiser et al [77]. A brief overview, the data processing, and the newly developed extensions to measure T1 and T2 are shown in this chapter.

4.1.1 DWCSI

The biggest problem in standard or uniformly weighted CSI (UWCSI) is the low achievable spatial resolution, and as a consequence thereof, the severe signal contamination from neighboring regions due to the side lobes of the spatial response function (SRF). This contamination can be reduced if acquisition weighting, i.e. acquisition of k-space positions with different accumulation numbers (accumulation weighted CSI, short AWCSI), can be applied. The effect of the acquisition weighting is an increase in experimental time or a reduced FOV, if the spatial resolution is the same as in a UWCSI experiment. Weighting k-space with a Hanning window has been shown to be a good compromise between sensitivity and spatial resolution [79] in AWCSI.

$$w(k) = \frac{\Delta x \cdot \beta}{2} * NA * \left(1 + \cos\left(2\pi \frac{k \cdot \Delta x}{\alpha}\right)\right)$$

(4.1)

Equation 4.1 shows the Hanning function for a given resolution Δx and a given total number of acquisitions NA. The width α of the Hanning function is defined as the 64% width of the calculated SRF (c.f. Raleigh criterion in optics) and β has to be adjusted so that the integral over the function equals NA. In the three dimensional case the value for α = 1.78 and for β = 1.73 [6].

In the case of DWCSI the Hanning function is used to weight the k-space in a different way than in the AWCSI experiment. The distance between neighboring points in k-space is no longer uniform. The density of the points in k-space from k=0 to k=k_{max} decreases according to the Hanning window. To illustrate the different types of sampling, Figure 4.1 was taken from [77].
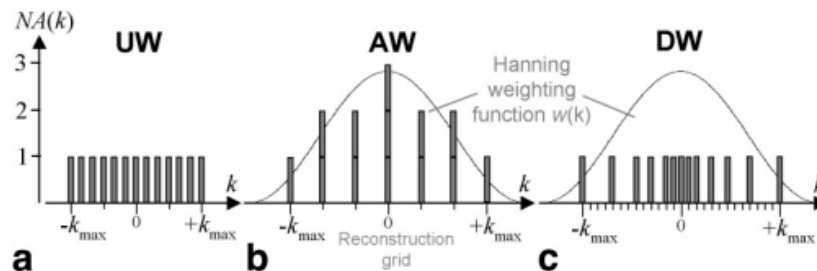
Figure 4.1: Uniformly weighted (UW), accumulation weighted (AW), and density-weighted (DW) 1D phase-encoded experiment. In AW, the weighting is accomplished by accumulation of distinct PE steps. In DW, a variation of the sampling density is employed to approximate the weighting function w(k). In UW, the achievable FOV = 1/Δk is larger than in AW as no accumulations of single PE-steps are required. In DW, the central k-space is sampled more densely than in AW at identical NA.

For the algorithm to calculate the k-space positions for the DWSCSI acquisition scheme, readers are referred to [77]. In Figure 4.2 the SRF of a 2D sampling scheme with the same NA (NA=1024) and the identical resolution Δx from all three acquisition schemes are shown. The SRF of the AWCSI shows clear reduction of the FOV compared to the SRF of the UWCSI. The DWCSI reduces the contamination from the side lobes of neighboring voxels compared to the UWCSI and does not reduce the FOV as much as the AWCSI, although the term FOV has to be defined differently in the DWCSI (see [77]).
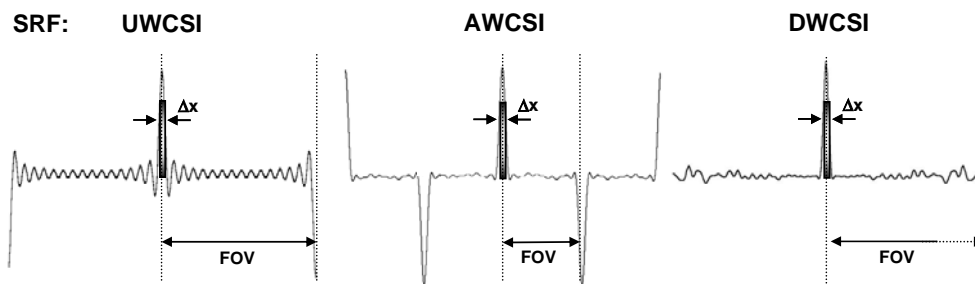
Figure 4.2: SRF from a UW-, AW-, DWCSI 2D phase-encoded scheme with the same NA and Δx. In UW, the achievable FOV is larger than in AW. The side lobes in AW- and DWCSI are suppressed. In DW the FOV is not clearly defined, but is larger than in AW.

The dependence of the SRF on NA and therefore on the FOV, is shown in Figure 4.3. A 2D sampling scheme (matrix size: 256 x 256) was filled with NA = 128, 256, 512, 1024 and 2048 different k-space points according to the DWCSI algorithm. The growth of the FOV and the radial noise distribution without a periodic appearance of a large aliased signal found in the other acquisition schemes can be observed.
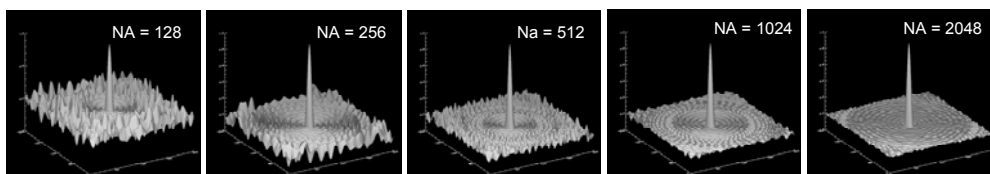
Figure 4.3: Simulation of the SRF of a DWCSI 2D phase-encoded scheme with different NA and constant Δx. The growing area of low noise distribution (FOV) can be seen from the left (NA=128) to the right (NA = 2048).

Hence, DWCSI is superior to other CSI acquisition schemes as the number of acquisitions can be reduced compared to UWCSI without the aliasing problems in AWCSI. In our work 3D DWCSI with either 8192 or 32768 phase encoding steps on a 128^3 matrix was used.

4.1.2 Data reconstruction of DWCSI

The size of a DWCSI data set was 128^3 points for the spatial dimensions and 512 complex points in the spectral dimension without zero filling. Therefore the hardware and software had to fulfill special requirements to reconstruct the large size of the DWCSI data sets. A Pentium 4 computer with a working memory of 3 GB running on a SUSE Linux platform and the software IDL (Interactive Data Language, RSI, Boulder, CO, USA), which could address 2GB to one variable were required to handle the reconstruction. After acquiring the 8/32k FIDs of the DWCSI pattern, zero filling by a factor of two and an exponential filter with up to 20 Hz line broadening were applied to the data in the spectral dimension. After sorting the fids to the DWCSI grid zero filling in the three spatial dimensions by a factor of two followed by a segmented FFT was performed. To reduce the enormous size of the data set, only the part of the data containing the actual object was stored. After that, sum of square (SOS) reconstructions around the sodium peak in the spectral dimension were calculated.

4.1.3 Measuring T1 with DWCSI

An extension to measure T1 with the DWCSI method is shown in Figure 4.4. Before the actual DWCSI module an inversion pulse and a spoiler gradient were applied. By using increasing delays (vd) between the inversion and the DWCSI

module for each dataset the T1 curve can be acquired. For an optimum T1 fit of the data it is important to acquire the first point shortly after the inversion and to have the last point acquired as late as possible. All pulses are block pulses to keep the time between excitation and acquisition as short as possible. The additional waiting time at the end of the acquisition is necessary due to the fact that the magnetization has to be fully recovered before the next scan. Hence, the experimental time is relatively long. A saturation recovery T1 DWCSI experiment, which could cut down the experimental time tremendously, was also introduced, and was used in the time critical measurement of T1 in a stroke model of the mouse brain.
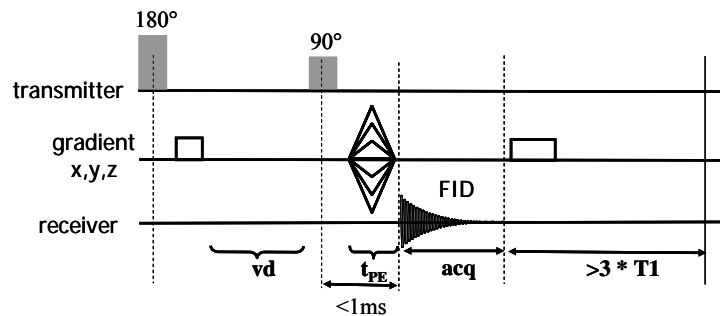
Figure 4.4: T1 DWCSI method. It consists of a DWCSI and an inversion recovery module. t_{PE} is the phase encoding time, acq the acquisition time (usually ~ 64 ms), and vd the variable delay to scan the T1 curve. The additional delay (>3*T1) is for the relaxation of the magnetization.

4.1.4 Measuring T2 with DWCSI

In order to measure T2 the DWCSI was converted into a spin echo DWCSI sequence with different echo times. The pulse program is shown in Figure 4.5. .All pulses are again hard pulses. The crusher gradient was kept as short as possible to allow for very short echo times (~ 1 ms).
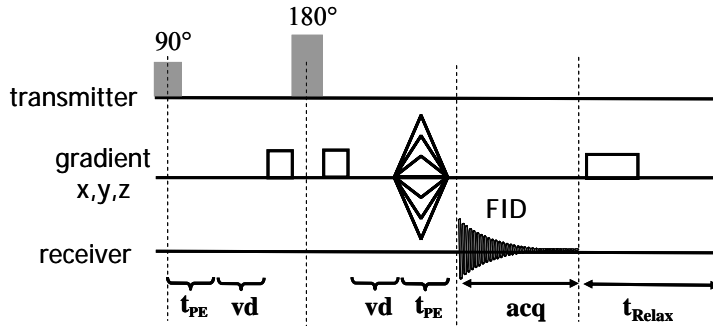
Figure 4.5: T1 DWCSI method. It consists of a DWCSI and an inversion recovery module.

4.2 Phantom Experiments

In this section, evaluation of the point spread function of the DWCSI sequence with respect to the image quality and the validation of the T1 and T2 DWCSI methods are shown on phantom experiments. All phantom experiments are performed with a solution of 200 mM NaCl in a 20 mm Ø NMR tube at 20 °C.

4.2.1 The effect of k-space undersampling on the point spread function

As already seen in Figure 4.3 the FOV and also the SRF of the DWCSI is dependent on the total number of FIDs acquired. The more FIDs acquired the smoother the SRF. In this work two different sampling schemes with either 8192 or 32768 phase encoding steps were used. Figure 4.6 shows on the right side axial and sagittal SOS images of the data set acquired with 8192 PE steps and on the left side the corresponding images from a 32768 PE steps data set reconstructed as described in 4.1.2. Below the images are profiles along the middle of the images (yellow line). The standard deviation along a 1.5 cm long profile in the middle of the phantom is 5% of the average signal intensity for the 32k PE steps data set and 7% for the 8k case.
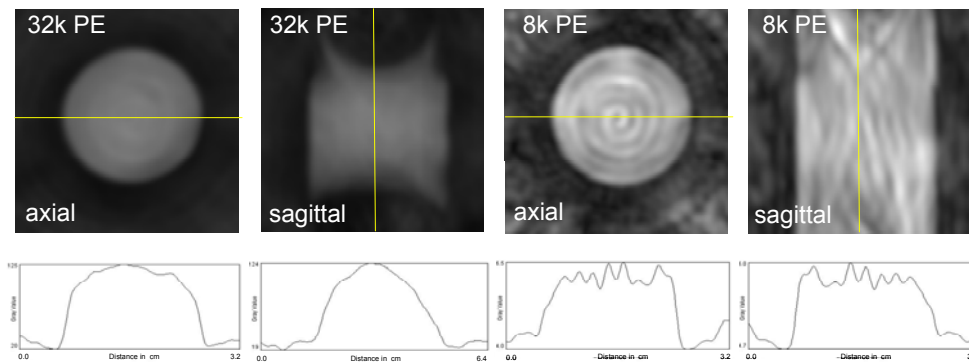
Figure 4.6: Phantom DWCSI experiments. The left side shows images from the 32k PE steps data set and the right side from the according 8k PE data set. Below the images are profiles along the middle of the images (yellow line). (Acquisition parameters: SWH = 4000, TD = 512, TR = 73 ms, T_{exp} (8k PE) = 10 min, res = 1 x 1 x 1 mm^3. Reconstruction parameters: 8k PE: zerofilling by a factor of 2 in all 4 dimensions / 32k PE: same as 8k except, no zerofilling in z direction).

Although the 32k PE steps experiment has a smoother profile (or SRF) and of course a higher SNR it takes 4 times longer than the 8k data set and is therefore not appropriate for all studies. For *in vivo* experiments the total experimental time has to be taken into consideration: Either the animal can stand only a certain time in the magnet (especially after an operation) or time course studies need a certain temporal resolution and therefore the 8k PE steps data set had to be used.

4.2.2 T1 measurements

For theT1 DWCSI, described in 4.1.3, the sampling scheme with 8192 PE steps was chosen as this will be the scheme for experiments in animals due to the limited time *in vivo*. The resolution was chosen to be 1 x 1 x 1 mm^3.12 data sets with different variable delays (vd) were acquired. The total experimental time of the five dimensional data set was approximately 6.5 h. The single DWCSI data sets were reconstructed as described in 4.2.1 (zero filling in four dimensions by a factor of 2), except that in the spectral dimension an integration over the main peak instead of a SOS reconstruction was performed. The resulting four dimensional dataset was fitted to the T1 curve using a home written IDL routine. The fitting parameters in this three parameter fit were M0, a, and T1:

$$M(t) = M_0 * (1 - a * \exp(-t/T_1)) \tag{4.2}$$

The middle slices of the three dimensional data sets with the longest vd = 500ms, the M0 map and the T1 map can be seen in Figure 4.7. The given T1 = 55.5 ± 3.2 ms is an average T1 over the middle 20 slices of the three dimensional T1 map. The right side of Figure 4.7 shows an example T1 fit of the data. While the expected pattern of the 8192 PE DWCSI can be seen in the two left images it almost disappears in the T1 map. The additional appearing artifact shows considerable ripples, but is still less than in conventional CSI. To validate the T1 DWCSI sequence a global inversion recovery and a global saturation recovery method were used to measure T1 of the same phantom. The inversion recovery sequence yielded a T1 of 53.8 ± 2.3 ms and the saturation recovery a T1 of 55.0 ± 3.1 ms.

This result shows that the T1 DWCSI method can be used to acquire three dimensional T1 maps with a good resolution. The artifacts are only in a range of ± 6%, which is negligible or at least in the same range as the error coming from the low concentrations in *in vivo* sodium CSI.

Figure 4.7: Results from the T1 DWCSI measurement. The left image is the middle slice of the data set with vd = 500 ms. The middle images are the M_0 and the T1 fit of the middle slice of the three dimensional fitted data set. And the right image is an exemplary T1 curve. (resolution = 1x1x1 mm^3,vd=(0,1,4,8,12,20,40,60,80,120,200,500) ms, SWH = 4000 Hz, TD =512, t_{Relax} = 85 ms , TR= 151 ms)

4.2.3 T2 measurements

To evaluate the T2 DWCSI method, again, the 8192 PE scheme was used. The resolution was 1 x 1 x 1 mm^3. Image reconstruction was performed as described in 4.2.2, and a T2 three parameter fit was applied (again IDL):

$$M(t) = M_0 * \exp(-t/T_2)) + C \qquad (4.3)$$

The three parameter fit was chosen as the signal in the spectroscopic dimension is integrated over the magnitude of the main peak and therefore, at long echo times, the integral over noise will always have a value larger than zero. The image on the left side of Figure 4.8 shows the middle slice from the spin echo data set with an echo time of 1.3 ms. The middle images are again the M0 map and the T2 map of the middle slices of the fitted data sets. The pattern of the 8192 PE DWCSI can not be seen in the T2 map. The average T2 was 55.4 ± 2.8 ms. Again, an example T2 fit is shown on the right side of Figure 4.8.

To validate the T2 DWCSI sequence two global methods were used. The first method, a global T2 spin echo method with CPMG preparation [80], [81] yielded 53.1 ± 1.9 ms and the second method a spin echo sequence with variable echo time resulted in a T2 of 53.9 ± 2.2 ms. This results were in good accordance with the T2 DWCSI method. Hence, the T2 DWCSI method can be used to measure T2 of sodium.
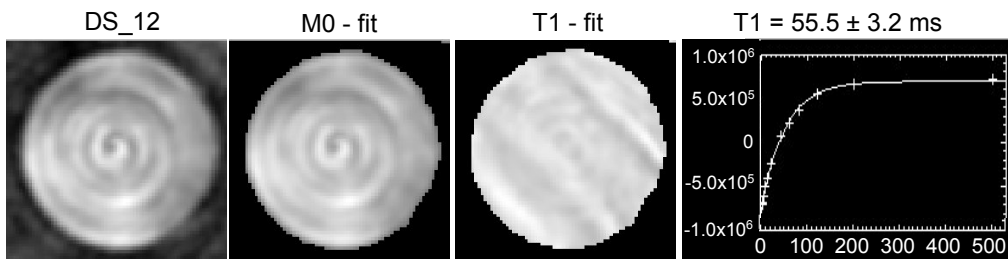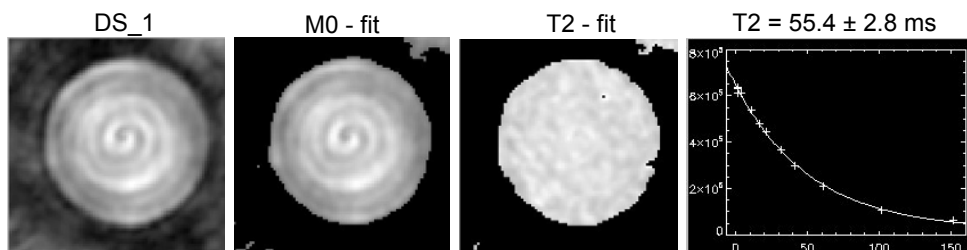

Figure 4.8: Results from the T2 DWCSI measurement. The left image is the middle slice of the data set with TE = 1.3 ms . The middle images are the M$_0$ and the T2 fit of the middle slice of the three dimensional fitted data set. And the right image is an exemplary T2 curve. (resolution = 1x1x1 mm^3, TE = (1.3, 1.4, 1.8, 3.8, 11.3, 16.3, 21.3, 31.3, 41.3, 61.3, 101.3, 151.3) ms, SWH = 3500 Hz, TD =512, t$_{Relax}$ = 85 ms , TR= 151 ms)

4.2.4 Temperature dependence of T1 and T2

In an additional experiment the temperature dependence of the T1 and T2 times was investigated. The sample was preheated in a water bath to a specific temperature (up to 80 °C) and than inserted into the magnet and global T1 and T2 times were measured at least five times. Each experiment took about 1.5 min. The time taken from the point where the sample was taken out of the water bath until the end of the measurements was determined. After the scans the sample was brought to the same temperature as before and inserted into the resonator but not in the magnet. This time the cooling phase of the sample was monitored with a thermometer. In this way rough information about the T1 and T2 times in a temperature range of about 50 °C was acquired.
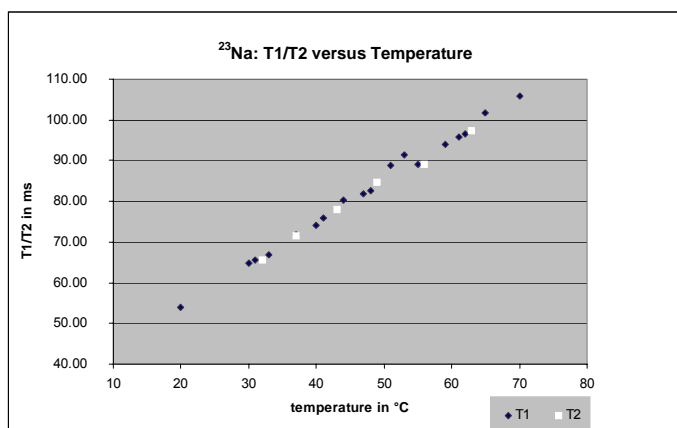
Figure 4.9: Temperature dependency of the longitudinal and transverse relaxation times of sodium. A linear behavior in the temperature range from 20 to 70 °C can be observed. Black diamonds are T1 and white squares are T2 measurements.

The T1 values are the black diamonds and the T2 measurements are the white squares in Figure 4.9. A linear increase in both T1 and T2 in this temperature range can be observed, as predicted.

4.3 Sodium DWCSI of Rat and Mouse Brain

In the early 1990`s the major limitation of sodium MRI was the suboptimal NMR systems resulting in a low SNR and therefore images with an unacceptable spatial resolution in very long scan times (>30 min) [65], [82], [83]. Due to the advances in system technology and sequence development [70], [84] sodium imaging of the brain has become feasible in the last 15 years.

Animal studies have been performed to calculate the total tissue sodium concentration in rats [84], [85], while other animal studies have focused on the pathologies discussed in chapter 2.12 (stroke: [56], [57], [58], [86]; tumor: [59], [60]). Many studies on the human brain were conducted focusing on anatomy [87], [88], [89], [90]. Some of them included measuring T2 and/or T2*. Recently the move to higher fields has reduced the scan time and/or improved the resolution. The latest result at 7 Tesla, shown by Liu et al [87], yielded a resolution of (4 x 4 x 8) mm^3 in ~5 min scan time. Only one recent study of stroke in the human brain (including the acute stroke) was described by Thulborn et al [56]. The sodium concentration in tumors of the human brain with a voxel size of 0.2 mL has been presented by Ouwerkerk et al [59].

In this study the focus was on the spatial resolution of sodium MRI using DWCSI. Anatomical images of the healthy and infarcted rat brain and the first sodium MRI images of the mouse brain (healthy and infarcted) have been acquired.

4.3.1   Sodium MRI of the healthy Rat Brain

Material and Methods

Due to the limited space in the magnet adult Fischer rats (Charles River, Sulzfeld, Germany) with weights up to max. 220 g were used to image the brain. After being anesthetized (mixture of carbogen and isoflurane (4 - 5%)) in a special constructed box the carbogen flow was set to 1 l / min, the isoflurane dose was reduced to ~1.5 %, and the rat was placed onto the animal handling system, fixed and inserted into the resonator and the magnet. Life functions were monitored with the breath / ECG trigger unit (see chapter 3.3.). The MINI 0.5 gradient system with a larger inner diameter had to be used. Proton images were acquired with the birdcage resonator described in chapter 3.2.3. After the proton imaging the probe base with the rat was taken out of the magnet, the resonator was unscrewed from the base, and replaced with the commercial sodium birdcage described in chapter 3.2.1. In this way the rat was placed back to the same position in the magnet and sodium images were recorded.

Proton MRI

Figure 4.10 shows four axial slices from the rat brain acquired with a 2D RARE sequence. In the left image the olfactory bulb (ob) can be seen. The next image shows the cortex (co, grey matter) and the beginning of the corpus callosum (cc, white matter). Below the corpus callosum (following image) brain cavities filled with cerebro spinal fluid (csf) and the striatum (str) are clearly distinguishable. The carotid arteries, the main arteries supplying the brain with blood are also shown in this image. The right image shows besides the co, cc and csf the hippocampus (hip) further back in the brain.
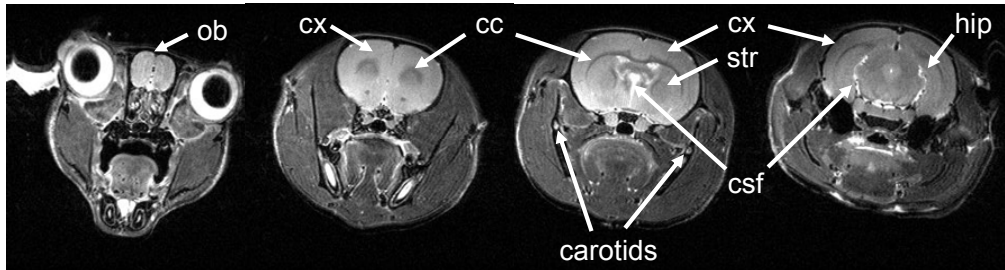
Figure 4.10: Four axial slices through the rat brain from a 2D ^{1}H RARE data set. The olfactory bulb (ob); corpus callosum (cc); cortex (cx); hippocampus (hip), striatum (str) and the carotid arteries are marked with arrows. (Parameters of the RARE sequence: SWH = 100 kHz, $TE_{first\ echo}$ = 5.3 ms, RARE factor = 16, NAE = 8, T_{tot} = 32 min, Res = (117 x 117 x 500) μm^3, N_{Slices} = 32).

Sodium MRI

DWCSI data sets with 8k PE steps and different resolutions were acquired from different rats. The acquisition delay (time between excitation and acquisition) was minimized to ~ 0.5 ms. With a TR of 150 ms and a NS = 1 the total scan time was 20.5 min (SWH = 4500 Hz, TD = 128). Figure 4.11 shows an axial SOS image from each of the 8k PE steps data set with voxel sizes of 43, 18, 9 and 6 μL. The SNR was calculated by averaging the whole brain and dividing it by the standard deviation of the noise outside the brain.
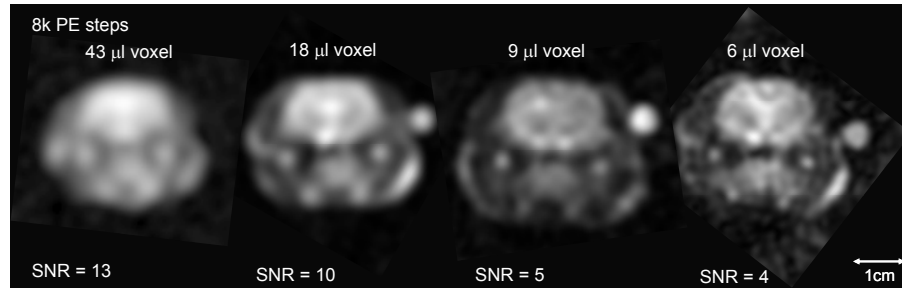
Figure 4.11: Axial sodium images from 3D DWCSI data sets of rat brains with different resolutions. The resolution is increased from the left to the right. Each scan had 8192 phase encoding steps. To achieve higher resolutions the pre acquisition delay had to be increased (from 530 to 870 μs) due to the limited gradient strength (G_{max}=200 mT/m).

Due to the maximum gradient strength limitation the acquisition delay for the data sets with 32k PE steps had to be extended to 920 μs to achieve a resolution of 5μL (1.4 x 1.4 x 2.7 mm^3) voxel size. The whole head of a rat is shown in Figure 4.12. Again the major brain structures with a higher SNR than in Figure 4.11 can be seen.
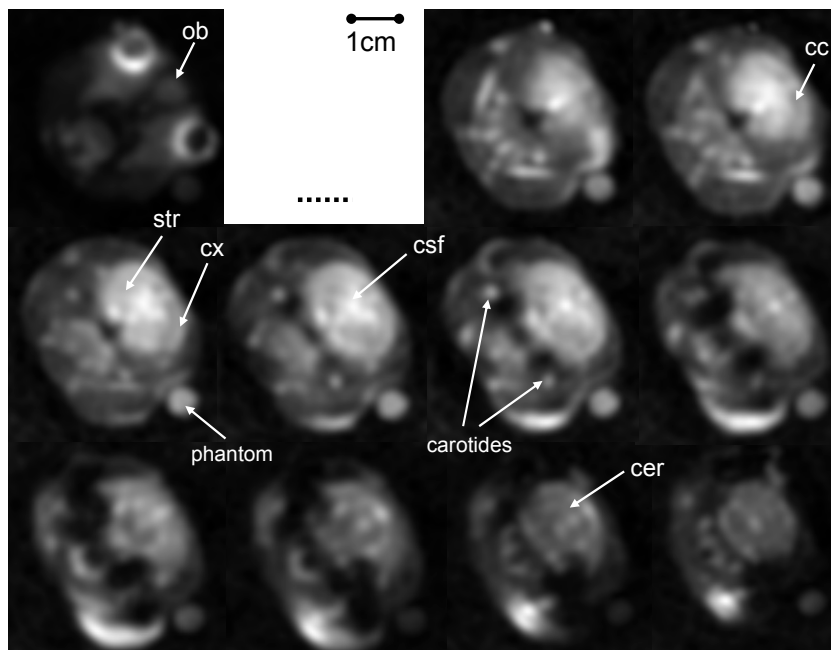
Figure 4.12: Axial sodium images from a 3D DWCSI data set of a rat head with 32768 PE steps. Besides the eyes, the carotids and other anatomical details of the head the brain with some substructures could be resolved. (ob = olfactory bulb; cc = corpus callosum; cx = cortex; striatum (str); cerebellum (cer); carotid arteries and the 50mM NaCl phantom are marked with arrows.

Discussion

Due to the good contrast to noise ratio in the proton RARE images very detailed information on the brain structure could be achieved. Images with higher resolution are shown in chapter 6. The quality of the images shown here is sufficient to perform a comparison between the proton and the sodium images.

The sodium DWCSI of the rat brain shows much more detailed information compared to recent studies [58], [59]. While the structures of the brain are blurred in the image with 43 μL voxel size due to the partial volume effect the outlines of the brain and the other structures of the head can already be recognized in the image with a voxel size of 6 μL in the 8k PE steps data sets. Good examples of the partial volume effect are the carotid arteries marked with an arrow in Figure 4.12. While they are broadened in the image with 43μL voxel size they become smaller the better the resolution of the data set gets. A partial volume correction can be done when proton images of the same image slice are available as shown in [91]. Although the SNR in the 6 μL image is very low it is sufficient to distinguish the major structures in the head.

The 32k PE steps data set with a resolution of 5 μL shows detailed information of the brain with a high SNR. A comparison of a slice from the proton and the sodium data set is shown in Figure 4.13. Regions that are clearly distinguishable in the sodium image are cx, str, csf, and the carotid arteries. In other slices the ob and the cer as shown in Figure 4.12 can be outlined. Due to the size of the cc (~0.6 mm diameter) only traces can be observed in Figure 4.12.
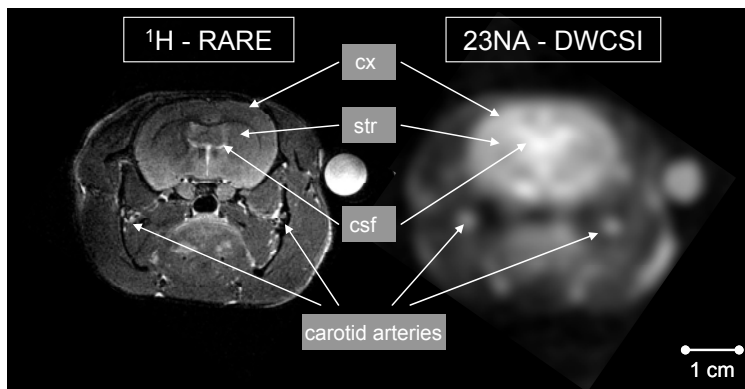
Figure 4.13: Comparison of an axial slice of the 1H RARE and the 23Na 3D DWCSI data set (32768 PE steps). (cx = cortex; str = striatum; csf = cerebro spinal fluid). Good concordance between sodium and proton images can be seen.

4.3.2 Sodium MRI of a Stroke Model in the Rat Brain

Material and Methods

During surgery ischemia was induced in the brain of Wistar rats with a weight of up to 200 g by permanent occlusion of the middle cerebral artery. Sodium and proton imaging was performed subsequent to and after recovery on days zero, three, and seven post operation. The animal handling for this study is described in chapter 4.3.1. Both Bruker resonators, the 38 mm birdcage for proton and the one for sodium were used to achieve proton reference RARE/FLASH and 3D DWCSI sodium images. Because of the size of the resonators the study was conducted in the MINI 0.5 gradient system.

To keep the anesthesia time of the animal for the MRI experiments as short as possible the total time used for proton MRI was less than 30 minutes. The acquisition parameters for the RARE sequence were: FOV = (30 (or 35) mm)^2; matrix = (256)^2; RES = 117 (or 137) μm; Slice = 0.5 mm, NA = 2; RARE factor = 8; N_{slices} = 20; TE_{eff} = 29 ms; TR = 5 s; T_{exp} = 5 min 20 sec. As the FLASH images had the same results as the RARE images but show less contrast they are not shown.

Again because of the short time window for the examination only 3D DWCSI data sets with 8192 PE steps (one exception) were acquired. The achieved resolution was between 1.5 and 1.2 mm isotropic. The pre acquisition delay was around 500 μs. Scan time was 9/18 minutes while conducting 2/4 averages.

The total anesthesia for the animal was therefore less than 1 hour.

Results

Typical proton and sodium images from different time points are presented in Figure 4.14. The infarcted area can be clearly delineated in the RARE and the DWCSI images.

The RARE images show good contrast in the brain. The infarcted area could be clearly identified. Furthermore, grey and white matter and the brain cavities filled with CSF were distinguishable. The contrast between brain and infarcted area is slightly reduced at day 7 compared to day 0.

The sodium images show particularly the areas with elevated sodium concentration. On day 0, especially, the stroke and the wound from the operation have

a very high sodium concentration. On day 3 the sodium concentration of the wound is already reduced. Unfortunately the resolution on day 7 was chosen to be 1.2 mm isotropic leading to a reduced SNR. Nevertheless the infarcted area can still be seen.

Figure 4.14: Coronal images from proton 2D RARE (upper row) and corresponding sodium 3D DWCSI data sets of infarcted rat brains acquired at days 0, 3 and 7 after operation. The stroke can be localized in the proton and the sodium images during the whole time. A reduction of the sodium signal in the operation wound can already be seen on day 3.

One of the examined rats generated a cyst in the operated area. Figure 4.15. shows a comparison between proton RARE and sodium DWCSI images acquired with 32768 PE steps of this animal at day 9 after operation. The arrow heads show the infarcted area while the small arrows show the brain cavities and the small dashed arrows the cyst. The contrast in the proton images was high enough to delineate the stroke. The sodium images are slightly tilted in the axial plain compared to the proton images, which does not influence the information of the data. With 0.8 mm isotropic a very good resolution of the sodium images with a comparatively high SNR was achieved. As the "gradient on time" had to be extended, the pre acquisition delay was 675 μs. Compared to the proton images the cyst appears smaller in the sodium images, indicating a higher sodium content in the middle. The acquisition parameters can be found in the caption of Figure 4.15.
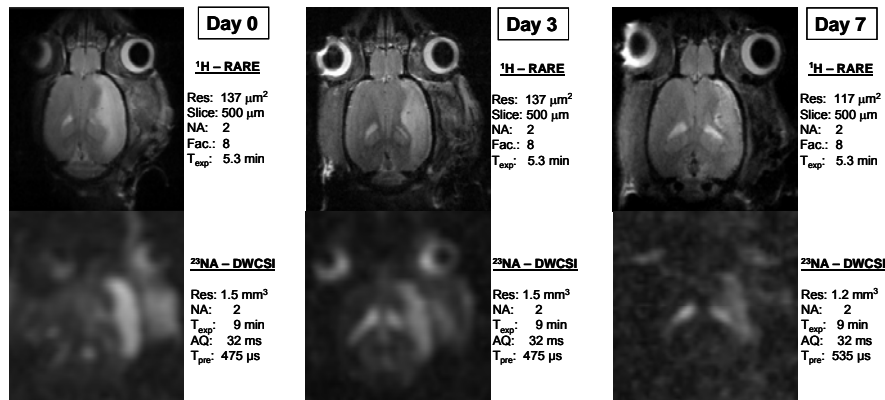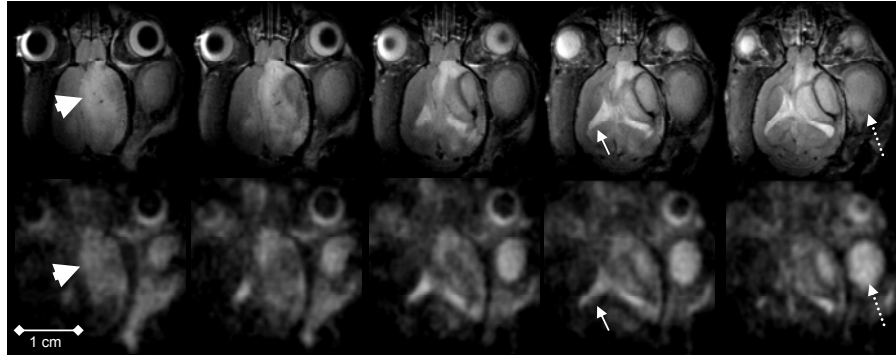
Figure 4.15: Coronal images from proton 2D RARE (upper row) and corresponding sodium 3D DWCSI data sets of infarcted rat brain and generated cyst acquired at day 9 after operation. The acquisition parameters for the RARE images are: FOV = (30 mm)^2; matrix = (256)^2; RES = 117 μm; Slice = 0.5 mm, NA = 2; RARE$_{factor}$ = 8; N$_{slices}$ = 20; TE$_{eff}$ = 29 ms; TR = 5 s; T$_{exp}$ = 5 min 20 sec. And for the DWCSI: 32786 PE steps; res = 0.8 mm^3; NA = 1; T$_{aqdel}$ = 675 μs; T$_{exp}$ = 36 min.

Discussion

Sodium imaging of the infarcted rat brain is shown in this chapter with a resolution of up to 800 μm isotropic. This data can be matched with the proton RARE images, showing consistency in the size of the affected area.

In their studies on strokes in primates and humans Thulborn et al [56] showed that the apparent diffusion coefficient (ADC) achieved by proton MRI decreased rapidly to about half the normal value after stroke induction and then stabilized with a slow decrease, giving no information about the progress of the severity of the injury. The total sodium concentration showed little change for the first 100 minutes after stroke induction and then increased at a constant rate. Their spatial and temporal resolutions were up to 64 mm^3 and less than 10 min. In our case with a resolution of 1.5 mm isotropic sodium images could be achieved in only 9 minutes, and therefore monitoring of the changes in the sodium signal can be conducted in rats in future studies. Tests for new drugs for example to reduce the damage of strokes can be carried out first on rats than on the much more costly studies on primates.

On day 0 the wound from the operation in Figure 4.15 has a very high sodium concentration due to the damaged tissue. In the following images the sodium tissue concentration in this area is reduced. Sodium MRI could therefore be an additional tool in wound healing.

Furthermore Lin et al [57] showed on a long term study of up to two weeks after infarction that sodium concentration may be a reliable marker for dead tissue. The T2 maps and the ADC maps show changes in their values that made it difficult to delineate the infarcted area over the two weeks of examination. As the SNR of the sodium measurements was very low they could not delineate the infarcted area and predict the final infarct volume. With our resolution (0.5 μL, 32786 PE steps, 36 min) more detailed studies could be performed and the sodium tissue concentration might lead to the prediction of final infarct sizes.

4.3.3 Sodium MRI of Stroke Models in the Mouse Brain

Material and Methods

Two different stroke models were applied to mice (15 – 18 g). In the first model the coronary artery of one side of the brain was closed by a thread for 90 minutes leading to a massive stroke of almost half of the brain. In the second model a smaller part of the brain is affected as the stroke is conducted by activating earlier injected radicals into the brain with a light source from the outside.

Animal handling for the MRI experiments (see chapter 3.3) was as usual. For proton imaging the 38 mm Bruker birdcage with the MINI 0.5 and for sodium the home build quadrature birdcage (see chapter 3.2.2) with the MICRO 2.5 gradient system were used.

Proton RARE images (in plane resolution: $(141 \ \mu m)^2$; slice thickness = 0.5 mm; Na = 1; TR = 5 s; rare factor = 4; T_{exp} = 2 min 40 sec) and highly diffusion weighted spin echo images (b = 1015/1700 s/mm^2; NA = 8/16; in plane resolution: $(141 \ \mu m)^2$; slice thickness = 1 mm; TR = 1 s; T_{exp} = 34 min) were acquired as references.

Sodium 3D DWCSI with 32768 PE steps (resolution up to $(0.7 \times 0.7 \times 1 \ mm^3)$; $T_{acq-delay}$ = 275 μs; T_{exp} = 40 min) was conducted on the first model before the mouse had to be sacrificed due to the increasing size of the stroke. The second model with the smaller infarcted area was examined on day 8, 10 and 15 after stroke. The acquisition parameters were similar to those of the first model. Three dimensional T1 maps of sodium were acquired on day 10 and 15 after infarction with DWCSI. The total scan time for one T1 map was about 2h and 45

min (res = 1.3 x 1.3 x 1.3 mm^3). To minimize the repetition time and therefore the overall scan time a suppression module consisting of three 90-degree block pulses with additional spoiling after each pulse was used instead of the inversion recovery method described in chapter 4.2.2. After saturation, eight time points (20/40/60/80/100/ 125/200/300 ms) were acquired and a three parameter fit on a point by point basis was conducted on the reconstructed images as described in chapter 4.2.2.

Results

Four axial slices from the stroke occlusion model of the mouse brain acquired with the proton RARE sequence (left), the proton diffusion spin echo sequence DIFFSE (middle), and the 3D DWCSI sodium sequence (right) are shown in Figure 4.16.
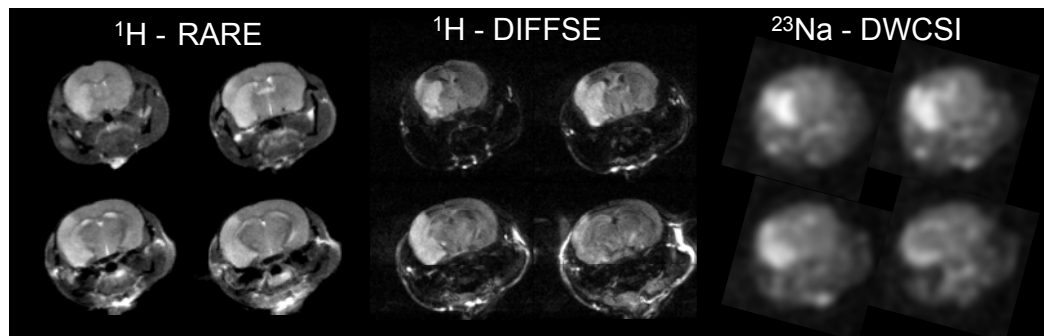
Figure 4.16: Comparison of axial RARE (left), diffusion weighted spin echo (middle) and sodium DWCSI images of the infarcted mouse brain. The stroke was induced by a 90 minutes occlusion of the coronary artery. The infarcted area can be localized in all three image sequences.

The RARE images give detailed information about the brain structure. The outline of the infarcted area in the left brain hemisphere can be defined due to the higher SNR of that region. The highly diffusion weighted proton spin echo images show the same results as the RARE images except the lower SNR in the healthy brain and the better contrast between infarcted and healthy brain areas. The brain, the ventricles and the infarcted area are clearly distinguishable in the sodium images.

The radical stroke model (Figure 4.17.) shows a smaller size of the infarcted area in all three different imaging sequences. The sodium images were acquired on day eight after stroke, showing to the lower left of the left hemisphere an additional hyper intense area (right sodium image).
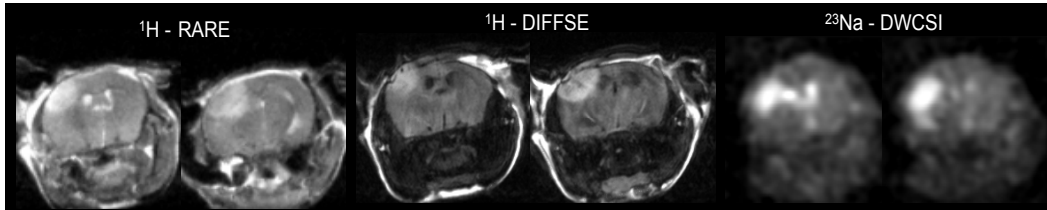
Figure 4.17: Comparison of axial RARE (left), diffusion weighted spin echo (middle) and sodium DWCSI images of the infarcted mouse brain. In this case the stroke was conducted due to an activation of injected radicals in the brain. The infarcted area can be localized in all three image sequences.

The results of the T1 measurements on day 15 after surgery are shown in Figure 4.18 and the achieved values of T1 from the different brain regions measured at day ten and fifteen are shown in Table 4.1. The T1 value in the infarcted region is elevated compared to the one in the healthy hemisphere of the brain.
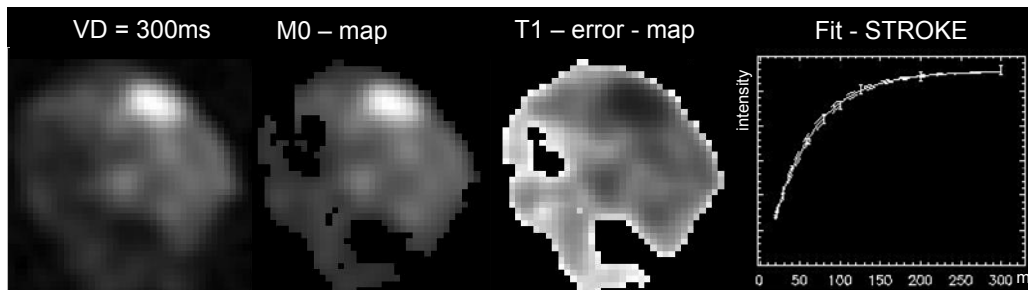
Figure 4.18: Sodium DWCSI saturation recovery T1 measurement of the infarcted mouse brain. From left to right: An image 300ms after saturation, the M0 – map, the errors of the T1 fit and a representative fit from the infarcted area are shown.

10 days after stroke			
	STROKE	BRAIN	CSF
T1	58 ± 5 ms	40 ± 2 ms	55 ± 4 ms
15 days after stroke			
	STROKE	BRAIN	CSF
T1	53 ± 3 ms	44 ± 2 ms	56 ± 5 ms

Table 4.1: Sodium T1 values of the infarcted mouse measured on day 10 and 15 after stroke. The values given are averages over a region of interest.

Discussion

At 17.6 Tesla it is possible to delineate the infarcted area in both stroke models with proton RARE imaging in a very short time. Diffusion imaging can be used to get a more precise delineation of the stroke, but requiring a longer acquisition time as the diffusion gradients lower the signal in the image. Therefore in most cases it might be sufficient to use fast RARE imaging with longer echo times if the evaluation of the size of the stroke is needed.

It is the first time that sodium imaging of the mouse brain has been reported. Compared to the size of the brain (~ 1.5 cm in diameter) the resolution with up to 0.7 x 0.7 x 1.0 mm^3 is still coarse. Nevertheless the brain, the brain chambers and the infarcted area can be delineated. As the weight of the mice was only between 15 – 18 g, it should be possible to resolve more details when using adult mice with a weight of around 30 g and a slightly bigger brain.

An additional improvement of the localization in future studies could be achieved by using proton images, generating a mask for the areas of interest from those images and taking the partial volume effect into account as described in [91].

As the cell structure is destroyed during a stroke and the intracellular space decreases while the extracellular space increases a rise in tissue sodium concentration is found in the infarcted area (left image Figure 4.18) and at the same time a rise in T1 was observed. As the T1 of the infarcted area has the same

values as the T1 of CSF an almost total destruction of the cells might have happened. Yet the T1 of the CSF has to be discussed critically because the partial volume effect in this case can not be neglected due to the size of the brain chambers. To evaluate this, further studies have to be performed including measuring of T2 and histopathology.

The overall results of the T1 measurement concur with the values reported in several other studies measured at different field strength and various animals. An overview can be found in Table 4.2.

`	animal	field	healthy	infarct	CSF	ROI
Schepkin et al	rat	9.4 T	38.1 ± 1.5			8 μl
Lin et al	rat	4.7 T	60	60		not published
Goodman et al	rat	4.7 T	40 ± 5			800 μl
Our study	mouse	17.6 T	42 ± 2	56 ± 4	56 ± 5	2 μl

Table 4.2: Sodium T1 values from the brain of various animals. The values are taken from references [92], [57], and [37] .

4.4 **The Mouse Heart – a feasibility Study**

Introduction

Substantial progress in cardiac magnetic resonance imaging (MRI) and spectroscopy of small animals has occurred in recent years. In particular, many of the technical challenges associated with imaging of the murine heart have been tackled [93]. These developments have resulted in a number of studies of normal cardiac function, and changes associated with myocardial infarcts or other pathological conditions [94]. Acquisition of data from the mouse, in particular, is important due to the widespread availability of transgenic animals. Studies on mice have concentrated thus far on morphological changes, which can be detected either on anatomical images, or via changes in the dynamic motion of the heart. The next logical step in technique development is to acquire data which contain metabolic information. As such, the acquisition of sodium images is a promising approach. For example, previous studies in rabbits have shown that localization of myocardial infarcted areas can been performed by observing changes in the magnitude of the sodium signal [95]. However, there are considerable more technical difficulties in acquiring sodium data from the murine heart than from the murine brain: high spatial resolution is necessary to differentiate structures within the mouse heart, which has a total volume of approximately one cubic centimeter. A more general difficulty in imaging the mouse heart is the motion due to the very fast heartbeat (up to 600 beats per minute). So far, in vivo cardiac sodium studies have been limited to humans [96], [97], dogs [98], [99] or rabbits [95]. Sodium imaging has been performed on isolated rat hearts [100], but no sodium in vivo studies on murine hearts have been reported. In this chapter, we show the first high resolution sodium images of the mouse heart, which were acquired at 17.6 tesla using the optimized 3D DWCSI sequence, with custom-built cardiac gating unit and radiofrequency coil. Images with a three-dimensional isotropic spatial resolution of 1 x 1 x 1 mm have been acquired in approximately 1.5 hours measurement time.

Material and Methods

Experiments were performed using the resonators described in chapter 3.2.1 and 3.2.3 and the MINI 0.5 gradient system (maximum gradient strength: 200 mT/m). Mice (20-25 g) were anesthetized using a continuous flow of isoflurane (1.5-2%) at a gas flow of 17 ml/second. After positioning the mouse in the animal handling system and the proton radiofrequency coil, dynamic images of the heart were acquired using a fast low angle shot (FLASH) CINE sequence [101], comprising 128 segments of FLASH images with an echo time of 1.9 ms. Approximately 15 frames per heartbeat were acquired with an in-plane spatial resolution of 300 x 300 µm, and a slice thickness of 800 µm. Eight signal averages were acquired for a total data acquisition time of 6 minutes. These images were used to assess both the motion of the heart, and also for subsequent correlation of the proton and sodium images. Triggering was performed on the heart beat and the breathing of the animal were monitored

After the short axis proton CINE images of the heart were acquired, the proton coil was replaced by the sodium coil. 3D DWCSI was conducted using a non-selective excitation pulse (80 µs), a TR of 26 ms, and rapid gradient switching allowed the minimum effective echo time for this system (~720 µs) to be used. A total of 32,768 k-space data points were acquired, with 256 complex time-domain points per free induction decay (FID), and two signal averages. Since respiratory and ECG triggering were needed to acquire data from the anesthetized mouse, the total data acquisition time was approximately 1.5 hours (2 FIDs acquired per heartbeat). Data processing was performed as described in chapter 4.1.2 (exponential filter: 10 Hz line - broadening; zero-filling in spatial dimensions by a factor of 2). In order to reduce the resulting four dimensional data array to three dimensions either sum-of-square images of the relevant points in the spectral dimension were calculated, or simple integration over the same bandwidth was performed. The SNR of the sodium signal in different areas was obtained by defining regions of interest (ROIs) in the left and right ventricle and the myocardium/septum. With this information the ratio of the sodium concentration in blood and in myocardium was estimated, as has been measured by other groups in larger animals.

<u>Results</u>

Proton images of healthy mice allowed identification of the anatomy of the heart and major vessels in the animal. Figure 4.19(a) shows a short axis view of a mouse heart from the CINE data sets. The ventricles and the myocardium can be seen with a good contrast-to-noise. Figure 4.19(b) shows a long axis view of the same heart. Figure 4.19(c) shows the short axis slice from the 3D sodium density weighted CSI dataset corresponding to the proton image in Figure 4.19(a), and Figure 4.19(d) shows the long axis view from the sodium data set corresponding to Figure 4.19(b). Due to the breathing of the mouse only eight out of every ten heartbeats could be used for data acquisition. With these restrictions, and acquiring two signal averages, the total scan time was about 1.5 hours. In the sodium images the left ventricle (LV) and right ventricle (RV) are clearly distinguishable. The septum and parts of the rest of the myocardium can be seen in both figures Figure 4.19(c) and Figure 4.19(d). The papillary muscles can also be identified in the short axis slice.
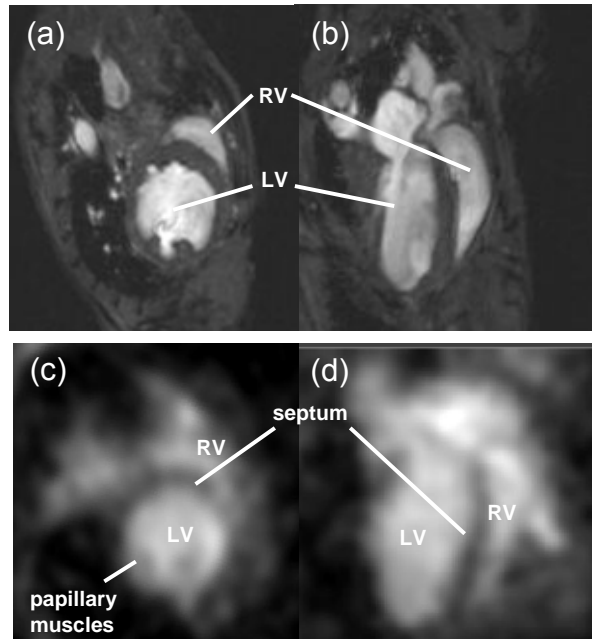
Figure 4.19: Short and long axis views from a mouse heart. (**a**) and (**b**) are short and long axis views from the proton CINE datasets. (**c**) and (**d**) are corresponding slices from the 3D density-weighted sodium dataset. The left and right ventricle, the septum, and some parts of the left ventricular free wall are distinguishable, as are the papillary muscles in (**c**). Data acquisition parameters for the sodium images: 256 complex time-domain data points, a spectral width of 11 kHz, the acquisition time 23ms, echo time 720μs, 2ms gradient spoiling and a repetition time of 26ms. An exponential filter of 10 Hz was used in the spectroscopic direction, and zero-filling by a factor of two in each spatial dimension of the data set. A sum-of-squares reconstruction was performed on the 32 spectral data points around the highest peak

Figure 4.20 shows six short axis views from a different data set. The SNR of the RV, LV, left ventricular free wall (where visible) and the septum, were measured by using regions in the center of each compartment in order to reduce errors associated with tissue edges. The calculated SNRs were LV: 9.2 ± 2.3; RV: 8.3 ± 2.06; left ventricular free wall: 3.8 ± 1.0 and septum: 5.6 ± 1.4. Using these figures, the myocardial/blood sodium concentration ratio in the left ventricle was calculated to be 0.42 ± 0.16 and for the right ventricle 0.46 ± 0.15. These values compare well with a theoretical value of 0.45, and experimental value of 0.46 obtained in humans [96]. As in previous publications one must be careful in interpreting these values since differential relaxation times can give rise to signal intensity differences. In our sequence, since the echo time used was so short, errors introduced by differential T_2 values are only of the order of a few percent,

as signal loss is only relevant for the intracellular space. As in reference [96], the repetition time used was much shorter than the sodium T_1 value, and so a correction for T_1 should ideally be made. However, it is extremely difficult to measure T_1 values in the heart in vivo, and so uncorrected values were used as in [96]. The fact that the experimental and theoretical ratios are very similar, both in this study and in reference [96], strongly suggests that a T_1 correction would have only a small effect on quantitation.
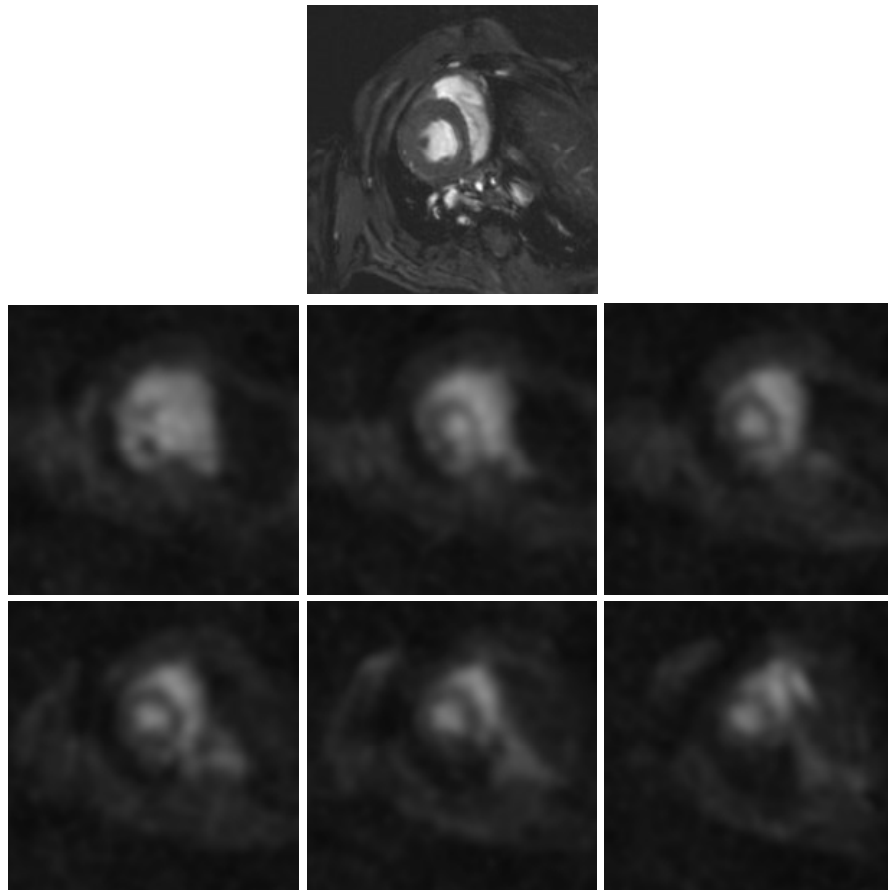
Figure 4.20: Six short axis sodium images from a second mouse. These data were used to calculate the SNR values of the different spatial compartments. The top image is a proton image from a CINE dataset from the same mouse.

Since the sodium dataset is spatially isotropic, it is possible to perform a full 3D reconstruction of the data as shown in Figure 4.21. Segmentation and visualization were performed using the Amira software package (Indeed - Visual Concepts GmbH, Berlin). Next to the right and left ventricles, the atrium can be seen clearly. The major vessels of the mouse heart, such as the aorta, can be followed throughout the 3D reconstructed volume: the aortic arch is particularly well defined in the sodium images.
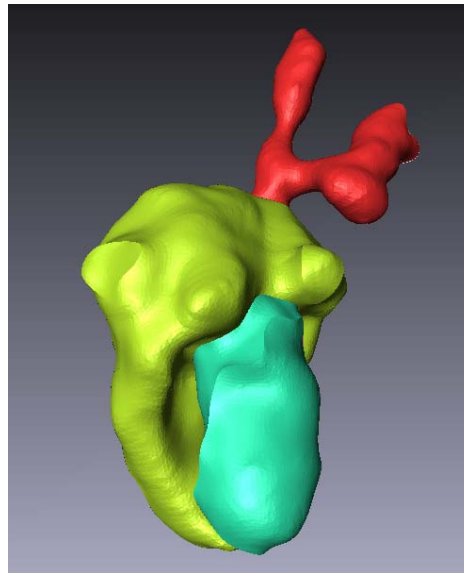
Figure 4.21: Three-dimensional surface reconstruction of a sodium dataset. Identifiable regions are the left ventricle (*dark green*) and right ventricle (*light green*) blood chambers, atrium and aorta including the aortic arch (*red*)

Discussion

This study has shown the first sodium images of the mouse heart in vivo, acquired with an isotropic voxel resolution of 1 x 1 x 1 mm, and a signal-to-noise ratio of ~10:1 in the ventricles, within 1.5 hours data acquisition time. The ventricles, septum and myocardium are clearly distinguishable in these images. The calculated ratios of the sodium concentration in the myocardium and in the blood are in good agreement with values in the literature.

The spatial resolution achieved, while useful, is still too poor to be able to resolve some features of interest within the heart. Using the MINI 0.5 gradient system, this resolution is limited by the maximum gradient strength of 200 mT/m. For future studies the newly designed resonator (chapter 3.2.2) with an outer diameter of 39 mm and therefore the stronger MICRO 2.5 (1000 mT/m) gradient system could be used, increasing both the spatial resolution and the SNR.

Since the sodium concentration in infarcted areas of the heart increases by about 200% [95] infarcts in mice would be easily visible with our setup. Therefore, application of density-weighted CSI with optimized instrumentation at high magnetic fields should allow investigation of mouse cardiac models by sodium imaging. This adds a valuable tool to cardiac diagnosis that has so far only been available for models in dogs or rabbits.

4.5 **Renal Imaging of the Mouse**

<u>Introduction</u>

Since the first studies in 1984 [102] renal proton MRI has become increasingly important. Today it allows for a comprehensive examination of almost the complete spectrum of urologic diseases, including congenital malformations in humans [103]. But not only the nephropathy is of interest, functional parameters such as glomerular filtration, tubular concentration and transit, blood volume and perfusion, diffusion, and oxygenation can be measured non invasively with MRI [104]. Many studies have been performed on animals investigating, for example, essential hypertension linked to kidney malfunction in rats.[105], [106].

Until now sodium MRI of the human kidney has been of little importance because of the low achievable SNR. Examples of human renal images can be found in [107]. The first sodium MRI animal studies were performed on rabbits and guinea pigs. Recently studies on rats were published by Maril et al [108], [109], [110]. The particular interest in sodium MRI is due to the extra cellular corticomedullary sodium concentration gradient which regulates the fluid homeostasis. This concentration gradient is the driving force behind the reabsorption of water from the filtrate back into the plasma. Before the studies of Maril et al. only invasive methods such as micropuncture [111] or slice section procedures [112] had been applied to determine the sodium changes in the kidneys of rats. Since the mouse has become the most important animal model for human disease the aim of our study is the monitoring of the changes of the sodium concentration in the kidneys of the mouse during induced diuresis with our setup.

4.5.1 The kidney function

The kidney consists of three main parts, the renal cortex, the renal medulla and the renal pelvis. The basic functional unit of the kidney is the nephron, of which there are more than a million in each normal human adult kidney. They are located in the cortex except for parts of the so-called loop of Henle which descends into the renal medulla. The nephrons regulate the water and soluble matter in the body. In the glomerula, a part of the nephron, the blood is ultra

filtered and water and small solutes are washed out. In the loop of Henel a countercurrent exchange takes place and necessary fluid and molecules are reabsorbed. In this way the pH of the blood is regulated to 7.4. The urine produced is than transported from the loop of Henel into larger ducts, flows into the renal pelvis, and finally excretes through the ureter into the bladder.
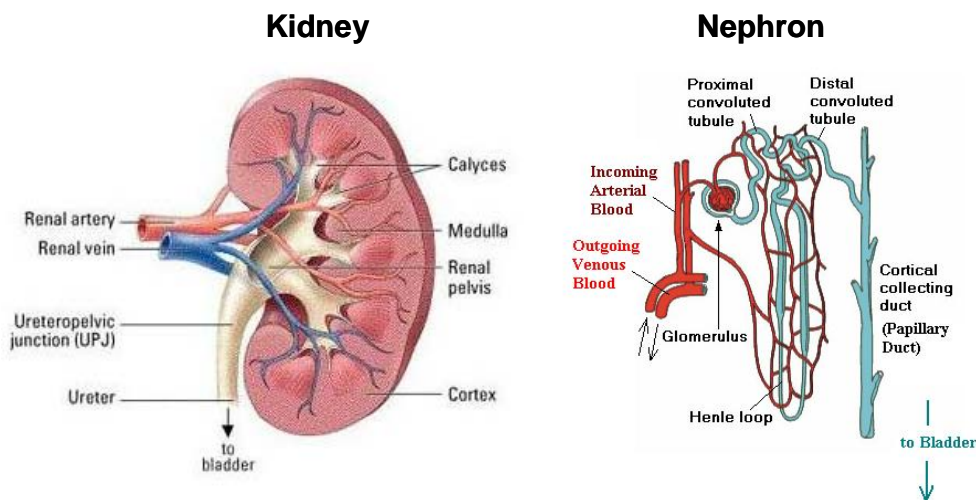
Figure 4.22: Scheme of an intact kidney (from: **http://faculty.washington .edu/zeman/kidney.jpg**) on the left side and one of the approximately one million nephrons contained in a human kidney (from**: http://members.tripod.com/vzajic/nephron.jpg**) on the right side.

In the normal kidney a linear sodium gradient exists from the outer cortex to the inner medulla. Compared to the human kidney (size: 11 cm long and about 5 cm thick, weight: 150 grams) the kidney of the mouse (240 mg) is with about 1 cm in length and 0.5 cm in width relatively huge.

4.5.2 Feasibility of renal mouse MRI

Material and Methods

All experiments were performed on adult healthy NMRI mice (Charles River, Sulzfeld, Germany) with a weight between 20 and 30 g. The mice were anesthetized with a mixture of carbogen and isoflurane (1.5%). To monitor the health state of the mouse the trigger unit was used. In the case of proton MRI the 38 mm Ø eight leg birdcage resonator as described in chapter 3.2.3 and in

the case of sodium MRI the homebuilt resonators as described in chapter 3.2.1 and 3.2.2 were used. Dependant on the size of the resonator the respective gradient system was chosen.

Proton MRI

In the case of proton MRI a 3D FLASH sequence was first used to visualize the kidneys. As the focus of this study lies on sodium only, images with a coarse resolution of 230 x 170 x 170 μm^3 in 16.5 min were acquired. The echo time was 1.7 ms, the repetition time was 60ms and the flip angle about 15°. A coronal slice after zero filling by a factor of 2 from a 3D proton FLASH image of the kidneys from a mouse is shown in Figure 4.23 (left). The two kidneys with some of the blood vessels are clearly distinguishable. As there were no details in the kidney visible a RARE sequence with an in plane resolution of 125 x 256 μm (slice: 500 μm) was performed on a different mouse. With an RARE factor of 8 and an average echo time of 23.1 ms (TR = 4s, FOV = 16 x 25 mm^2, NA = 4, T_{exp} = 7min) more details, especially on the right kidney, can be seen. The renal pelvis, structures from the medulla and the cortex are distinguishable.
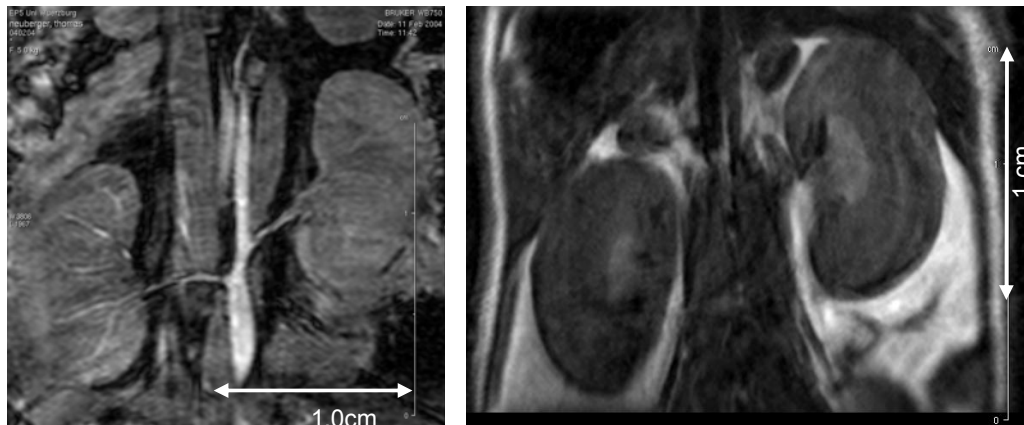
Figure 4.23: A coronal slice from a 3D FLASH data set of the kidneys of a mouse (left) and a slice from a multi slice RARE data set with a T2 contrast from a different mouse. The RARE image shows more details of the kidney, while the FLASH image pronounces the blood vessels.

Sodium MRI

A critical point for sodium imaging is the positioning of the mouse in the resonator as no reference proton image could be taken with the single resonant home built coils. The probe base and the resonator are either one part (in the case of the 27 mm birdcage) or, in the detachable system (38 mm bird cage), no proton resonator was available. Three dimensional density weighted sodium CSI either with 8192 or 32768 phase encoding steps with different resolutions was applied to analyze the achievable information about the sodium distribution in the kidneys. The reconstruction of the data was performed as described in chapter 4.1.2.
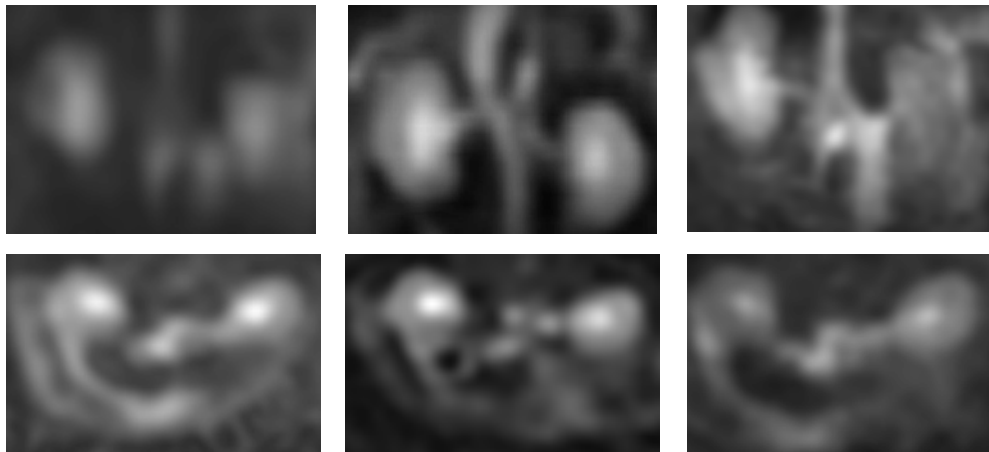
Figure 4.24: Three coronal (upper row) slices and a corresponding axial slice from 3D density weighted CSI data sets of mice kidneys with different resolution. From left to right the resolutions are 1.4x1.4x2.9 mm³, (1.5 mm)³, and. (1.0 mm)³

Figure 4.24 shows three coronal slices (upper row) and a corresponding axial slice (lower row) with different resolutions and imaging parameters. The left images with a resolution of 1.4 x 1.4 x 2.9 mm³ are slices from a data set with 8192 phase encoding steps and a total scan time of 7.7 min (SWH = 4960 Hz, TD = 512, NS = 1, TR = 57 ms). In the middle images, keeping the number of phase encoding steps the same, the resolution is 1.5 mm in all three dimensions. The total scan time was 38.4 min because of the relatively long TR of 281 ms (SWH = 4000 Hz, TD = 512, NS = 1). The right images are from a

data set with 32768 phase encoding steps. The resolution is (1 mm)³ and the total scan time was 1h and 3min.

Results of the sodium MRI

The kidneys and some of the major blood vessels are visible in all three image data sets. Due to the 'cylindrical shape' of the kidneys the poor z resolution in the left images of Figure 4.24 is of little consequence. The axial plane with a resolution of (1.4 mm)² shows a viable difference between the inner (medulla) and outer (cortex) kidney. On the left side of Figure 4.25 a profile from the cortex to the inner medulla along the corticomedullary axis (x – direction) and the adjacent profiles to the upper kidney (blue box) are shown. It can be seen that the sodium signal increases from the cortex to the inner medulla.
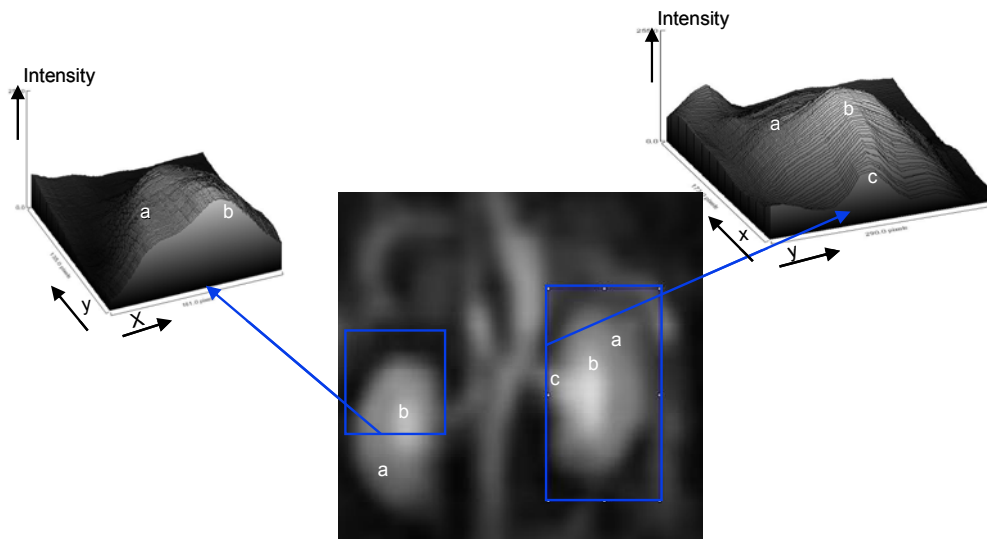
Figure 4.25: Three coronal slices from 3D density weighted CSI data sets of mice kidneys with different resolution. From left to right the resolutions are 1.4x1.4x2.9 mm³, (1.5 mm)³, and. (1.0 mm)³

The right side of Figure 4.25 shows profiles from the renal pelvis to the outer cortex orthogonal to the orientation of the profiles shown on the left side.

Five profiles from the left kidney with the corresponding axial image in different heights are shown in Figure 4.26. Again the achieved signal can be assigned to

the cortex (a), the medulla with the pelvis (b), and a mixture of the afferent and abducent blood vessels and the ureter (c). While the sodium signal rises from the outer cortex to the outer medulla by a factor of three, the increase from the outer cortex to the inner medulla and the pelvis is about a factor of six.
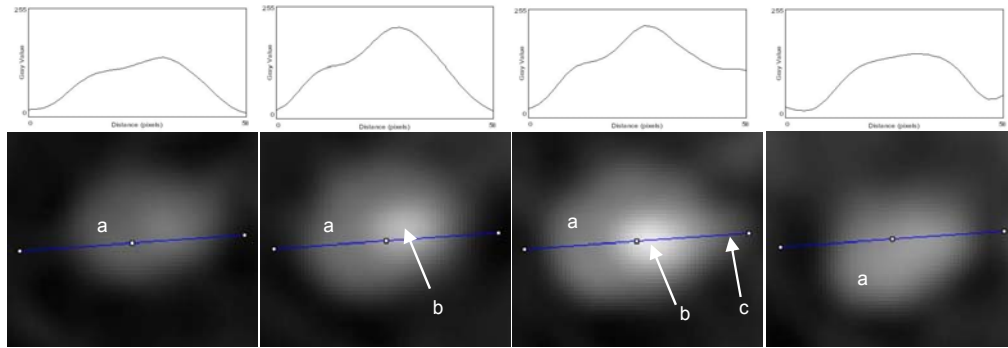
Figure 4.26: Four axial slices of the left kidney from a 3D density weighted CSI data set in different heights (lower row) and the profiles along the corticomedullary axis (blue line) is plotted in the upper row.

Discussion:

The kidney is responsible on the one hand side for the conservation of the water supply and on the other hand side for the regulation of the excretion and reabsorption of solutes in the body. Unlike other organs, where the inner cellular sodium concentration is about a factor ten lower than the outer cellular concentration, the kidneys have an additional active regulation of extra cellular sodium concentration on the organ level. This regulation mechanism is responsible for an increase in sodium concentration from the renal cortex to the renal medulla.

Due to the size of the mouse kidney and the achieved resolution partial volume effects at the edges between the different tissues occur and the boundaries are not distinct. Nevertheless, our images do not show the linear gradient from the outer cortex to the inner medulla as described in [108] and [109]. The difference between cortex and medulla is not linear.

The maximum corresponds to the inner medulla and the pelvis (where existing). This hypertonicity is due to the accumulation of fluid in the interstitium as well as

in the structures of the medulla, including the loops of Henle, the urine collecting ducts, and the vasculature.

Our results show that sodium MRI can be used to monitor the distribution of sodium in the mouse kidney. Hence, temporal changes in the sodium distribution or pathologies of the kidneys can be investigated with our setup.

By using an external standard as reference even the determination of the total sodium concentration would be possible. The necessary T1 and T2 times of sodium in the tissue and the standard for relaxation correction can be measured as described in chapter 4.2.2 and 4.2.3.

4.5.3 The sodium signal during diuresis: A time course study

Introduction

To investigate the capability of this method to monitor changes of the sodium distribution in the kidney of the mouse, loop diuresis was induced with furosemide as diureticum. Furosemide blocks the $Na^+/K^+/2Cl^-$ cotransporter in the apical membrane of the thick segment of the medullary ascending limb [113] and a "wash out" of sodium in the medulla occurs. Furthermore the cortical total sodium concentration increases [114]. Hence, this method can provide a non – invasive tool for assessing renal function of mice.

Material and Methods

The mice and the mouse handling was the same as described in chapter 4.5.2 except that a tail vein access for the diureticum was implemented before the mouse was placed into the rf resonator and then into the magnet. The time between the establishing of the tail vein access and the injection of the diureticum was kept as short as possible (about 15 min.) to keep the access open. Lasix (Hoechst, Frankfurt, Germany) with furosemide as the active agent in a concentration of 10 mg/ml was used as diureticum. Diuresis was induced by a bolus injection (about 20 sec duration) of the furosemide solution at a dose of 10 mg/kg/wt into the tail vein of the mouse.

A series of 12 three dimensional DWCSI data sets were acquired to monitor the changes in the kidney. Due to the short repetition time (TR = 34.2 ms, SWH = 8000 Hz, TD = 512) the total acquisition time for one dataset was only 4min and 40 sec (PE =8192) resulting in a total experimental time of 56 min. The achieved resolution was 1.0 x 1.0 x 2.5 mm³. To have a pre administration state, the bolus was given after the first data set.

Each data set was reconstructed and zero filling by a factor of two in each of the four dimensions was performed. Profiles along the corticomedullary axis were analyzed and relative concentration changes during the time course were determined.
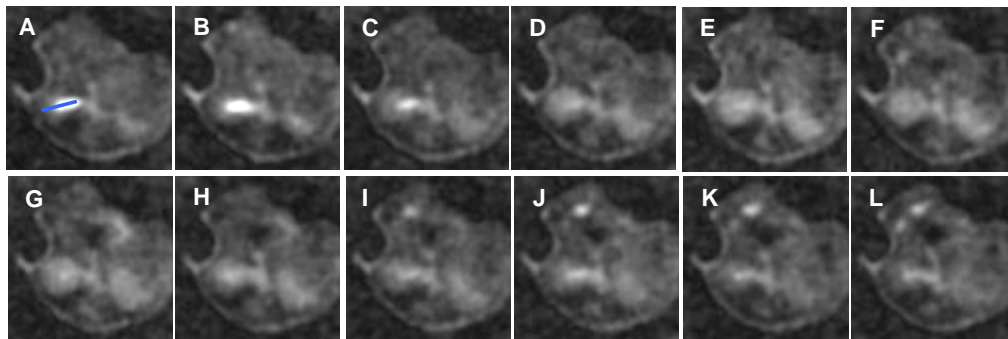
Figure4.27: Series of axial images of the same slice during diuresis. The diureticum was administered after the first data set. With a resolution of 1.0 x 1.0 x 2.5 mm³, each data set takes 4.7 minutes. A decrease in the medulla and a slightly increase in the cortex of the sodium signal can be observed. Blue bar in A: Corticomedullary axis of a mouse kidney.

Results: Kinetics of Diuresis

Changes in the renal sodium distribution during the administration of furosemide could be observed with a temporal resolution of 4min 40sec. Twelve axial slices at different time points, one before eleven after injection of furosemide, are shown from A to L in Figure 4.27. A decrease in the sodium signal in the medulla and an increase in the renal cortex can be observed. Figure 4.28 shows the profiles along the corticomedullary axis as indicated in Figure 4.27 (blue bar in A). Each pixel corresponds after zero filling to 0.25 mm. Fifteen minutes after the bolus injection the increase of the sodium signal in the renal

cortex is about 20%. Another 30 minutes later the signal is even lower than before the administration of furosemide. The sodium signal in the medulla, however, decreases to about 55% of the initial signal height after approximately 25 minutes (data set F-G). During the next 25 minutes the signal intensity of the medulla stays unchanged. This decay of the signal in the medulla could be exponentially fitted with a time constant of 6 +- 1 minutes (data not shown).
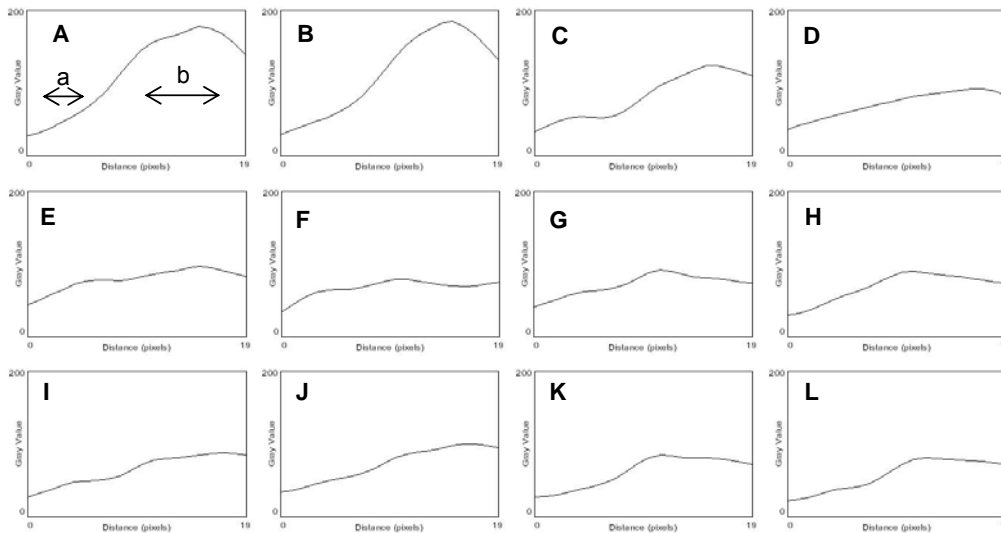
Figur4 4.28: Profiles along the corticomedullary axis of a mouse kidney during diuresis. The diureticum was administered after the first data set. A decrease in the medulla (b) and a slightly increase in the cortex (a) of the sodium signal can be observed. Even 45 minutes after administration a steady state has not been re-established.

Discussion of diuresis:

This study shows the application of sodium MRI during the administration of a loop diureticum on the mouse. It shows the great potential of sodium MRI to help us to understand how drugs influence renal function. Furosemide has two main effects on the sodium concentration in the kidney. Due to the inhibition of the absorption of Na^+ and Cl^- in the macula densa cells and the following reactions, the total sodium concentration increases in the kidney [114]. The second effect takes place in the medulla where the cotransport of $Na^+/K^+/2Cl^-$ is inhibited and the reabsorption of Na^+ and Cl^- is reduced resulting in a lower total

sodium concentration [115]. Both of these effects could be observed in our study. Despite the partial volume effects, the profiles along the corticomedullary axis show a huge decrease of the sodium signal in the medulla and a moderate increase in the cortex. After the administration of furosemide the effect is already seen in the next data set (C in Figure 4.27 and Figure 4.28) and an exponential decay of the sodium concentration could be fitted. The time constant of the decay is in accordance with [108] about 6 minutes. This investigation showed that time course studies of the changes in sodium concentrations in the kidneys with a spatial resolution of 1.0 x 1.0 x 2.5 mm³ and a temporal resolution of 4min 40sec can be performed on mice in vivo.

In general, it is possible with our setup not only to monitor the changes of the sodium concentration in the kidneys, but in any other organ where changes occur. The most interesting pathologies of this kind are probably stroke in the mouse brain as described in chapter 4.3.3 or the heart (see chapter 4.4).

Maril et al [108] conducted a similar study on rat kidneys. They used a three dimensional gradient echo sequence with short echo times (1.7 ms) to monitor the sodium distribution in healthy kidneys, as well as in pathologies. The effect of diuresis was investigated by the same authors in [109]. Their spatial resolution was 0.9 x 0.9 x 3.0 mm³ remarkably high, as they were working only at 4.7 Tesla. Nevertheless their study was concentrated only on one kidney as they were using a surface coils. To find the kidneys themselves and delineate the boarders of the kidney they had to use proton images because of the low signal to noise ratio.

A comparison between a three dimensional gradient echo sequence with a short echo time and the 3D DWCSI, both sequences with the same spatial resolution and scan time, yielded a higher SNR for the chemical shift imaging sequence. The reasons are the much shorter hard pulse for excitation and the shorter gradient encoding time of the CSI sequence, resulting in a pre acquisition delay far below 1 ms.

As the FOV of the 3D DWCSI sequence is still very high, a reduction of the phase encoding steps by a factor of two and a recalculation of the sampling points onto a smaller grid (64³ instead of 128³) would not only lead to a smaller, but still sufficient, FOV but also to a reduction of the scan time by a factor of two. This gain would allow one either to monitor processes with shorter time

constants or to improve the SNR by averaging or putting additional phase encoding steps into the sampling scheme.

To improve our setup and get an additional gain in SNR other resonators could be applied. Whether the use of surface coils would lead to a higher SNR at the region of interest in the mouse body is still under investigation. First results with proton resonators showed that an array with two surface coils [116] gives about 30% more signal within 1cm from the resonators than a commercially available bird cage. If this is also applicable for sodium and how big the gains would be is the subject of further studies.

Another resonator design of interest would be a double tuned resonator working on both, the proton and the sodium frequency. With the additional information of the proton images a partial volume correction of the sodium images could be performed.

4.5.4 T1 and T2 Measurements

Introduction

A further step to quantify the absolute total sodium concentration is the knowledge of the relaxation times. T1 and T2 can be measured as described in chapter 4.2.2 and 4.2.3. Both methods the global and the localization methods with the 3D DWCSI scheme were conducted. While the global methods give a rough estimation of T1 and T2 in the whole animal the localized CSI sequences allow for detailed differentiation in the mouse.

T1 measurement

For the analysis of the global inversion recovery method 16 data points after inversion times from 0.08 ms up to 1 s were used. With a repetition time of 300 ms and 16 signal averages the total scan time was less then 2 minutes. The achieved T1 was 38 ± 1 ms.

As the global T1 was less then 40 ms a repetition time for the CSI measurements (8192 phase encoding steps) of 150 ms was chosen, first to keep the total experimental time as short as possible and second to allow for nearly complete T1 relaxation before the next inversion. In total six experiments with differ-

ent inversion delays (0.002, 8, 15, 100, 250 ms) could be acquired in a total experimental time of 2h 47min. The resolution was 1.1 x 1.1 x 1.1 mm³. Reconstruction and fitting of the data were performed as described in chapter 4.2.2. The achieved T1 and the M_0 fit are shown in Figure 4.29.
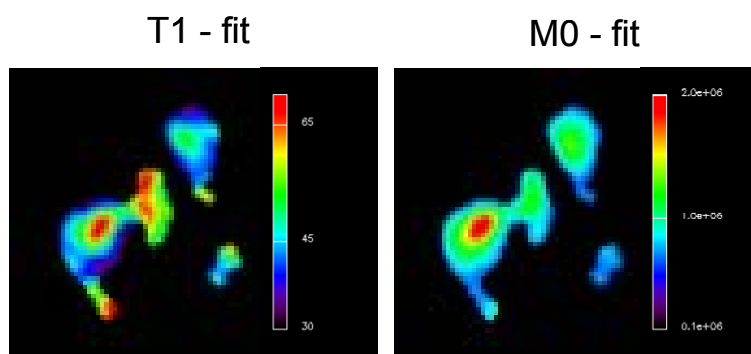
Figure 4.29: Slice from the T1 inversion recovery experiment. The left image is the T1 and the right image the corresponding M_0 fit. Six datasets with different inversion delays were acquired in 2h 47min.

Due to the fact that the kidneys are slightly shifted in an animal (see Figure 4.23) the cut is through the middle plane of only one kidney, while in the second kidney mainly the cortex is seen. The achieved T1 value in the cortex is 41 ± 4.0 ms (average of 82 pixels) and 67.9 ± 1.3 ms (average of 10 pixels) in the medulla. This result shows a clearly elevated T1 in the medulla of the kidney which might be due to the higher mobility of the sodium cations in this region of the kidney.

Compared to the global T1 measurements this values are slightly higher, but this is probably due to the fact that the global signal for the T1 measurements is an average of the whole mouse body in the resonator and not only the kidneys.

With a T1 of 41 ms (neglecting the small area of the medulla) the relaxation time is about a reasonable 20 % higher than the T1 measured in rat kidneys at 4.7T in [108] (although Maril et al. do not discuss their methods in detail).

Special care has to be taken if regions with flowing blood are of interest. As the rf resonator is not inverting the signal from the whole mouse, inflow effects may cause problems in the T1 fit.

T2 measurement

Preliminary localized T2 measurements were conducted on the mouse kidneys. The used 3D DWCSI sequence in spin echo mode (8192 PE) is described in chapter 4.2.3. Experiments with 10 variable echo times ranging from 2.9 to 42.7 ms were conducted in2 h and 37 min. The spatial resolution was 1.3 x 1.3 x 1.7 mm³ and the repetition time was depending on the echo time up to 115 ms. The long time-constant T_2 values were measured to be 29.2 ± 3.8 ms for the cortex and 36.1 ± 2.8 ms for the medulla, respectively. The fast T_2 time -constant of the bilinear fit were 0.8 ± 0.6 ms for the cortex and 1.0 ± 0.6 ms for the medulla region.

5   In Vivo Proton Spectroscopy

Proton MRI is limited to monitor the signal arising from protons of water molecules or fat. This is not surprising as water (concentration: 50 mM) and fat (concentration: depending on tissue) are the two main sources of protons in living tissue. Due to its ability to detect signal from protons of numerous tissue metabolites which have much lower concentrations (millimolar range), localized proton MR spectroscopy can be used to provide considerable biochemical information of tissues in vivo and in vitro not accessible for imaging. The majority of MRS experiments are conducted on the brain revealing non-invasively information about pathogenesis of several brain disorders. A summary of applications of MRS in the human brain can be found in Ross et al [49]. Furthermore, MRS can also be used to phenotype the increasing numbers of animal models of brain disease. Conducting these studies at very high magnetic fields (>9.4 tesla) benefits the SNR and spectral resolution, and, hence, can make proton MRS in rodents a valuable tool for researchers. The major problems that have to be overcome at increasing field strengths are the bigger chemical shift artifact, the possible presence of more eddy currents and a demand for higher shim strength due to the increasing susceptibility effects.

At these field strengths, however, knowledge of the relaxation times T1 and T2 is essential in order to conduct optimized experiments and to study changes induced by various pathogenic conditions. Previously, relaxation times of proton brain metabolites have predominantly been measured in rat models [117], [118], [119] at fields up to 11.7 Tesla. In our work we explore the feasibility to acquire highly resolved proton spectra and to measure the relaxation times T1 and T2 of the major metabolites in the mouse brain with scanner independent home written single voxel MRS methods at 11.7 and 17.6 tesla.

5.1 **Phantom Experiments**

5.1.1 Introduction

Before the *in vivo* experiments phantom experiments are conducted to ensure accurate localization of the single voxel proton MRS sequence and therefore to ensure that no signal contamination from outside the voxel is acquired during the experiment. Furthermore the essential water suppression had to be optimized, and to ease the in vivo shimming, the automatic shimming technique by mapping along projections (FASTMAP) [120] shimming routine had to be tested and the optimal parameters for a small voxel had to be found. In addition post processing was optimized to take for example the effects resulting from eddy currents into account. In order to quantify complex spectra the method described by Provencher (LC-model) [33] is often used and was available through the department of neuroradiology of the clinic of the university. For future work to actually quantify the spectra the necessary data base for 17.6 tesla was created.

5.1.2 Material and Method

MR-setup

For all proton spectroscopy experiments at 17.6 Tesla the home built birdcage (chapter 3.2.3) and the MINI 0.5 gradient system were used to ensure the same conditions in the phantom and *in vivo* experiments. The phantom itself consisted of a 10 mm diameter NMR tube inserted into a 20 mm diameter NMR tube. A solution of 10 mM Cre in the 10 mm and a100 mM NAA solution in the 20 mm tube were used to verify the localization properties of the sequence. For shimming, water suppression, and post processing considerations either a 200 mM GABA solution with 2 mM TSP (0 ppm) and 200 mM sodium formate (8.44 ppm) as references, a 50 mM Cre solution or pure water were poured into the 10 mm tube. The 20 mm tube contained only water.

To create a basis data set for the quantitative evaluation of spectra using the LC – model [33] spectra of 16 brain metabolites (Table 5.1) were acquired. To

avoid air bubbles, all solutions were degassed for at least 10 min at a pressure of less than 50 mbar. The temperature was adjusted to 20 degree Celsius using the gradient cooling unit.

MR-methods

To improve the B_0 field homogeneity inside the phantom the FASTMAP tool implemented by BRUKER was used. Special care had to be taken to choose the right starting parameters otherwise the routine would fail. A detailed description can be found in the Bruker online manual of Paravision.

For water suppression the CHESS sequence, described in chapter 2.8 was used. The three excitation pulses were frequency selective 10 ms sinc pulses with a band width of 621 Hz. To avoid signal refocusing spoiling gradients with a strength of 40 mT/m and a duration of 5 ms were applied asymmetrically as shown in Figure 5.6.

For single voxel spectroscopy the PRESS sequence [13] was chosen as this sequence has good localization properties and higher SNR than the comparable STEAM [121] sequence. The excitation pulses were frequency selective sinc pulses (90° -pulse: 1 ms / 6210 Hz bwdth; 180° - pulses: 1 ms / 4650 Hz bwdth) and the 40 mT/m spoilers surrounding the 180° - pulses were 1 ms long. The pulses were carefully adjusted manually (after the initial values from the Bruker "auto reference gain" method) by maximizing the acquired signal from a $(3 \text{ mm})^3$ voxel. The echo time was 15 ms and the acquisition time was, depending on the number of acquired points (8192 /16384 complex points) and the chosen band width (10000 /15000 Hz), between 1.1 and 3.3 seconds. The repetition time, at least 15 sec, was long enough to avoid T1 saturation effects. Since a 16 step phase cycle was used usually 16 averages were acquired resulting in a total experimental time of ≥ 4min.

5.1.3 Results

<u>Water suppression</u>

By applying the CHESS water suppression before the PRESS sequence the water signal was reduced from an SNR of ~1350 (receiver gain setting: 1000) in the unsuppressed to a value of ~57 (receiver gain setting: 25000) in the suppressed case. Taking the receiver gain setting into account the actual suppression was almost a factor 600 (see Figure 5.1).
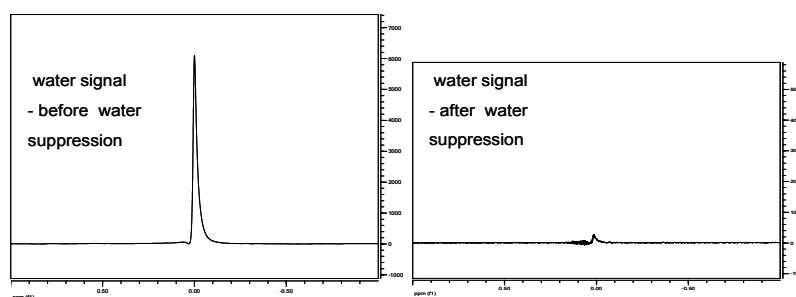
Figure 5.1: Spectra from a water phantom. The signal to noise ratio was about 600 times smaller in the suppressed spectrum (right) compared to the unsuppressed case (left).

<u>Shimming</u>

A manual global shim on the entire sample led to a line width of ~25 Hz. The optimal parameters for the FASTMAP routine by shimming on voxel sizes between $(3 - 5\ mm)^3$ were found to be: TR = 1s, band width = 6000 Hz, number of points along the projection 64, and a evolution time of 3 ms for the first run. In the next 2 -3 repetitions of FASTMAP the evolution time could be increased in the phantom experiment up to 60 ms. During those phantom experiments the second order shims were strong enough to compensate for inhomogeneity of the B0 field. The final line width of the water signal in the shimmed voxel was less than 3 Hz. Examples of achieved line widths of the metabolite resonances are shown for GABA in Figure 5.2. The five resonances from the GABA phantom for example, which resulted from J – coupling at around 1.88 ppm, are all

resolved. Evan the J –coupling constant of ~7 Hz [50] could be determined. Each peak had a line width of approximately 3 Hz.
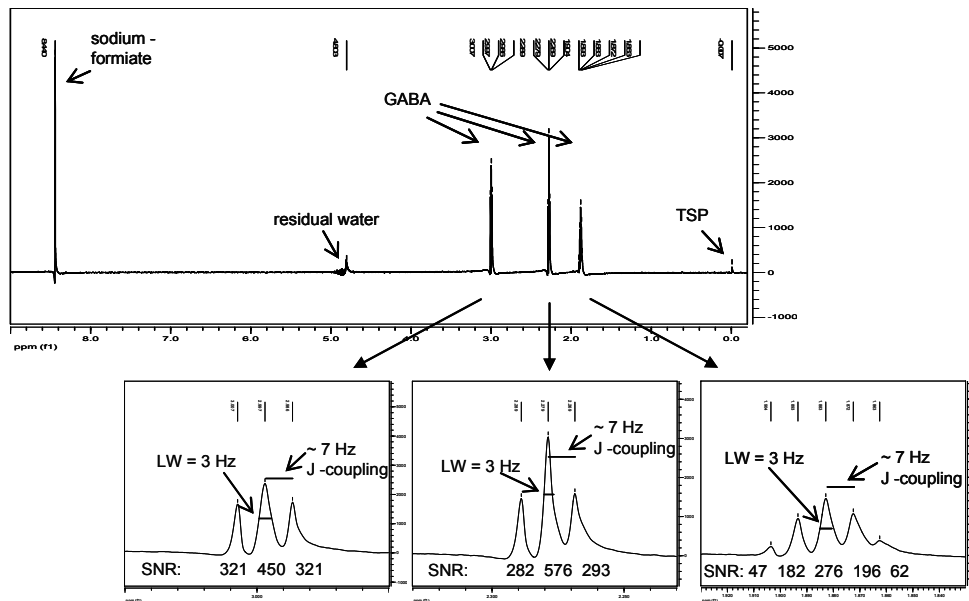
Figure 5.2: Spectrum from a 200 mM GABA solution with 2 mM TSP (0 ppm) and 200 mM sodium formate (8.44 ppm) as references (upper spectrum). The detailes in the lower row show the achieved SNR for the GABA resonances, their line width and the J – coupling constant

Localization

The localization of the PRESS sequence yielded no contamination from the surrounding NAA solution in the Cre spectrum (data not shown). With a voxel size of $(3mm)^3$ and a gradient strength for voxel selection being ≥ 19 %, the voxel shift due to chemical shift displacement (H_2O – Cre) was about 0.8 mm (see Equation 2.39).

Data reconstruction

All FIDs were zero filled by a factor of two and an exponential filter (lb = 1 Hz) was applied prior to Fourier transformation. Phase correction (first and second

order) was performed to yield the expected final spectra. Unfortunately, due to eddy currents the spectra could not be phased to achieve a Lorentzian/ Gaussian line shape. An additional eddy current correction using the phase of a water reference spectrum [32] had to be applied. A corrected creatine resonance is shown in Figure 5.3.
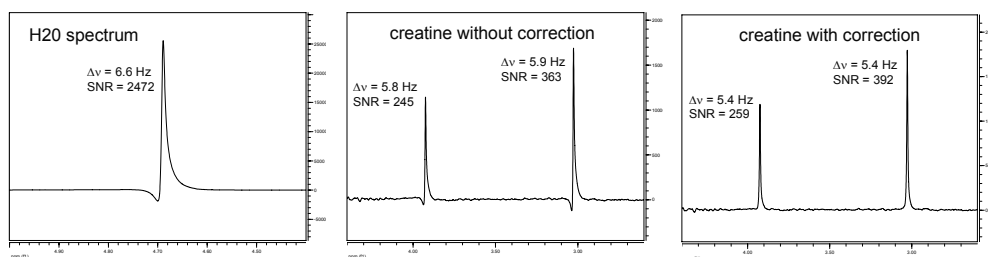
Figure 5.3: The spectrum to the right shows the final spectrum of the eddy current corrected, water suppressed creatine resonances (middle) using the phase of the unsuppressed water spectrum (left).

Data base spectra

Substance	Abbreviation	Concentration in mM
Alanine	Ala	100
Aspartate	Asp	40
Creatine	Cre	50
Carnitine	Car	50
Glucose	Glc	200
GABA	GABA	200
Glutamine	Gln	132
Glutathione	GSH	70
Glycine	Gly	200
myo-Inositol	Ins	200
NAA	NAA	50
Phosphorylethanolamine	PE	50
Serine	Ser	100
Taurine	Tau	200
Phosphocholine	PCh	27
Glycerophosphocholine	GPC	25

Table 5.1: Brain metabolites used to create a basis data set for LC –model, which will allow to evaluate the brain spectra quantitatively.

Spectra of the 16 most important brain metabolites (see Table 5.1) were acquired to create a basis data set at 17.6 tesla for LC – model [33]. All the spectra can be found in [122]. Furthermore a simulation of the spectra using NMRSIM (BRUKER) as an alternative to the acquisition of the data is presented.

5.1.4 Discussion

Although the CHESS water suppression module could be applied several times before the actual PRESS sequence, making the water suppression more effective, it was sufficient to conduct it just once in our case. Therefore, the possibility of additional signals arising from insufficient spoiled water was minimized. The water signal was reduced enough to resolve the metabolites within the dynamic range of the receiver. Shimming gave a line width of ≤ 3 Herz in the phantom. As the time for shimming was less than 10 minutes the use of the FASTMAP routine was a promising tool for in vivo applications. Since no signal

contamination from outside the voxel was observed the PRESS sequence should produces accurate localization in *in vivo* experiments.

As seen in the spectra the presence of eddy currents can not be neglected, particularly not with line widths in the single digit region. As the resonances in vivo have broader peaks the eddy currents might not be to obvious. Nevertheless all effort should be undertaken to keep the eddy currents as little as possible as otherwise a loss in SNR and distortions of the peaks and therefore the baseline of the spectra will occur. Eddy currents result mainly due to the fast switching of the gradients. They can occur especially in the NMR probe or the magnet itself. To minimize eddy currents the gradient switching shape is slightly modified from a strict trapezoidal to a shape with a more or less high overshoot at the end of each switching period that takes the unwanted eddy currents into account. In general the ramp time of the gradients should be as fast as possible (especially important for fast imaging sequences) without showing to much overshoot. It is not sufficient to observe the gradient switching shape of the gradient amplifiers, rather the acquired spectra in the magnet has to be observed after a gradient switching cycle to judge for the presence of eddy currents. By slight changes in the switching behavior of the gradients the effect of eddy currents should be reduced. The control for the gradient amplifier switching is called 'preemphasis' where LC-elements are provided to apply additional current into the gradient and the B0 shim coil. A manual adjustment of the preemphasis values is very time consuming and therefore not practical. Therefore in our case the preemphasis was adjusted as proposed by Terpstra et al. [123]. A semi automated correction method developed for Bruker imaging systems in Oxford (Dr Damian Taylor, Dr Juergen Schneider). After these adjustments, the removal of the residual eddy current effects using the phase of the additional acquired water signal led to undistorted spectra from metabolites at relevant in vivo concentrations.

5.2 **Rat and Mouse Brain in Vivo Spectroscopy**

5.2.1 Introduction

So far no *in vivo* spectra from the mouse or even the rat brain at 17.6 tesla are presented in the literature. Since susceptibility differences in the brain lead to much larger effects at 750 MHz than at lower frequencies, the feasibility of proton spectroscopy is shown in this chapter. A table of detected proton resonances in the rat brain by Pfeuffer et al [117] and their chemical shifts are shown in Table 5.2.

TABLE 1

^{1}H Chemical Shifts of Cerebral Metabolites, Detected in Rat Brain *in Vivo* Corresponding to Fig. 1

| | | | ^{1}H chemical shift | |
| | | | | |
No.	Compound	Carbon position	*in vivo* spectra (ppm)	Fitted model spectra (ppm)
1	*N*-Acetylaspartate	CH₃		2.009 (Ref.)	
2		αCH	C2		4.377
3		βCH₂	C3	2.489 + 2.674	
4		NH		7.82	
5	*N*-Acetylaspartylglutamate	CH₃		2.046	
6	γ-Aminobutyric acid	αCH₂	C2	2.28	
7		βCH₂	C3	1.89	
8		γCH₂	C4		3.01
9	Alanine	αCH	C2		3.777
10		βCH₃	C3	1.468	
11	Aspartate	αCH	C2		3.88
12		βCH₂	C3	2.79	2.66 + 2.79
13	Choline compounds	(CH₃)₃		3.209	
14	Creatine	CH₂		3.911	
15		CH₃		3.027	3.024
16	Phosphocreatine	CH₂		3.931	
17		CH₃		3.027	3.030
18	α-Glucose	[1]CH	C1	5.226	
19	Glutamine	αCH	C2		3.76
20		βCH₂	C3	2.12	
21		γCH₂	C4	2.45	
22	Glutamate	αCH	C2	3.75	
23		βCH₂	C3		2.08
24		γCH₂	C4	2.349	
25	Glutathione	Gly CH + Glu αCH	C2		3.77
26		Glu βCH₂	Glu C3		2.16
27		Glu γCH₂	Glu C4		2.54
28		Cys βCH₂	Cys C3		2.95
29	Glycerophosphorylcholine	NCH₃ + Glyc CH₂			3.66
30		OCH₂			4.31
31		Glyc OCH₂ + CH			3.90
32	*myo*-Inositol	[1,3]CH	C1,C3	3.525	
33		[2]CH	C2	4.060	
34		[4,6]CH	C4,C6	3.622	
35		[5]CH	C5	3.275	
36	*scyllo*-Inositol	CH		3.345	
37	Lactate	αCH	C2	4.11	
38		βCH₃	C3	1.318	
39	Phosphorylcholine	NCH₃			3.58
40		OCH₂			4.16
41	Phosphorylethanolamine	NCH₂			3.22
42		POCH₂		3.98	
43	Taurine	SCH₂		3.418	
44		NCH₂		3.246	

Note. ^{1}H chemical shifts were referenced to the *N*-acetylaspartate methyl peak. The assignment was based on LCModel analysis containing model solution spectra. Chemical shifts were determined from peak positions *in vivo* and from the fitted model spectra with an accuracy of ±1 Hz (±0.003 ppm).

Table 5.2: Brain metabolites and their chemical shifts. Taken from [117]

5.2.2 Material and Method

The MR-setup was the same as in the phantom experiment. The investigated animals were either small Fisher rats (≤ 200 g) or mice (~ 25 g), both from Charles River. The animal handling is described in chapter 3.3. After performing scout images to ensure accurate positioning of the animal, shimming with the FASTMAP tool was conducted. For the spectroscopic experiments the previous tested PRESS sequence, with CHESS water suppression was used. The voxel size was chosen to be 3 mm (5 mm in the rat) isotropic and the voxel was positioned below the corpus callosum. The acquisition parameters were: TR = 4 s,

TE = 15 ms, T_{exp} = 17 min, NS = 256 and the number of acquired points were TD = 2048 resulting in an acquisition time of 98 ms. Pulses with a sinc shaped pulse form were used for excitation. The 1 ms long spoiling gradients around the 180 – degree pulses were 40 mT/m. The frequency selective sinc shaped pulses for water suppression were 10 ms long (= 560 Hz) and the spoiler had a duration of 1 ms while being 40mT/m strong. Data analysis was performed using MestReC (MESTRELAB RESEARCH, Santiago de Compostela, SPAIN).

5.2.3 Results

Rat Brain

Figure 5.4 shows a representative spectrum acquired from a rat brain. The high SNR allowed the reconstruction of the data without exponential filtering, keeping the line width of the resonances as small as possible. Zero filling by a factor of 2 was applied prior to Fourier transformation. The performed water suppression was leading to a sufficient elimination of the water signal .Furthermore, no distortions due to the suppression below ~ 4.3 ppm in the spectrum were observed. The FASTMAP shimming routine ((5 mm)^3 voxel size) resulted in a water signal line width of only 27 Hz (data not shown) in the voxel of interest. Hence, no additional manual shimming was applied. The voxel was placed away from the edge of the brain, and therefore only a small lipid signal could be seen around 1.0 – 1.7 ppm. More than 20 resonances could be assigned to metabolites in the spectrum. The assigned numbers of the resonance peaks in Figure 5.4. correspond to the numbers in Table 5.2. The highest SNR is 279 for the creatine resonance at 3.027 ppm which has a line width of 34 Hz. Besides the obvious NAA CH$_3$ peak at 2.009 ppm the βCH$_2$ peaks could also be detected (#3 in the spectrum). It is noteworthy that the creatine and phosphocreatine methylene peaks at 3.922 and 3.941 ppm and the taurine and choline resonances at 3.249 and 3.216 ppm were resolved. Other peaks are the αCH$_2$ and βCH$_2$ resonances of GABA at 2.285 and 1.881 ppm, having a high SNR of around 70, and the resolved γCH$_2$ resonances of glutamate and glutamine at 2.338 and 2.435 ppm. Another glutamine peak, the βCH$_2$ resonance, could be

distinguished at 2.114 ppm. Only one peak arises from the αCH resonances of glutamine and glutamate at 3.76 ppm. Between 3.3 and 3.7 ppm large peaks from taurine (SCH2 at 3.416 ppm) and myo – inositol ([1,3]CH at 3.529 ppm and [4,6]CH at 3.617 ppm) were detected.
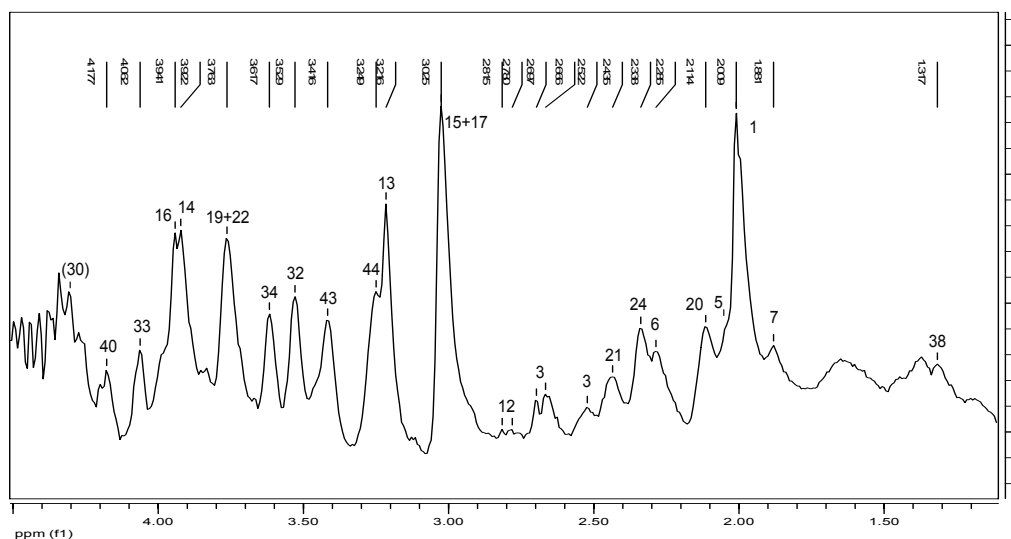
Figure 5.4: PRESS spectrum from a healthy rat brain. (voxel size = (5 mm)^3; NA = 256; TR = 4 s; TE = 15 ms). .

Mouse Brain

An example of a spectrum from a mouse brain is shown in Figure 5.5. The achieved line width of the water signal in the voxel of interest, using FASTMAP, was 30 Hz. Further shimming was not possible due to the limited power of the second order shim coils. As the brain is relatively small, contamination from lipids outside the brain is shown in this case (large resonance below 1.7 ppm). Again zero filling by a factor of two was applied. The SNR of the creatine resonance at 3.025 ppm was 26 and the line width was 57 Hz. The spectrum shows all the major resonances of the spectrum from the rat brain. Due to the lower SNR and the larger line width the creatine and phosphocreatine methylene peaks at 3.921 ppm and the taurine and choline resonances at 3.216 ppm were not resolved. While the αCH$_2$ GABA resonance at 2.277 ppm is still discernible the βCH$_2$ resonance could not be detected.
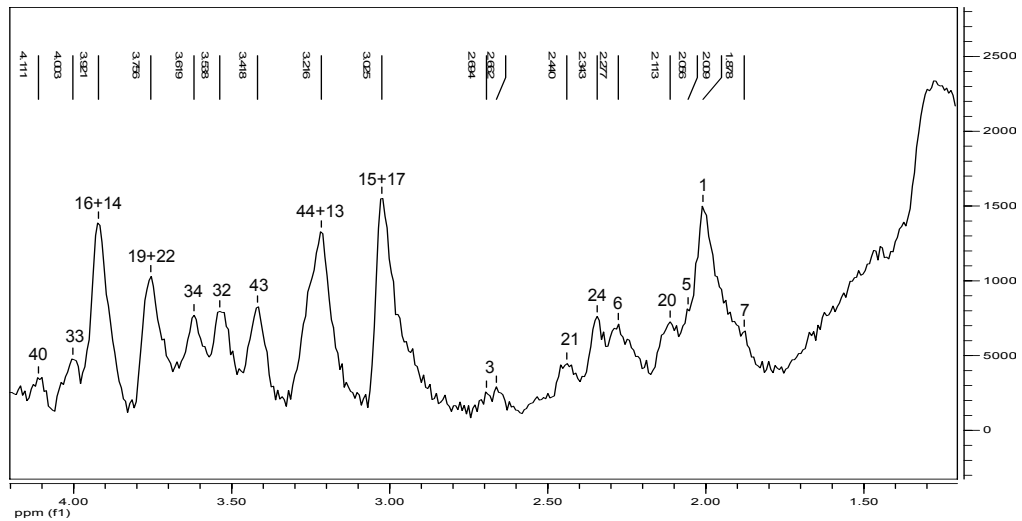
Figure 5.5: PRESS spectrum from a healthy mouse brain in vivo. (voxel size = (3 mm)^3; NA = 256: TR = 4 s: TE = 15 ms).

5.2.4 Discussion

In general, it is possible to acquire highly resolved in vivo single voxel proton spectra of the rat and mouse brain at 17.6 T. There are several reasons why the spectra from the rat have higher spectral quality than those from the mouse brain. First of all, as we were using the same setup for the rat and the mouse, the filling factor and therefore the sensitivity of the resonator was higher in the rat experiments. The main reason for the improved spectral quality is also size related: By using the maximal available second order shim coils smaller line width in the rat brain than in the mouse brain could be achieved due to the more homogenous tissue in the voxel of interest in the rat brain.

The spectra showed an improvement in spectral resolution for all metabolites compared to other studies at lower field strength [124], [125], [126]. Nevertheless there are also studies showing similar [127] or even better results [117], [119], [128]. Those studies were either conducted with larger voxel sizes [117], [127], larger number of averages [117], used optimized RF – resonators [117], [119], an improved shimming method [127] or even a newly designed shim system which provided improved second order shims [128].

Nevertheless, using high-field NMR with improved shimming possibilities may lead to a noninvasive assessment of a significantly expanded neurochemical profile *in vivo* for the study of animal models of disease.

5.3 T1 and T2 of major brain metabolites at very high fields

5.3.1 Introduction

As shown in the previous chapter, the spectral resolution of high field MRS allows the identification of more than 20 resonances in the spectrum of a rat/mouse brain. The concentrations of the metabolites in the brain vary. These changes can either be due to normal variations [128] or can be linked to diseases [49]. Spectroscopic imaging can be used to acquire spectra on a voxel basis [129] or even to generate metabolite maps of the different resonances [130]. To conduct an optimized MRSI experiment knowledge of the relaxation times T1 and T2 is necessary, especially when the concentrations of the investigated metabolites are very low as in *in vivo* experiments.

So far, relaxation times have predominantly been measured in rat models. However, to study the increasing number of genetically modified mouse models by using the benefits of the high magnetic fields, knowledge of T1 and T2 in the mouse brain is advantageous. Therefore, measurement of T1 and T2 in the mouse brain with system independent methods was performed at 500 and 750 MHz.

5.3.2 Material and Methods

MR Set-up

The T1 and T2 spectroscopy experiments were carried out in collaboration with Dr. Juergen Schneider from the Department of Cardiovascular Medicine, John Radcliffe Hospital (Oxford, UK). In Oxford an 11.7 T (500 MHz) MR system comprising a vertical magnet (bore size 123 mm – Magnex Scientific, Oxford, UK), a Bruker Avance console (Bruker Medical, Ettlingen, Germany), a shielded

gradient system (548 mT/m, rise time 160 μs - Magnex Scientific, Oxford, UK), and a quadrature driven birdcage coil with an inner diameter of 28 mm (Rapid Biomedical, Würzburg, Germany) was used to transmit/receive the NMR signals. Identical experiments were performed in Würzburg on the 17.6 T Avance system with the MINI 0.5 gradient system (chapter 3.1). In Würzburg an eight-leg, home-built birdcage resonator (inner diameter 38 mm) was used in linear mode (chapter 3.2.3).

<u>MR Methods</u>

Water-suppressed and unsuppressed spectra of $2 \times 3 \times 3$ mm^3 (18 μl) voxel size were acquired from the mouse brain using a PRESS sequence (TE = 13 ms, CHESS water suppression). For determination of T1, a non-selective inversion pulse (bandwidth: 4.5 ppm) was applied prior to the PRESS sequence, and prior to the water suppression module. Spectra were acquired at inversion times ranging from 10 ms to 10 s. T2 was measured using the sequence shown in Figure 5.6: A global CPMG sequence [80], [81] was followed by three slice-selective 180°- refocusing pulses. CHESS water suppression could additionally be applied prior to the CPMG module. The non-selective pulses used for the CPMG sequence were calibrated manually on the volume of interest. Between eight and 128/256 refocusing pulses were applied with an echo time pad of 3 ms, yielding total echo times between 59/83 ms and 803 ms. Using this approach rather than measuring T2 by a series of PRESS spectra with increasing echo time, reduces the effect of diffusion as the voxel selection module has the same timing for each time point on the T2 curve. Moreover a comparison on different scanners should be more accurate. The inversion pulses and the CPMG pulses were applied –2.5 ppm down-field relative to the water resonance to minimize off resonance effects.
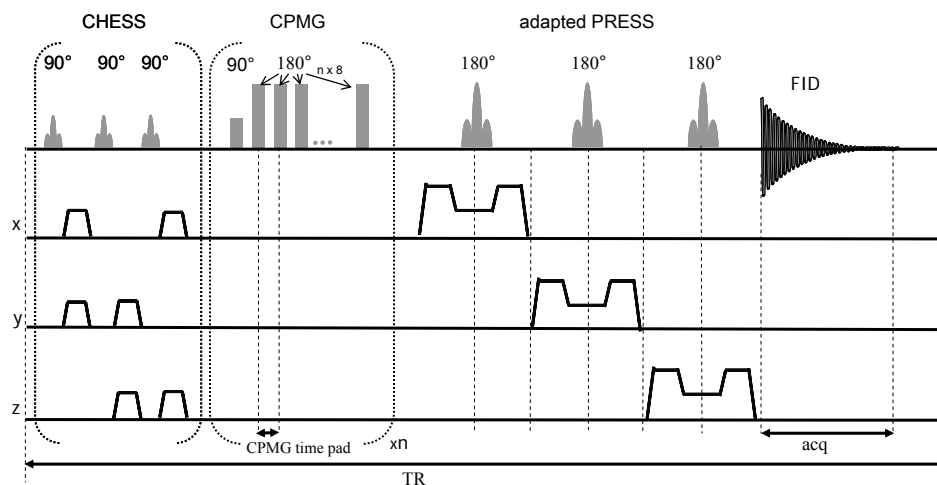
Figure 5.6: Pulse sequence to measure T2 .

Phantom Experiments

Before the *in vivo* experiments phantom experiments were conducted to validate the spectroscopic methods at 17.6 T on a 500 mM TSP-solution in a 10 mm NMR tube, doped with 10 μl Magnevist (Schering AG, Germany) per 5 ml solution. Specifically, unlocalized standard inversion recovery and CPMG sequences were compared to the respective localized methods ($3 \times 3 \times 3$ mm^3 voxel size), acquired with the same timing and with and without water suppression.

Solutions of 10 mM Cr, NAA and Cho were subsequently subjected to relaxation measurements at 11.7 T and 17.6 T. Each solution, containing 1 mM Gadodiamide (Omniscan, Amersham, UK), was filled into the 10 mm NMR-tube and surrounded by a physiological saline solution (in a 20 mm NMR tube). 16 points on the respective relaxation time curve were acquired with a repetition time of 5 s. 16 spectra were averaged for each time point. T1 - and T2 - measurements on water (+ 1 mM Omniscan) were also performed (no water suppression, NA=8). All samples were made from a stock solution and were identical for both centres. A series of 13 T2 experiments with time pads ranging from one to 12

ms was conducted on the water resonance to investigate possible diffusion effects. The temperature in these experiments was controlled by the water-cooled gradient systems, and was set to 20°C.

In vivo Experiments

Two groups of female C57Bl/6J mice (n = 5 each, 17 ± 2 g) were investigated in this study. After inducing anesthesia in an anesthetic chamber using 4 % isoflurane in 100 % oxygen, animals were positioned in dedicated animal holders, and maintained at 1.5-2 % isoflurane in 1.5 l/min oxygen flow. Cardiac and respiratory signals were continuously monitored throughout the entire MR experiment. Body temperature was maintained at 37°C. Mice were secured within the holder using surgical tape, without compressing their abdomen or chest regions.

After positioning the animals in the magnet, tuning and matching the coils, and acquiring scout images, a $3 \times 2 \times 3$ mm^3 voxel, placed underneath the hippocampus, comprising the striatum and parts of the brain chambers, was shimmed manually in Oxford, using the same PRESS sequence and with the FASTMAP tool in Würzburg. After manual adjustment of the pulses, a metabolite spectrum was acquired (TE/TR=13/10000 ms, NA=16). This was followed by the relaxation time measurements, whereby water suppressed spectra were averaged 32 times and experiments without water suppression 8 times, respectively. Eight points were acquired on each relaxation time curve. The overall experimental time was 2.5-3 hrs.

Data Analysis

All spectra were quantitatively analysed in the time domain using AMARES in jMRUI [131], [132]. The residual water resonance in the water-suppressed spectra was removed within ±0.5 ppm around the main water frequency using an SVD filter prior to fitting. Relaxation time curves were fitted in IDL using a least square fitting algorithm.

5.3.3 Results

<u>Phantom experiments</u>

In all phantom experiments at 17.6 tesla the FASTMAP shimming routine worked very well. Line widths of less than 3 Hz were achieved without any additional manual shimming. At 11.7 tesla line width of less than 7 Hz were achieved by manual shimming on the VOI. The results of the unlocalized and localized T1 and T2 measurements for the TSP solution at 17.6 tesla are shown in Table 5.3 No significant differences between the unlocalized and the localized experiments with or without water suppression were observed.

	TSP		H2O		water suppression
	T1/[ms]	T2/[ms]	T1/[ms]	T2/[ms]	
unlocalized	715±35	321	205±1	135	no
localized	707 ± 9	304±17	197±6	136±1	no
	682 ± 6	299±8	xxx		yes

Table 5.3: Validation of the T1/T2 sequences. Comparison of localized and unlocalized measurements.

As an example of the T1 results, spectra from the 10 mM NAA solution at 17.6 tesla are displayed on the left side of Figure 5.7. Only the main peak at 2.0 ppm was fitted. The right side of Figure 5.7 shows T2 spectra from the 10 mM creatine solution, again at 17.6 T. The CH_3 as well as the CH_2 resonance were fitted. A series of T2 measurements of the water resonance with different echo time pads during the CPMG sequence did not show changes in the T2 relaxation time (199 ± 2 ms).
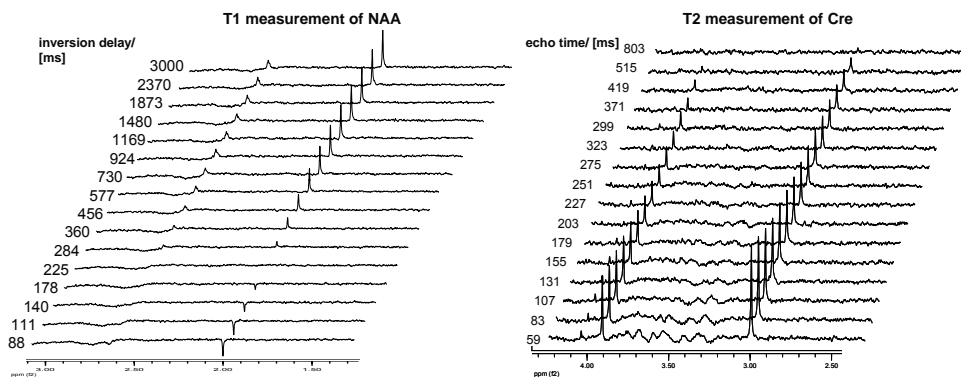
Figure 5.7: Examples of the T1/T2 phantom measurements. The left image shows the 16 spectra acquired at different inversion times for the evaluation of the T1 relaxation time of the 10 mM NAA solution. The T1 fit was conducted on the CH_3 resonance at 2.0 ppm. Because of the J – coupling the βCH_3 resonances (2.7 ppm) could not be fitted. Spectra from the T2 series for Cre are displayed in the right image. Both resonances at 3.0 and 3.9 ppm could be analyzed.

The results of the T1/T2 measurements at the two field strengths conducted on the 10mM metabolite solutions are shown in Table 5.4. While the T1 values are slightly higher at 17.6 than at 11.7 tesla, the T2 values are the same for both field strengths.

	T1		T2	
	11.7 T	17.6 T	11.7 T	17.6 T
H2O	250 ±5	262 ± 6	196 ± 7	197 ± 9
Creatine – CH3	325 ±13	386 ±14	228 ± 9	231 ± 12
Creatine – CH2	304 ±19	305 ±23	222 ± 19	195 ± 15
NAA	282 ±14	348 ± 25	178 ± 11	208 ± 15
Choline	406 ±8	481 ± 5	287 ± 22	333 ±17

Table 5.4: Results of the T1/T2 phantom measurements at 11.7 and 17.6 tesla.

T1 measurements of the mouse brain metabolites *in vivo*

Voxel-based shimming led to a line width of less than 50 Hz for the unsuppressed water line in all experiments. Example spectra for each time point on the T_1 metabolite curve are shown in Figure 5.8. The measured T_1 values for the water and metabolite resonances *in vivo* are shown in the insert. Although the differences between the T_1 values of Cre and Cho at the two field-strengths are not statistically significant at the $p < 0.01$ level, due to the small sample size, the values at 17.6 tesla and those at 11.7 tesla are both higher than those reported previously at 9.4 Tesla [117] in the rat brain. Furthermore they are in accordance (within the error bars) with the work from de Graaf et al [119] who recently investigated T1 and T2 of water and metabolites in the rat brain, using field strengths from 4.0 up to 11.7 tesla.

	T1 11.7 T	SD	T1 17.6 T	SD
Cre	1.508	0.251	1.577	0.351
Cho	1.553	0.210	1.641	0.149
NAA	1.529	0.353	xxx	xxx
H2O	1.468	0.248	1.826	0.176
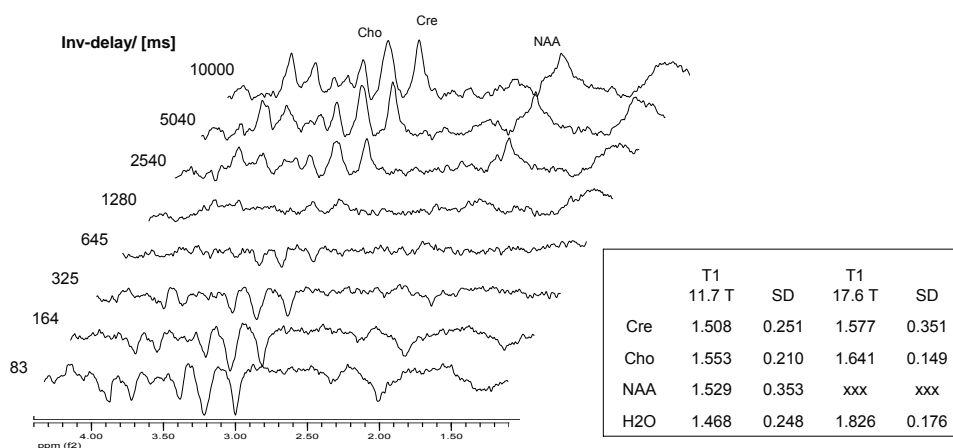
Figure 5.8: Spectra from an inversion recovery experiment of an 18 µl voxel placed in a mouse brain. Shown data was acquired at 750 Mhz. Table shows the acquired T1 values in seconds at 11.7 and 17.6 tesla.

The broad signal present at around 2 ppm, probably originating from macromolecules, produced a large baseline signal. This distortion and the relatively low total peak height led to an unreliable T1 value of NAA at 17.6 tesla. The reason why the NAA peak acquired at 17.6 tesla was more influenced than the one at 11.7 tesla might have been the chemical shift displacement: The original

voxel was placed in the RARE images to fit inside the mouse brain. By taking the gradient strength and the chemical shifts of the metabolites into account the NAA resonance had only 30% volume with the original voxel in common. The maximum shift in one direction was 1.1 mm. The voxels for Cho/Cre had an overlap of 54% / 49% with the original voxel. Their maximum shift in one direction was 0.6 / 0.7 mm. The overlap of the NAA and Cho voxel was only 55%. Therefore, if the voxel of the Cho resonance happened to be at the edge of the brain, but still inside, the NAA voxel would generate a much weaker signal due to the fact that up to half of the voxel is placed outside the brain. Although the gradient strengths used at 11.7 tesla were about the same as at 17.6 tesla, the lower resonance frequency reduced the chemical shift displacement. The overlaps with the original voxel were 68 % for choline, 64 % for creatine, and 48% for NAA, resulting in reliable numbers for the T1 fits of all three metabolites.

T2 measurements of the mouse brain metabolites *in vivo*

Example spectra of a T2 measurement at 17.6 tesla are shown in Figure 5.9. Although decays with increasing echo time could be observed, the standard deviations of the fitted T2 values were too high to present a reliable value for both field strengths. Reasons for this are manifold and will be discussed in the next section.
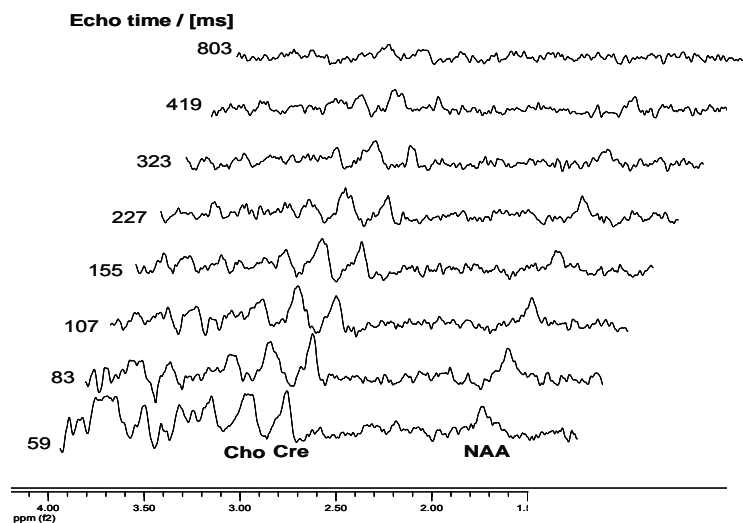

Figure 5.9: Spectra from a T2 measurement of a 3 x 2 x 3 mm^3 voxel in the mouse brain *in vivo.*

5.3.4 Discussion

While the FASTMAP routine, used at 17.6 tesla, yielded line width of less than 3 Hz of the water and the metabolite resonances in the phantom experiments, the *in vivo* results were not as satisfying (FWHM: 30 -50 Hz). The problem was not the FASTMAP sequence itself, but rather the limited strength of the second order shims. Therefore, the calculated necessary shim currents could not be applied and the minimum line width for the water resonance by using FASTMAP was high. Recently Tkac et al [128] showed at 9.4 tesla that line widths between 11 – 14 Hz of the unsuppressed water signal could be achieved in 5 – 10 μl voxel sizes in the mouse brain. They were using a FASTMAP sequence and a very strong custom – designed second order shim coil. Another study by de Graaf et al conducted on the rat brain reached line widths of the water resonance of only 8 Hz at 4 tesla, and 16 Hz at 11.7 tesla. As their shim volume of $(4 \text{ mm})^3$ was slightly smaller than the one we used in the rat brain $((5\text{mm})^3)$, our achieved line width of 27 Hz is of comparable quality. The conducted FASTMAP experiments in Oxford showed that their second order shim ability was very limited. Therefore manual shimming on a voxel basis had to be applied as the FASTMAP sequence did not provide any reasonable result.

To keep the total experimental time as short as possible, but also to measure T1 and T2 during one session, the number of repetitions for one spectrum was limited to only 32, resulting in a very low SNR (~ 10) of the metabolite resonances. An increased voxel size would provide a higher SNR on the one hand, but would also increase the chemical shift displacement (Equation 2.39). A smaller voxel, concordant with increased gradient strengths, would decrease the chemical shift displacement but the SNR would be lowered. Furthermore the line width of a voxel with a reduced volume should be smaller due to the decreased inhomogeneities within the voxel. Another parameter that had to be taken into account is the total available power of the transmitter necessary to achieve 180 degree shaped pulses. The time of those pulses had to be as short

as possible to invert the spectral range of interest, and especially in the PRESS module to achieve reasonable echo times.

As the SNR of the metabolites was limited, a fitting in the frequency domain, rather than in the time domain, or a combination of both may yield further improvements in the T1/T2 fitting. The use of prior knowledge, like model spectra, either measured or simulated (prepared for LC –model [122]) would also improve the fitting. A detailed overview of common fitting routines in MRS is given in [133].

The achieved T1 values in the mouse brain are in accordance with the literature from T1 values acquired at lower field strength (e.g. [117][119]) in the rat brain. However the calculated errors of the T1 values in our study are extremely high. To reduce those errors a higher SNR, by conducting more averages, should be achieved and a different fitting method (see above) should be applied. Nevertheless the presented values are the first once acquired at 11.7 and 17.6 tesla in the mouse brain.

Although published T2 values have been measured by other researchers with a spin echo method with variable echo times the effect of diffusion were often neglected (e.g. [117][119]) and inconsistent values were presented (see Table 2.7 in [5]). As diffusion leads to more signal loss for longer echo times the measured "apparent transverse relaxation time" is shorter than the intrinsic transverse relaxation time. In our T2 measuring method the diffusion effects are approximately the same for every time point on the T2 curve. Especially the T2 measurement series of the water resonance with different echo time pads showed that there are no or only minor diffusion effects. T2 had a constant value, although a large range of echo time pads was investigated. Therefore, the influence of diffusion due to different gradient settings as in a variable echo time T2 measurement method, were minimized. This result showed that the T2 sequence should be independent of the MR system and comparable results measured at different systems should be achievable.

In conclusion, our work shows the feasibility of measuring metabolic longitudinal and transverse relaxation constants at ultra high fields in the mouse brain. T1 could be determined *in vivo* within physiologically viable experimental times, despite increased methodological challenges inherent to ultra-high magnetic fields. Due to the limited number of animals, the small number of transitients, and the long echo time for the first measurement, T2 in mouse brains *in vivo* could not be determined in a significant way. Future experiments with a higher number of averages, even smaller voxel sizes, and a shorter first echo time should yield system independent T2 values of the major metabolites in the mouse brain *in vivo* at very high field strengths. In general the use of very strong second order shim coils would improve the line width and therefore the spectral quality tremendously. Replacing the volume RF- resonator with dedicated surface coils should also improve the SNR and hence the fitting results.

6 Iron Labeled Stem Cell Imaging

<u>Introduction</u>

The potential of stem or progenitor cells to regenerate damaged tissue in neuronal diseases has attracted much attention in neurological research over recent years. Stem cell transplantation is a promising therapeutic approach for Parkinson´s Disease [134] - [136], cerebral ischemia and chronic neuroinflammation [137] - [141]. However, clinical studies concerning long term survival, differentiation and migration of grafted cells in the host organism have been not very effective [142], [143], because no reliable non-invasive method exists for monitoring transplanted cells *in vivo* at high spatial resolution over an extended period of time. Positron emission tomography (PET) [144] allows non-invasive detection with very high sensitivity but suffers from poor spatial resolution. Magnetic resonance imaging (MRI) can provide images with very high spatial resolution in small animals, but requires efficient labeling of the cells for these to be observed. Several strategies to make cells MR-visible have been developed. Most efforts incorporate small iron-oxide particles into cells which leads to a strong decrease in the transverse relaxation time of water protons diffusing close to the cells, resulting in turn in signal loss in T_2^*-weighted gradient echo images [145] - [148]. Strategies to optimize particle incorporation and contrast behaviour have been developed by using different lipofection agents [149], translocation peptides [150], or by use of phagocytosis only [151]. Initial studies on the visualization of grafted magnetically labeled cells have been conducted both *in vitro* [152] and *ex vivo* [153], [154]. These studies showed that neuro-transplantation of magnetically labeled oligodendrocyte progenitors is feasible and that MRI can visualize cell migration and myelination [154]. *In vivo* visualization of labeled cells after transplantation has been shown in other studies in the rat brain [153], [155] - [157] as well as in the swine heart [158],[159]. Recently, it was shown in a rat model of ischemia that, after injection of magnetically labeled embryonic stem cells into the non-ischemic side of the brain, stem cells migrated along the corpus callosum, populating the border zone of the ischemic area of the contralateral hemisphere [160]. A similar migration behavior was observed after implantation of magnetically labeled bone marrow stro-

mal cells in a rat model with a cortical lesion [161]. The migration velocity of grafted subventricular zone cells, labeled with iron-oxide particles, has been measured in a rat stroke model [162]. However, in all these studies large numbers of cells ($10^5 - 10^6$) have been grafted and observed.

To obtain a detailed insight into migration processes or to observe cells after intravascular administration it would be advantageous to detect many fewer cells (< 1000). The feasibility of observing single cells with MR methods *in vitro* has been demonstrated very recently [148], [163]. For *in vivo* investigations, however, only rough estimates of the minimum number of detectable cells are available to date.

The purpose of our study was to explore the limits of MRI-detection of grafted cells in the rat brain *in vivo.*

Material and Methods

Details about cell culture of the mouse embryonic stem cells (CRL-1934, ATCC, Manassas, USA), labelling with very small superparamagnetic iron-oxide particles (VSOP) C200 (Ferropharm, Teltow, Germany), the accuracy of the number of cells that were implanted and stereotactic transplantation can be found in [164].

Before animal experiments were performed agarose gel phantoms were prepared and imaged to prove the feasibility of the study. Four injections of 2 µl of a cell suspension with different but defined number of cells were placed in each phantom. Special care was taken to reduce air bubbles in the gel phantom.

Gels were imaged with a highly T2* weighted 3D FLASH gradient echo sequence with 98 µm isotropic spatial resolution (TE/TR = 5/20 ms; matrix: 256^3; flip angle: between 5° and 10°).

Female Wistar rats (130-150 g) (Charles River WIGA, Sulzfeld, Germany) were anesthetized with isoflurane (Abbott, Wiesbaden, Germany) and each animal received an injection of 2 µl (1µl / 2 min) cell suspension into the striatum of the left brain hemisphere via a Hamilton microsyringe. Six animals received 1000 unlabeled cells, as control animals, and eleven animals received labeled cells (one animal 120000, three animals 1000, three animals 100, and four animals 20).

Due to the size of the animals the 38 mm proton resonator and the MINI 0.5 gradient system were used for the in vivo experiments and a birdcage with an inner diameter of 15 mm (BRUKER) was used for the phantom experiments.

All animals were kept under anesthesia after the transplantation and 3D gradient echo imaging experiments were performed. The behavior of the transplanted stem cells was monitored up to six weeks after the operation in some of the animals. After positioning, a 3D data set with an isotropic resolution of 98 µm was acquired with a $(256)^3$ matrix over a field of view of $(2.5 \text{ cm})^3$ comprising the whole brain; TE/TR = 3.0/20 ms; scan time 22 minutes. After identification of the transplantation site a second high resolution 3D data set with 98 µm isotropic resolution but 256 x 256 x 128 points was recorded over a smaller field of view: TE/TR = 4.6/15 ms; scan time 32 minutes (4 averages). The SNR in the images was between 20 and 30 in grey matter regions of the brain. For the animal that had received 120,000 cells a modified protocol with lower spatial resolution (117 x 117 x 183 μm^3, TE/TR = 2.7/30 ms) was sufficient to observe the cells.

Image processing was performed with the software packages Paravision (Bruker, Rheinstetten, Germany) and Amira (TGS, San Diego, USA).

After the final imaging sessions, rats were euthanized with an overdose of pentobarbital and either perfused for paraffin embedding or prepared for frozen sectioning. The obtained histological slices were stained for iron and immunohistochemistry was performed in cases where transplanted cells were observed.

Results

Cell handling

Efficient incorporation of VSOPs by the stem cells was shown by confocal laser scanning microscopy (CLSM) and fluorescent iron-oxide particles. The left image of Figure 6.1 shows the fluorescence of the Rhodamine green labeled iron-oxide particles, generally proving the presence of VSOP in a single cell. The right image is an overlay of the left image and the image achieved from the membrane marker ANEPPS (see [164]), which stains the cell membranes red. The VSOP aggregates surrounded by membranes form endocytotic vesicles. As all of the visible fluorescent labeled VSOPs are surrounded by membranes

they must have been incorporated into the cell. The large dark spot in the images presents the nucleus of the cell.
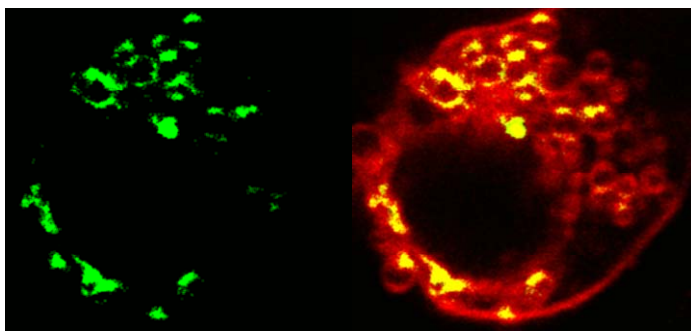

Figure 6.1: Fluorescence microscopy of one cell with VSOPs colabeled with fluorescence marker (rhodamine green, left). A control channel on the right, shows fluorescence of the membrane marker ANNEPS.

The highest standard deviation for the stem cell count prior to the operation was 30 – 40 % in the case of only 10 cells / µl, the smallest number of cells implanted into the brain. All other numbers of cells were counted with a standard deviation of less than 15 %. No significant difference was found between the number obtained with the Neubauer chamber and the count with fluorescence microscopy.

In vitro MR visualization of cells

To assess the potential of the applied MR methods in conjunction with our labeling strategy and the transplantation protocol, we injected 2 µl of different concentrations of VSOP labeled cells into agarose gels according to the *in vivo* transplantation protocol. In T_2^*-weighted MR images the gel appeared homogeneous, indicating that the gel was virtually free from air bubbles. The injection canals were identified by slightly higher signal intensity compared to the gel. Figure 6.2 shows longitudinal sections through two or three (out of four) injection canals in the gels for injection of unlabeled (500 cells/µl) and labeled cells (500 and 50 cells/µl). Labeled cells were detected as areas corresponding to signal reduction in the image along the injection canal. Whereas with 500 cells/µl large areas of signal loss were observed along the entire canal (Figure 6.2 middle), with 50 cells/µl dark areas were separated and signal reduction

114

was less pronounced (Figure 6.2 right). The injection of 1000 unlabeled cells showed no large areas of signal loss in the injection canal (Figure 6.2 left)
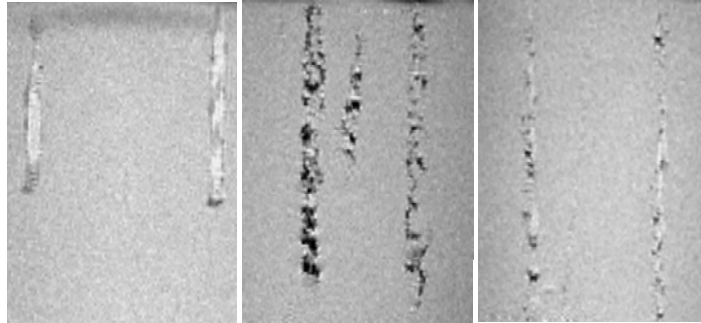

Figure 6.2: Gradient echo images of gel phantoms after injection of 1000 unlabeled (left), 1000 labeled (middle), and 100 labeled cells.

In vivo MRI of labeled cells

In order to explore the minimum number of cells that can be identified by MRI *in vivo* we transplanted different numbers of labeled and unlabeled stem cells into the striatum of 17 female Wistar rats. The intrinsic image contrast allowed distinction between grey and white matter structures such as corpus callosum, fornix, and anterior commissure. Parts of the ventricles and vessels could also be identified. In the latter, signal intensity depended strongly on the orientation of blood flow. Transplantation of 120,000 labeled cells was easily identified via large regions of very low intensity (Figure 6.3 left). Directly after transplantation (~ 1 h) the cells were distributed throughout a wide area inside the left hemisphere (Figure 6.3 right). Besides the transplantation canal, cells were distributed over the left ventricle. No cells were observed in the right hemisphere. Three days after transplantation only minor changes in the cell distribution were observed. The signal loss along the canal was slightly less pronounced while the distribution in the ventricle was slightly more widespread. In addition to the left ventricle, cells were also observed in the left part of the third ventricle. Over a period of the next 22 days no significant changes in the location of the cells were found.
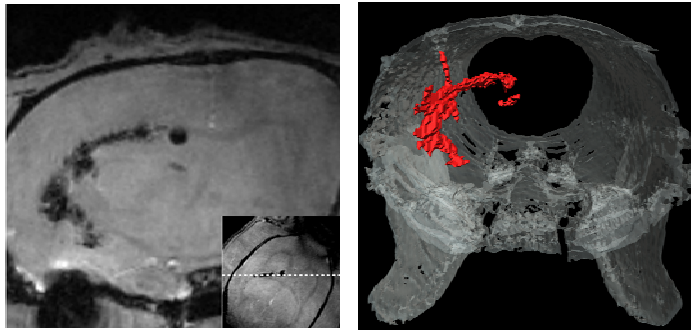
Figure 6.3: Transplantation of 120 000 cells. left: 2D section through a 3D gradient echo data set. Cells are clearly seen as area of low signal.right: 3D volume reconstruction of the distribution of transplanted cells. The ventricle and also the needle track are filled.

After transplantation of 1000 labeled cells in the striatum of three rats a clearly visible area, extending to the deep end of the transplantation canal, of signal loss was observed in each animal (Figure 6.4 middle). In contrast, none of the six animals that had 1000 unlabeled cells transplanted into them showed a comparable signal loss at the transplantation site (Figure 6.4 left). Nevertheless, in two animals significant signal losses in the upper part of the needle track were observed, which may have resulted from infiltration of cerebrospinal fluid (CSF) or blood (data not shown). Transplantation of 100 cells resulted in an area of signal extinction which was easily visible in several slices of the 3D data set (Figure 6.4 right), but the area of signal loss became smaller. A distribution along the lower half of the canal that may have resulted from retraction of the needle was also visible. In Figure 6.4 several smaller areas of signal loss are seen in the deeper part of the brain. These may result from clusters of up to 10 cells. Infiltration of CSF or micro-bleeding that can cause similar signal extinction would be observed as larger, contiguous areas. After transplantation of approximately 20 cells only small areas of reduced signal were observed, extending only over two or three slices in the data sets (data not shown). However, the small dimension and the incomplete loss of the signal did not allow to attribute these observations unambiguously to the labeled cells. Here, infiltration of CSF or blood may have been the cause of the signal loss.
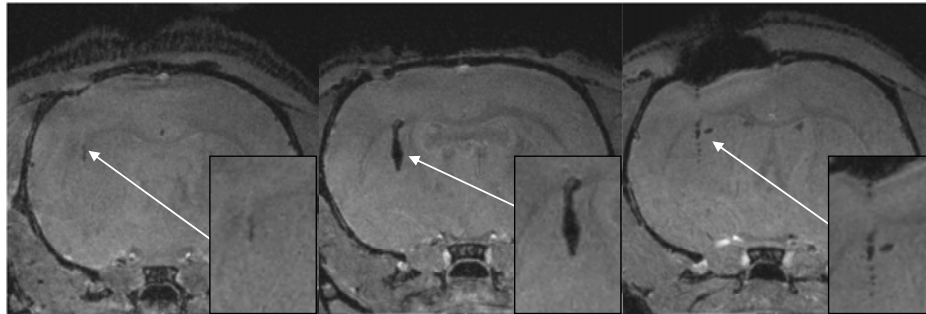
Figure 6.4: Gradient echo images of three rat brains with different numbers of cells. In the left image 1000 unlabeled stem cells were transplanted (control). The middle and right images show rat brains after transplantation of 1000 and 100 labeled stem cells, respectively (from [164]).

Histology

Histologically, the needle tract was found in all perfused animals after careful scrutiny of serial sections in both horizontal and frontal brain cuts. The few sections containing the tract showed a small cortical glial scar, sometimes with a tiny central defect (Figure 6.5 A). In Prussian-Blue stained sections a few iron positive cells were present in centrally located or perivascular cells (Figure 6.5 B). In some animals, both within and in the vicinity of the needle tract, small microbleedings were seen.
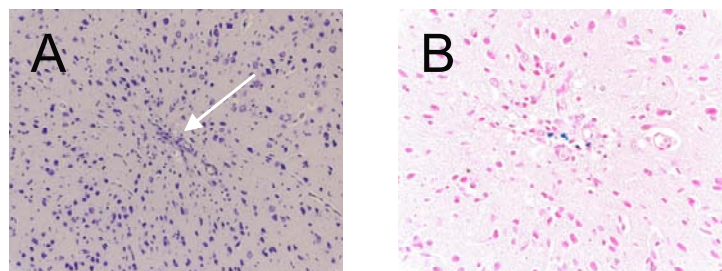
Figure 6.5: Histology of a rat after transplantation of 1000 VSOP-labeled stem cells.(A) Nissl stain. Within the tissue a small cortical glial scar with a tiny central defect (arrow) can be seen. (B).In Prussian-Blue stained sections a few iron positive cells were present in centrally located or perivascular cells. (from [164])

In one long-term survival animal injected with 1000 non-labeled cells, a conspicuous cellular conglomerate of approximately 1 mm diameter was present at

the end of the needle tract in the subcortical white matter, suggestive of neoplasia. At higher magnification, this circumscribed lesion contained a polymorphous population of cells. There was regional heterogeneity with either small undifferentiated and densely packed cells, or larger cells of epithelial appearance with nuclear hyperchromasia and mitoses. Perivascular rosettes and also true rosettes of the Flexner type were seen in several places. These cells were positive for GFAP and showed a high proliferation index using the MIB antibody (not shown).

Discussion

In this study we have shown that VSOPs are incorporated by mouse embryonic stem cells in sufficient amounts to act as an efficient cellular label. Our MRI results show that a single incubation step with VSOP is sufficient for *in vivo* detection of labeled stem cells. Several different labeling strategies have already been established, which make use of, for example, lipofection [149] or translocation peptides [150]. The question, however, of whether such procedures result in an increased sensitivity of the MR experiments, or whether they in fact harm the cells have not yet been answered. For example, a recent study showed that magnetic labeling leads to an increase of cellular oxidative stress. However, the increase seemed to be transient and no long term effects regarding cellular proliferation and viability were found [165]. Further systematic studies addressing possible effects of the labeling procedure on differentiation and migration of the cells are clearly required.

The first prerequisite for the determination of the minimum detectable cell number is a reliable method for controlling the number of cells. Comparison with fluorescence microscopy demonstrated that our procedure is accurate, keeping in mind the high dilution of the cells. Even in the case of the highest dilution of

only 10 cells/µl the deviation is within an acceptable range. The results of the counting procedure suggest that the concentration is slightly overestimated, due to a loss of cells in the inevitable last centrifugation step.

In vitro MRI experiments showed that cells labeled with VSOP can be visualized in T_2^*-weighted images after injection into agarose gels. We estimate that *in vitro* less than 10 cells is sufficient to be observed. The possibility of visualizing single labeled cells with gradient echo imaging methods at very high magnetic fields has recently been shown for cells labeled with larger iron particles [148].

Our *in vivo* data clearly show that 1000 grafted cells are observed at the transplantation site as a large area of low signal. No corresponding signal attenuation is found with unlabeled cells. In two control animals a high degree of signal loss was observed only in the upper canal in a contiguous area to the surface of the skull. Apart from these two animals only very small signal alterations were observed in the control animals. Areas of signal void were smaller in the animals that had received 100 labeled cells compared to animals that had received 1000 labeled cells, but were still more pronounced than the small signal alterations found in the controls. In two animals that received 10 cells / µl a small region of reduced signal in the injection canal was clearly identified. However, it can not be excluded that this signal reduction is caused by infiltration of CSF or blood. Histological findings, showing iron-containing stem cells in the direct vicinity of the needle track in animals that had received 1000 cells, confirmed the MR results. In animals with only 20 grafted cells it was not possible to locate reliably the cells in the tissue sections. Together with observation of cortical glial scars and microbleedings this supports the possibility that signal reduction with 20 cells may be due to other sources of contrast.

We have performed our investigation at the highest magnetic field available for imaging of rodents, 17.6 T. Higher magnetic fields have two major benefits: first, a higher equilibrium magnetization gives a higher intrinsic image SNR. Second, differences in the magnetic susceptibility, introduced by the iron particles in the grafted cells, lead to much more pronounced signal reductions than at lower field strengths. Thus, at 17.6 T comparable contrast is observed with far fewer cells than at lower fields. If the goal is to observe the bulk motion of several thousands of cells, low magnetic field strengths are sufficient. But, if the focus is on the microscopic migration and distribution of small numbers of cells, such as studying stem cell recruitment after stroke [138], high magnetic fields are necessary.

One potential method to increase further the sensitivity to T_2^*-effects is the use of steady-state-free-precession (SSFP) sequences. These have recently been shown to enable detection of single iron-labeled cells, embedded in a gel, at 1.5 T [163]. However, SSFP sequences are extremely prone to image artifacts in inhomogeneous media or if the object is moving. The sensitivity towards artifacts increases with the strength of the magnetic field. Only recently have SSFP sequences produced images of fixed samples at 11.75 T superior in contrast-to-noise to conventional gradient echo methods [166]. High field applications on living animals remain extremely problematic and have, to the best of our knowledge, not been reported to date.

Summarizing our results, approximately 100 cells are clearly observable by high resolution MRI, and can be distinguished from other sources of signal reduction. Numbers as low as 20 cells and below are potentially detectable in animals *in vivo* under optimized experimental conditions. The dominant problem at these

low cell numbers is the distinction of cells and other sources of contrast (mainly microhemorrhages induced through the implantation). However, in the monitoring of stem cells in different animal models the problem of induced microhemorrhages will be of less relevance, since cells are often not grafted directly at the lesion site. Time course studies of animals will also facilitate the distinction between hemorrhages and cells migrating towards the lesion sites.

7 Conclusion

The goal of the work presented in this thesis was to explore the possibilities and limitations of MRI / MRS using an ultra high field of 17.6 tesla. A broad range of specific applications and MR methods, from MRI to MRSI and MRS were investigated. The main foci were on sodium magnetic resonance spectroscopic imaging of rodents, magnetic resonance spectroscopy of the mouse brain, and the detection of small amounts of iron labeled stem cells in the rat brain using MRI

Sodium spectroscopic imaging was explored since it benefits tremendously from the high magnetic field. Due to the intrinsically low signal in vivo, originating from the low concentrations and short transverse relaxation times, only limited results have been achieved by other researchers until now. Results in the literature include studies conducted on large animals such as dogs to animals as small as rats. No studies performed on mice have been reported, despite the fact that the mouse is the most important laboratory animal due to the ready availability of transgenic strains. Hence, this study concentrated on sodium MRSI of small rodents, mostly mice, and in the case of the brain on young rats.

In order to acquire in vivo sodium images of the rat and the first ones of the mouse dedicated RF birdcage resonators driven in quadrature mode, for 17.6 tesla, were built during this work (Chapter 3). Since the low concentrations in vivo and the short relaxation times of sodium require a measuring method that allows reduced acquisitions per data set and provide a very short echo time, a phase encoding density weighted CSI method was designed. The sequence was implemented on the Avance 750 and extensions to measure T1 on the basis of inversion recovery and saturation recovery, and to measure T2 on a spin echo basis with variable echo times were developed. Details can be found in Chapter 4.1. After evaluating the new methods in phantom experiments (Chapter 4.2), in vivo experiments were conducted as described in the following chapters.

Chapter 4.3 discusses the results achieved from the in vivo rat and mouse brain. Both healthy as well as animals with stroke were investigated. The sodium DWCSI data set with a resolution of 5 μL of the healthy rat brain shows

much more detailed information compared to recent studies found in the literature. Time and spatial resolution are important in studies of stroke in chapter 4.3.2, and the superiority of the setup in this study is shown. Compared to studies in the literature, the examples shown in this work have a modest time reduction of 10% but an enormous (19 fold) decrease in voxel size. Therefore, changes in the sodium distribution during stroke should be subject of future studies especially as spatial resolution could be sacrificed to benefit the temporal resolution if necessary. The example with the unintended development of a brain cyst stands out not only because of the high spatial resolution of (0.8 mm)^3 but also because its demonstration of the fact that cysts detection is possible with sodium MRI.

Chapter 4.3.3 shows the first ever conducted sodium MRI studies on the mouse brain. Although having a more coarse resolution than the RARE and diffusion weighted proton images the sodium images delineate the stroke precisely. The measured T1 relaxation times showed highly elevated values in the stroke regions (56 ms) compared to the healthy brain (42 ms) which is in accordance with values published on rat brains.

Results from a more challenging (heart rate approx. 600 beats/min, 'hick up breathing', small size ~1 cm^3) application, namely mouse heart, are shown in chapter 4.3.3. These first sodium mouse heart images show clear demarcation of the left and the right ventricle and parts of the myocardium. One animal with an infarct was imaged three weeks after operation. Due to the wall thinning and the reduction of the sodium signal in the scar after a few weeks post infarction an increase of the sodium signal in the thin wall could not be unambiguously observed. This study should be the cornerstone of sodium mouse heart imaging and future promising studies should follow to provide information, for example, about the progress of infarction.

The last organs studied in this chapter are the kidneys of the mouse. Renal imaging of the mouse kidney, before impracticable due to insufficient SNR, showed its feasibility and provided detailed information concerning kidney homeostasis. High resolution sodium images of the mouse kidney were achieved and the corticomedullar sodium gradient was observed despite the small size and the low sodium concentrations. In the functional study of induced diuresis, three dimensional data sets of the kidney with a reasonable resolution were ac-

quired in less than five minutes. This enabled the time course of diuresis induced via Furosemide to be studied. The findings (Chapter 4.5) are in good agreement with the studies conducted by Maril et al on kidneys of much larger rats. To complete the characterization of the sodium imaging of the mouse kidney, T1 and T2 of the different kidney regions were determined and analyzed. These results suggest that meaningful sodium experiments can be performed on transgenic mouse models of disease, complementing the recent advances in sodium imaging of human patients.

Overall this work proved the feasibility of mice sodium MRSI in different parts of the body and showed resolution enhanced sodium images of the rat brain. Therefore these results should be encouraging for a whole variety of new studies in the future.

The gain of SNR due to the high static magnetic field was either used to increase the spatial resolution (in all cases) and/or to increase the temporal resolution especially in the case of the induced diuresis.

The second part of this work concentrated on proton magnetic resonance spectroscopy of the rodent brain. Due to the high magnetic field strength not only the increasing signal but also the extended spectral resolution was advantageous for such kind of studies. The difficulties/limitations of ultra high field MRS were also investigated.

In chapter 5.1 phantom experiments showed the ability to suppress water, shim, localize, and reconstruct eddy current corrected spectra. A data base for future quantitative studies using the LC-model, a frequency domain fitting software, was created. The achieved line widths in those spectra were less than 3 Hz. In the GABA phantom the J-coupling constant of 7 Hz could be determined.

The spectra of the rat/mouse brain in chapter 5.2 were the first ones acquired at 17.6 tesla. Due to the limited strength of the shim coils, relatively large line widths of the water resonance of a minimum of 27 Hz in the rat and 50 Hz in the mouse brain were observed. This effect counteracts the increased spectral resolution and requires further attention in upcoming studies. Nevertheless, the achieved spectra showed all the metabolites detected by other researchers at lower field strengths. A comparison of T1 of the major brain metabolites in the mouse brain at different field strength conducted in Oxford at 11.7 and in

Conclusion

Wuerzburg at 17.6 tesla resulted in comparable (within the error values) to very recently published results in the rat brain by de Graaf et al. It should also be noted that the voxel size in our experiments was more than four times lower compared to de Graaf et al. While the newly developed sequence to measure T2 independently of the system, in particular the gradient system of the NMR machine, showed promising results in the phantom studies (chapter 5.3.3) where T2 was the same at 17.6 tesla and at 11.7 tesla, the studies in the mouse brain suffered from a low SNR. Nevertheless this gradient independent approach should be used to determine T2 in the rat/mouse brain at different field strengths. In conclusion, we have shown that it is possible to acquire highly resolved spectra from the rat and the mouse brain at 17.6 tesla. Despite the difficulties of the high field the spectra are of good quality and an enhancement in terms of SNR and spectral resolution is obvious.

In the last part of the presented work detection limits of iron labeled stem cells in vivo using magnetic resonance imaging were explored. After establishing a method to label stem cells with VSOPs, ensuring the accuracy of counting the cells, and phantom experiments, different numbers of cells (120,000, 1000, 100, and 20) were injected into the rat brain in vivo and MRI was conducted. While 120,000, 1000 and 100 cells were observed unambiguously, other sources of hypo intense signal areas in the brain such as microhemorrhages induced by the needle of the syringe during injection or blood vessels made it difficult to depict 20 cells without doubt. Nevertheless, these studies provided very useful benchmarks for future researchers in terms of the number of labeled stem cells that are required for high-field MRI studies.

Overall this work has shown many of the benefits and the areas that need special attention of ultra high fields in MR. Three topics in MRI, MRS and MRSI were presented in detail. Although there are significant additional difficulties that have to be overcome compared to lower frequencies, none of the work presented here would have been possible at lower field strengths.

8 Kurze Zusammenfassung

Das Ziel der vorliegenden Arbeit war neue Möglichkeiten, aber auch Grenzen der Kernmagnetresonanz an Kleintieren an NMR - Systemen mit sehr hohen Feldstärken (bis zu 17.6 Tesla) zu erkunden. Anhand ausgesuchter Anwendungen wurden Methoden der Bildgebung (MRI), der Spektroskopie (MRS) als auch der spektroskopischen Bildgebung (MRSI) untersucht. Der Hauptteil der Arbeit beschäftigt sich mit der spektroskopischen Bildgebung von Natrium an Kleintieren. Weitere Themen sind die Protonenspektroskopie am Ratten- und Mäusehirn und die Untersuchung der Nachweisgrenze von mit Eisen markierten Stammzellen im Rattenhirn mittels der NMR Bildgebung.

Spektroskopische Bildgebung von Natrium wurde durchgeführt, da diese Anwendung von besonderem Maße von dem höheren Feld profitiert. Auf Grund des intrinsisch geringen Signals *in vivo*, welches seine Ursachen in den relativ geringen *in vivo* Konzentrationen und den kurzen Relaxationszeiten hat, wurden bisher nur NMR Untersuchungen an größeren Tieren durchgeführt. In der Literatur wurden bisher noch keine Untersuchungen an dem wichtigsten Labortier, der Maus, beschrieben. Diese Arbeit konzentrierte sich daher auf Untersuchungen an Kleintieren, sprich der Ratte und der Maus.

Um solche Untersuchungen durchführen zu können wurden im Rahmen der Arbeit angepasste NMR Resonatoren konstruiert, neue Pulssequenzen etabliert und Messungen an verschiedenen relevanten Organen an Kleintieren durchgeführt.

Die Untersuchungen am Hirnschlag bei der Ratte ergaben zwar nur eine geringfügige Verbesserung in der zeitlichen Auflösung (10%) im Vergleich zu den in der Literatur beschriebenen Studien, besitzen aber eine 19-fach höhere örtliche Auflösung. In künftigen Studien kann daher, je nach Bedarf, entweder die örtliche Auflösung beibehalten oder zu Gunsten der zeitlichen Auflösung reduziert werden. Die ersten jemals gezeigten Natrium Verteilungen im infarzierten Mäusehirn zeigen eindeutig den betroffenen Bereich und stimmen gut mit den höher aufgelösten Protonen Bildern überein. Zudem zeigen die infarzierten Bereiche einen erhöhten Wert der longitudinalen Relaxationszeiten

(T1), was gut mit den bisher veröffentlichten Werten im Rattenhirn übereinstimmt.

Eine hohe Herausforderung stellte die Darstellung der Natriumverteilung im Mäuseherzen dar. Hier waren nicht nur die geringen Natriumkonzentrationen sondern auch die geringe Größe (1cm³) als auch die Bewegungen auf Grund der Atmung und der schnellen Herzrate (~ 600 Schläge/min) zu berücksichtigen. In der vorliegenden Arbeit konnte sowohl der rechte als auch der linke Ventrikel und Teile des Myokardiums eindeutig identifiziert werden. Diese ersten jemals gezeigten Natrium Bilder vom Mäuseherzen bilden die Grundlage für künftige Studien. Untersuchungen des Natriumgehaltes im Verlauf eines Infarktes oder Phenotypisierung genmodifizierter Stämme sind nun denkbar.

Die außerordentlich wichtige Rolle der Niere die Natriumkonzentration des gesamten Körpers zu regulieren und dadurch Erkrankungen wie Bluthochdruck zu vermeiden gab Anlass Untersuchungen an der Mäuseniere durchzuführen. Es wurde nicht nur die Niere relativ hoch aufgelöst dargestellt, vielmehr konnte der Natriumverlauf von Nierenrinde (Cortex) über Nierenmark (Medulla) bis hin zum Nierenbecken (Pelvis renalis) beschrieben werden. Die durchgeführte funktionelle Studie, bei der der Maus ein Diuretikum verabreicht wurde ermöglichte den zeitlichen Verlauf der Konzentrationsveränderungen des Natriumgehaltes in den verschiedenen Nierenregionen zu messen. Die erhaltenen Verlaufsprofile und Zeitkonstanten der Konzentrationsveränderungen stimmen gut mit denen von Maril et al bei Ratten gemessenen überein. Um die Charakterisierung der Niere zu vervollständigen wurden zudem T1 und T2 in den verschiedenen Regionen bestimmt. Die erzielten Ergebnisse bilden die Grundlage für künftige Studien an verschiedenen Krankheitsmodellen an genveränderten Mausmodellen.

Zusammenfassend wurde in der vorliegend Arbeit die Machbarkeit von Natrium MRSI an verschiedenen Organen der Maus gezeigt. Die Experimente am Rattenhirn verbesserten die bisher erreichten Auflösungen um ein Vielfaches. Diese Ergebnisse sollten daher Grundlage und Anreiz für neue weiterführende Studien sein. Der durch das hohe statische Magnetfeld erzielte SNR Gewinn wurde entweder dazu genutzt die räumliche Auflösung zu erhöhen und/oder die zeitliche Auflösung zu verbessern.

Der zweite Teil der Arbeit konzentrierte sich auf Protonen MRS am Kleintierhirn. Hier war nicht nur das höhere SNR sondern auch der ebenfalls auf Grund des hohen Magnetfeldes erweiterte spektrale Bereich von Vorteil. Schwierigkeiten und Grenzen des hohen Feldes wurden in diesem Abschnitt ebenfalls untersucht.

Nachdem die nötige Wasserunterdrückung, eine automatisierte Shimroutine, die Lokalisation und die nötigen Wirbelstromkorrekturen am Phantom etabliert waren wurden Linienbreiten von weniger als 3 Hz am Phantom erreicht. Selbst J Kopplungskonstanten von GABA (7 Hz) konnten bestimmt werden. Die danach akquirierten Spektren im Ratten- und im Mäusehirn, die alle mit MRS bisher detektierten Metaboliten zeigen, sind die ersten die jemals bei 17,6 Tesla aufgenommen wurden.

Die in Kooperation mit Dr. Jürgen Schneider (University of Oxford) durchgeführte Studie, die als Ziel hatte die Relaxationszeiten (T1 und T2) der Hauptmetaboliten im Mäusehirn bei verschiedenen Feldstärken (11,7 Tesla in Oxford; 17.6 Tesla in Würzburg) zu bestimmen lieferte im Falle von T1 ergänzende Werte zu den erst kürzlich erschienenen Ergebnissen von de Graaf et al. Die neu entwickelte Methode um T2 von Metaboliten unabhängig vom NMR Gerät, explizit den Gradienten, zu messen wurde am Phantom erfolgreich getestet, litt allerdings auf Grund der begrenzten Messzeit bei den *in vivo* Messungen an einem zu geringen SNR. Nichts desto trotz sollte in künftigen Studien T2 bei verschiedenen Feldstärken mit dieser Gradienten unabhängigen Methode bestimmt werden.

Zusammenfassend wurde im zweiten Abschnitt der vorliegenden Arbeit gezeigt, dass generell hoch aufgelöste Spektren vom Ratten-/Mäusehirn bei 17,6 Tesla akquiriert werden können. Trotz der Probleme auf Grund des hohen Feldes sind die Spektren von hoher Qualität. Eine erhöhtes SNR und Vorteile durch die größere spektrale Auflösung sind klar zu erkennen.

Im dritten und letzten Teil der vorliegenden Arbeit wurde die Detektierbarkeitsgrenze von mit Eisen markierten Stammzellen mittels MRI untersucht. Nachdem Methoden etabliert wurden die Zellen mit VSOPs zu markieren, genau zu zählen und anschließenden Phantomexperimenten,

wurden verschiedene Mengen von markierten Stammzellen in das Striatum der Rattenhirne *in vivo* injiziert. Während 120.000, 1000 und 100 Zellen eindeutig auf Grund des hypointensen Signals bestimmt werden konnten, waren andere signalabschwächende Faktoren, wie kleine Blutungen, die am Einstichkanal der Nadel möglicherweise entstanden, oder Blutgefässe selbst der Grund warum 20 injizierte Zellen nicht eindeutig zugeordnet werden konnten. Nichts desto trotz zeigt diese Studie Richtgrößen an benötigten markierten Zellen für zukünftige Studien.

Insgesamt wurden in dieser Arbeit die vielen Vorteile, aber auch die Gebiete welche besondere Aufmerksamkeit bei Messungen an sehr hohen Magnetfeldern benötigen, aufgezeigt. Drei Themen im Bereiche der Kernspintomographie, der Spektroskopie und der spektroskopischen Bildgebung wurden im Detail untersucht. Obwohl durch das hohe Magnetfeld neue Schwierigkeiten bewältigt werden mussten, wäre keine der hier präsentierten Studien bei niedrigen Feldstärken durchführbar gewesen.

9   Bibliography

[1] Bransden B.H and Joachain C.J. 'Quantum Mechanics (2nd Edition)'. Prentice Hall, Harlow, (2000)

[2] F. Bloch, W.W. Hansen, M. Packard. 'Nuclear Induction'. Phys Rev 70, 460-474, (1946)

[3] Bloembergen N, Purcell EM, Pound RV. 'Relaxation effects in nuclear magnetic resonance absorption'. Phys.Rev. 73, 679-712, (1948)

[4] Solomon I. 'Relaxation Processes in a System of Two Spins' Physical Review 99, 559-566, (1955)

[5] de Graaf R. 'In – vivo NMR spectroscopy'. John Wiley & sons, Chichester, England, (1998)

[6] Pohmann R, von Kienlin M. 'Accurate phosphorous metabolite images of the human heart by 3D acquisition-weighted CSI'. Magn Reson Med. 45:817-26. (2001)

[7] von Kienlin M, 'Empfindlichkeit und Ortsaufloesung in der lokalisierten NMR- Spektroskopie'. Habilitationsschrift, Wuerzburg, (1996).

[8] Ernst RR. 'Sensitivity enhancement in magnetic resonance'. In: Waugh JS, editor. Adv Magn Reson. 2:1–135. (1966).

[9] Ernst RR, Bodenhausen G. 'Principles of NMR in One and Two Dimensions'. Oxford Science Publications, Clarendon Press, Oxford, (1987).

[10] Firbank MJ, Coulthard A, Harrison RM, Williams ED. 'A comparison of two methods for measuring the signal to noise ratio on MR images'. Phys Med Biol 44:N261-264, (1999).

[11] Haase A, Frahm D, Mattei W, H anicke W, Merboldt KD. 'FLASH Imaging. Rapid NMR Imaging Using Low Flip-Angle Pulses'. J Magn Reson 67:258-266 (1986).

[12] Ljunggren S. 'A Simple Graphical Representation of Fourier-Based Imaging Methods'. J Magn Reson 54:338-343 (1983).

[13] Bottomley US - Patent 4'480'228:0, (1984)

[14] Naressi A, Couturier C, Castang I, de Beer R, Graveron-Demilly D. 'Java-based graphical user interface for MRUI, a software package for

quantitation of in vivo/medical magnetic resonance spectroscopy signals'. Comput Biol Med; 31(4):269-286, (2001).

[15] Levitt M,' Spin Dynamics: Basics of Nuclear Magnetic Resonance', Wiley & sons, Chichester,England, (2001).

[16] Starcuk Z, Sklenar V, 'New hard pulse sequences for solvent signal suppression in Fourier transform NMR I'. J Magn Res 61, 567 – 570, (1985).

[17] Starcuk Z, Sklenar V, 'New hard pulse sequences for solvent signal suppression in Fourier transform NMR II'. J Magn Res 66, 391 – 397, (1986).

[18] Piotto M, Saudek V, Sklenar V. 'Gradient-tailored excitation for single-quantum NMR spectroscopy of aqueous solutions'. J Biomol NMR; 2(6):661-5 (1992).

[19] Mescher M,Tannus A, O`Neil Johnson M, Garwood M, 'Solvent suppression using selective echo dephasing'. J Magn Res A 123, 226 – 229, 1996.

[20] Hwang TL, Shaka AJ, 'Water suppression that works. Excitation sculpting using arbitrary wave forms and pulsed field gradients'. J Magn Res A, 112. 275-279, 1995

[21] Haase A, Frahm J, Hanicke W, Matthaei D., '1H NMR chemical shift selective (CHESS) imaging', Phys Med Biol.; 30(4):341-4 (1985).

[22] Moonen CT, van Zijl PC, 'Highly effective water suppression for in vivo proton NMR spectroscopy (DRYSTEAM)'. J Magn Res 88, 28 – 41, (1990).

[23] Griffey RH, Flamig DP. 'VAPOR for solvent – suppressed, short echo, volume – localized proton spectroscopy'. J Magn Res 88, 161 – 166, (1990)

[24] Moonen CT, von Kienlin M, van Zijl PC, Cohen J, Gillen J, Daly P, Wolf G. Comparison of single-shot localization methods (STEAM and PRESS) for in vivo proton NMR spectroscopy. NMR Biomed. 2(5-6): 201-8, (1989).

[25] Dong Z, Dreher W, Leibfritz D. 'Toward Quantitative Short-Echo-Time In Vivo Proton MR Spectroscopy Without Water Suppression' Magn Reson Med. 55:1441-1446, (2006).

[26] Kreis R., 'Issues of spectral quality in clinical 1H-magnetic resonance spectroscopy and a gallery of artifacts'. NMR Biomed, 17(6):361-81 2004.

[27] Mao XA, Ye CH, 'Understanding radiation damping in a simple way'. Concepts Magn Reson **9**: 173-187, (1997).

[28] Szantay C, Demeter A, 'Radiation Damping Diagnostics', Concepts Magn Reson **11**: 121-145, (1999).

[29] Picard L, von Kienlin M, Decorps M, 'An overcoupled NMR probe for the reduction of radiation damping', J Magn Reson A **117**:262-266, (1995).

[30] Ordidge RJ, Cresshull ID. 'The correction of transient B0 field shifts following the application of pulsed gradients by phase correction in the time domain'. J. Magn. Reson.; 69: 151–155, (1986).

[31] de Graaf AA, van Dijk JE, Bovee WMMJ. 'QUALITY: quantification improvement by converting lineshapes to the Lorentzian type'. Magn. Reson. Med.; 13: 343–357, (1990).

[32] Klose U. 'In Vivo Proton Spectroscopy in Presence of Eddy Currents'. Magn Reson Med. 14: 26-30, (1990).

[33] Provencher SW. 'Estimation of metabolite concentration from localized in vivo proton NMR spectra'. Magn. Reson. Med; 30: 672–679, (1993).

[34] Mareci TH, Brooker HR. 'High-resolution magnetic resonance spectra from a sensitive region defined with pulsed field gradients'. J Magn Reson 57:157-163, (1984).

[35] Brooker HR, Mareci TH, Mao JT. 'Selective Fourier transform localization'. Magn Reson Med 5:417-433, (1987).

[36] Constable RT, Spencer DD. 'Composite Image Formation in z-Shimmed Functional MR Imaging'. Magn Reson Med 42:110–117 (1999)

[37] Goodman JA, Kroenke CD, Bretthorst GL, Ackerman JJH, Neil JJ. 'Sodium Ion Apparent Diffusion Coefficient in Living Rat Brain'. Magn Reson Med 53: 1040 - 1045 (2005)

[38] Miller SK, Elgavish SE. 'Shift - reagent – aided ^{23}Na NMR spectroscopy in cellular and whole – organ systems'. Biological Magnetic Resonance Vol. 11: In Vivo spectroscopy, Plenum Press, New York, USA, (1992).

[39] C.E. Hayes, W.A. Edelstein, J.F. Schenck, O.M. Mueller und M. Eash: 'An Efficient, Highly Homogeneous Radiofrequency Coil for Whole-Body NMR Imaging at 1.5 T'. J.Magn.Reson. 63: 622 - 628 (1985).

[40] Watkins JC, Fukushima E. 'High - pass bird – cage coil for nuclear – magnetic resonance'. Rev. Sci. Instrum. 59 (6): 926 - 929 (1988)

[41] Sank VJ, Chen CN, Hoult DI. 'A Quadrature Coil for the Adult Human Head'. J.Magn.Reson. 69: 236 – 242 (1986).

[42] Tropp J, Derby K: 'The loss of signal to noise due to imperfect isolation between the channels of a quadrature nuclear magnetic resonance probe', Rev. of Sci. Instrum. 62: 2646 (1991).

[43] Mispelter J, Lupu M, Briguet. 'NMR PROBEHEADS FOR BIOPHYSICAL AND BIOMEDICAL EXPERIMENTS. Theoretical Principles and Practical Guidelines'. World Sci. Pub. Comp. (2006)

[44] Chen CN, Sank VJ, Cohen SM, Hoult DI: 'The field dependence of NMR imaging I. Laboratory assessment of signal-to noise ratio and power deposition'. Magn Reson Med 3: 722 (1986).

[45] Link J. 'The design of resonator probes with homogeneous radiofrequency fields' in: Diehl P, Fluck E, Guenther H, Kosfeld R. 'In-vivo magnetic resonance spectroscopy I'. Springer (1992).

[46] Haase A, Odoj F, von Kienlin M, Warnking J, Fidler F, Weisser A, Nittka M, Rommel E, Lanz T, Kalusche B, Griswold M. 'NMR Probeheads for In Vivo Applications' Concepts in Magnetic Resonance 12(6): 361 – 388 (2000)

[47] Doty FD, Connick TJ, Ni XZ, Clingan MN. 'Noise in high power, high frequency double tuned probes'. J Magn Reson 77:536 – 549 (1988).

[48] Murphy-Boesch J, So GJ, James TL: 'Precision Mapping of the B1 Field Using the Rotating-Frame Experiment'. J.Magn.Reson. 73: 293 - 303 (1987).

[49] Ross B, Bluml S. 'Magnetic resonance spectroscopy of the human brain'. Anat Rec. 265(2):54-84, (2001).

[50] Govindaraju V, Young K, Maudsley AA. 'Proton NMR chemical shifts and coupling constants for brain metabolites'. NMR Biomed, 13(3):129-53, (2000).

[51] Bates TE, Williams SR, Gadian DG, Bell JD, Small RK, Iles RA. '1H NMR study of cerebral development in the rat'. NMR Biomed. 2(5-6):225-9, (1989).

[52] Frahm J, Bruhn H, Gyngell ML, Merboldt KD, Hanicke W, Sauter R. 'Localized proton NMR spectroscopy in different regions of the human brain in vivo. Relaxation times and concentrations of cerebral metabolites'. Magn Reson Med. 11(1):47-63, (1989).

[53] Wang Y, Li SJ. 'Differentiation of metabolic concentrations between gray matter and white matter of human brain by in vivo 1H magnetic resonance spectroscopy'. Magn Reson Med 39(1): 28 – 33, (1998).

[54] Leibfritz D, Dreher W. 'Magnetization transfer MRS'. NMR Biomed. 14:65-76, (2001).

[55] Katz-Brull R, Lavin PT, Lenkinski RE. 'Clinical utility of proton magnetic resonance spectroscopy in characterizing breast lesions'. J Natl Cancer Inst. 94(16):1197-203, (2002).

[56] Thulborn KR, Gindin TS, Davis D, Erb P. 'Comprehensive MRI Protocol for Stroke Management: Tissue Sodium Concentration as a Measure of Tissue Viability in Nonhuman Primate Studies and in Clinical Studies'. Radiology 213:156-166, (1999)

[57] Lin SP, Song SK, Miller JP, Ackerman JJ, Neil JJ. 'Direct, longitudinal comparison of (1)H and (23)Na MRI after transient focal cerebral ischemia. Stroke'. 32(4):925-32. (2001)

[58] Wang Y, Hu W, Perez-Trepichio AD, Ng TC, Furlan AJ, Majors AW, Jones SC. 'Brain tissue sodium is a ticking clock telling time after arterial occlusion in rat focal cerebral ischemia'. Stroke. 31(6):1386-91; discussion 1392. (2000)

[59] Ouwerkerk R, Bleich KB, Gillen JS, Pomper MG, BottomleyPA. ''Tissue sodium concentration in human brain tumors as measured with 23Na MR imaging'. Radiology 227:529–537. (2003)

[60] Thulborn KR, Davis D, Adams H, Gindin T, Zhou J. 'Quantitative tissue sodium concentration mapping of the growth of focal cerebral tumors with sodium magnetic resonance imaging'. Magn Reson Med. 41(2):351-9. (1999)

[61] Lingrel JB, Kuntzweiler T. 'Na$^+$, K$^+$ - ATPase'. JBiolChem. 269:31: 19659 – 19662 (1994)

[62] DeWeer P. in: 'The Kidney: Physiology and Pathophysiology' (DW Seldin, and G. Giebisch, eds) p. 31, Raven, New York (1985)

[63] Glynn IM, Karlish SJD, Annu. Rev. Biochem. 59,171-205 (1990)

[64] Cameron IL, Smith NKR, Pool TB, Sparks RL. 'Intracellular concentration of sodium and other elements as related to mitogenesis and oncogenesis in vivo'. Cancer Res 40:1493–1500. (1980)

[65] Hashimoto T, Ikehira H, Fukuda H, Yamaura A, Watanabe O, Tateno Y, Tanaka R, Simon HE. 'In vivo sodium-23 MRI in brain tumors: evaluation of preliminary clinical experience'. Am J Physiol Imaging 6:74–80. (1991)

[66] Liou IC. 'Vergleich von linear polarisierten und Quadratur-Birdcage-Resonatoren für X-Kerne bei 17.6 T'. Diplomarbeit, EP5, Universitaet Wuerzburg, (2004).

[67] Behr VC. Dissertation, EP5, Universitaet Wuerzburg, (2008)

[68] Gravina S, Cory DG. 'Sensitivity and resolution of constant-time imaging'. J Magn Reson B. 104: 53-61, (1994).

[69] Balcom BJ, Macgregor RP, Beyea SD, Green DP, Armstrong RL, Bremner TW. 'Single-Point Ramped Imaging with T1 Enhancement (SPRITE)' J Magn Reson A. 123(1):131-4, (1996).

[70] Boada FE, Shen GX, Chang SY, Thulborn KR. 'Spectrally weighted twisted projection imaging: reducing T2 signal attenuation effects in fast three-dimensional sodium imaging'. Magn Reson Med. 38(6):1022-8, (1997).

[71] Boada FE, Gillen JS, Shen GX, Chang SY, Thulborn KR. 'Fast three dimensional sodium imaging'. Magn Reson Med. 37(5): 706-715, (1997).

[72] Brown TR, Kincaid BM, Ugurbil K. 'NMR chemical shift imaging in three dimensions'. Proc Natl Acad Sci U S A. 79(11):3523-6, (1982).

[73] Brooker HR, Mareci TH, Mao JT. 'Selective Fourier transform localization'. Magn Reson Med 5: 417-433, (1987).

[74] Mareci TH, Brooker HR. 'Essential considerations for spectral localization using indirect gradient encoding of spatial information'. J Magn Reson 92: 229-246, (1991).

[75] Webb AG, Briggs RW, Mareci TH. 'Volume localized spectroscopy using the selective Fourier transform with windowing by variable tip angle excitation'. J Magn Reson 94:174-179, (1991).

[76] Webb AG, Mareci TH, Briggs RW. 'Relative efficiencies of phase encoded localized NMR methods'. J Magn Reson Ser B 103: 274-277, (1994).

[77] Greiser A, von Kienlin M. 'Efficient k-space sampling by density-weighted phase-encoding'. Magn Reson Med 50(6):1266-75, (2003).

[78] Pohmann R, von Kienlin M, Haase A. 'Theoretical evaluation and comparison of fast chemical shift imaging methods'. J Magn Reson. 129(2):145-60, (1997).

[79] Mareci TH, Brooker HR. 'Essential considerations for spectral localization using indirect gradient encoding of spatial information'. J Magn Reson 92: 229-246, (1991).

[80] Carr HY, Purcell EM. 'Effects of diffusion on free precession in nuclear magnetic resonance experiments'. Phys. Rev, 94, 630 – 638. (1954).

[81] Meiboom S, Gillen D. 'Modified spin - echo method for measuring nuclear relaxation times'. Rev. Sci. Instrum. 29, 688 – 691. (1958)

[82] Hilal Sk, Maudsley AA, Ra JB, Simon HE. Roschmann P, Wittekoek S, Cho ZH, Mun SK. 'In vivo NMR imaging of sodium-23 in the human Head'. J Comput Assist Tomogr. 9: 1 – 7 (1985)

[83] Winkler SS, Thomasson DM, Sherwood K, Perman WH. 'Regional T2 and sodium concentration estimates in the normal human brain by sodium-23 MR imaging at 1.5 T'. J Comput Assist Tomogr. 13(4):561-6. (1989)

[84] Boada FE, Christensen JD, Huang-Hellinger FR, Reese TG, Thulborn KR, 'Quantitative in vivo tissue sodium concentration maps: the effects of biexponential relaxation'. Magn Reson Med. 32(2):219-23. (1994)

[85] Christensen JD, Barrere BJ, Boada FE, Vevea JM, Thulborn KR. 'Quantitative tissue sodium concentration mapping of normal rat brain'. Magn Reson Med. 36(1):83-9 (1996).

[86] Bartha R, Lee TY, Hogan MJ, Hughes S, Barberi E, Rajakumar N, Menon RS. 'Sodium T2*-weighted MR imaging of acute focal cerebral ischemia in rabbits'. Magn Reson Imaging., 22(7):983-91. (2004)

[87] Liu H, Snyder C, Vaughan T, Urgubil K. 'Apractical sodium imaging method at 7T'. Proc. Intl. Soc. Mag. Reson. Med. 13 (2005)

[88] Clayton DB, Lenkinski RE. 'MR imaging of sodium in the human brain with a fast three-dimensional gradient-recalled-echo sequence at 4 T'. Acad Radiol.;10(4):358-65. (2003)

[89] Kohler S, Preibisch C, Nittka M, Haase A. 'Fast three-dimensional sodium imaging of human brain'. MAGMA.;13(2):63-9. (2001)

[90] Bartha R, Menon RS. 'Long component time constant of 23Na T*2 relaxation in healthy human brain'. Magn Reson Med., 52(2):407-10. (2004)

[91] Greiser A, Haase A, von Kienlin M. 'Improved cardiac sodium MR imaging by density-weighted phase-encoding'. J Magn Reson Imaging. 2005 Jan;21(1):78-81.

[92] Schepkin VD, Ross BD, Chenevert TL, Rehemtulla A, Sharma S, Kumar M, Stojanovska J. 'Sodium Magnetic Resonance Imaging of Chemotherapeutic Response in a Rat Glioma'. Magnetic Resonance in Medicine 53:85–92 (2005)

[93] Ruff J, Wiesmann F, Hiller KH, Voll S, von Kienlin M, Bauer WR, Rommel E, Neubauer S, Haase A. 'Magnetic resonance micro imaging for non invasive quantification of myocardial function and mass in the mouse'. Magn Reson Med. 40(1):43-8, (1998).

[94] Slawson SE, Roman BB, Williams DS, Koretsky AP. 'Cardiac MRI of the normal and hypertrophied mouse heart. Magn Reson Med 39: 980-987, (1998).

[95] Kim RJ, Lima JA, Chen EL, Reeder SB, Klocke FJ, Zerhouni EA, Judd RM. 'Fast 23Na magnetic resonance imaging of acute reperfused myocardial infarction. Potential to assess myocardial viability'. Circulation. 95(7):1877-85,(1997).

[96] Pabst T, Sandstede J, Beer M, Kenn W, Greiser A, von Kienlin M, Neubauer S, Hahn D. 'Optimization of ECG-triggered 3D (23)Na MRI of the human heart'. Magn Reson Med. 45(1):164-6, (2001).

[97] Sandstede JJW, Pabst T, Beer M, et al. '23Na magnetic resonance imaging for the assessment of myocardial infarction in humans - comparison with cine MRI and delayed contrast enhancement'. Radiology 221: 222-228, (2001).

[98] Kim RJ, Judd RM, Chen EL, Fieno DS, Parrish TB, Lima JA. 'Relationship of elevated 23Na magnetic resonance image intensity to infarct size after acute reperfused myocardial infarction'. Circulation. 100(2):185-92, (1999).

[99] Constantinides CD, Kraitchman DL, O'Brien KO, Boada FE, Gillen J, Bottomley PA. 'Noninvasive quantification of total sodium concentrations in acute reperfused myocardial infarction using 23Na MRI'. Magn Reson Med. 46(6):1144-51, (2001).

[100] Weidensteiner C, Horn M, Fekete E, Neubauer S, von Kienlin M. 'Imaging of intracellular sodium with shift reagent aided (23)Na CSI in isolated rat hearts'. Magn Reson Med. 48(1):89-96, (2002).

[101] Frahm J, Haase A, Matthaei D. 'Rapid NMR imaging of dynamic processes using the FLASH technique'. Magn Reson Med 3: 321-327, (1986).

[102] Hricak H, Williams RD. 'Magnetic resonance imaging and its application in urology'. Urology 23(5): 442-54 (1984)

[103] Schneider G, Seidel R, Fries P. 'Magnetic resonance imaging in urology. Current techniques'. Urologe A. 43(11): 1385-90. (2004)

[104] Grenier N, Basseau F, Ries M, Tyndal B, Jones R, Moonen C. 'Functional MRI of the kidney'. Abdom Imaging. 28(2):164-75. Review. (2003)

[105] Laurent D, Poirier K, Wasvary J, Rudin M. 'Effect of essential hypertension on kidney function as measured in rat by dynamic MRI'. Magn Reson Med. Jan;47(1):127-34. (2002)

[106] Li L, Storey P, Kim D, Li W, Prasad P. 'Kidneys in hypertensive rats show reduced response to nitric oxide synthase inhibition as evaluated by BOLD MRI'. J Magn Reson Imaging. 17(6):671-5. (2003)

[107] Steidle G, Graf H, Schick F. 'Sodium 3-D MRI of the human torso using a volume coil'. Magn Reson Imaging. 22(2):171-80. (2004)

[108] Maril N, Margalit R, Mispelter J, Degani H. 'Functional sodium magnetic resonance imaging of the intact rat kidney'. Kidney Int. 65(3):927-35. (2004)

[109] Maril N, Margalit R, Mispelter J, Degani H. 'Sodium magnetic resonance imaging of diuresis: spatial and kinetic response'. Magn Reson Med. 53(3):545-52. (2005)

[110] Maril N, Margalit R, Rosen S, Heyman SN, Degani H. 'Detection of evolving acute tubular necrosis with renal 23Na MRI: studies in rats'. Kidney Int. 69(4):765-768. (2006)

[111] Buerkert J, Martin D, Prasad J, Trigg D. 'Role of deep naphrons and the terminal collecting duct in a mannitol- induced diuresis'. Am J Physiol 240: F411 – 422 (1981)

[112] Atherton JC, Hai MA, Thomas S. 'The time course of chances in renal tissue composition during mannitol diuresis in the rat'. J Physiol 197: 411 – 428 (1968)

Bibliography

[113] Romano G, Favret G, Federico E, Bartoli E. 'The site of action of furosemide'. Pharmacol Res. 37(5):409-19. (1998)

[114] Greger R. 'How does the macula densa sense tubule function?': Nephrol Dial Transplant 12:2215-2217. (1997)

[115] Greger R. 'Physiology of renal sodium transport'. Am J Sci 319:51-62. (2000)

[116] Gareis DL, Neuberger T, Behr VC, Jakob PM, Faber C, Griswold MA. 'Transmit-Receive Coil-Arrays at 17.6T, Configurations for 1H, 23Na and 31P MRI'. Concepts Magn Reson Eng 29B: 20-27 (2006)

[117] Pfeuffer J, Tkac I, Provencher SW, Gruetter R. 'Toward an in vivo neurochemical profile: quantification of 18 metabolites in short-echo-time (1)H NMR spectra of the rat brain'. J Magn Reson. 141(1):104-20, (1999).

[118] van der Toorn A, Dijkhuizen RM, Tulleken CA, Nicolay K. 'T1 and T2 relaxation times of the major 1H-containing metabolites in rat brain after focal ischemia'. NMR Biomed. 8(6):245-52, (1995).

[119] de Graaf RA, Brown PB, McIntyre S, Nixon TW, Behar KL, Rothman DL. 'High magnetic field water and metabolite proton T1 and T2 relaxation in rat brain in vivo'. Magn Reson Med. 56(2):386-94, (2006).

[120] Gruetter R. 'Automatic, localized in vivo adjustment of all first- and second-order shim coils'. Magn Reson Med. 29(6):804-11, (1993).

[121] Frahm J, Haase A, Matthaei D, Merboldt KD, Ha¨nicke W. 'Rapid NMR imaging using stimulated echoes'. J Magn Reson 65:130–135, (1985).

[122] Gburek B. ‚NMR-Spektroskopie: Aufnahme eines Basisdatensatzes für die Spektrenanalyse mit der Auswertungssoftware LCModel', Projektpraktikum am Lehrstuhl für Experimentelle Physik 5, Wuerzburg, Germany, (2004)

[123] Terpstra PM, Andersen PM, Gruetter R. 'Localized eddy current compensation using quantitative field mapping'. JMR 131(1):139-43, (1998).

[124] Choi CB, Kim HY, Han DY, Kang YW, Han YM, Jeun SS, Choe BY. 'In vivo 1H MR spectroscopic findings in traumatic contusion of ICR mouse brain induced by fluid percussion injury'. Eur J Radiol. 55(1):96-101 (2005), (Epub 2004).

[125] Schwarcz A, Natt O, Watanabe T, Boretius S, Frahm J, Michaelis T. 'Localized proton MRS of cerebral metabolite profiles in different mouse strains'. Magn Reson Med. 49(5):822-7. (2003)

[126] Hesselbarth D, Franke C, Hata R, Brinker G, Hoehn-Berlage M. 'High resolution MRI and MRS: a feasibility study for the investigation of focal cerebral ischemia in mice'. NMR Biomed. 11(8):423-9. (1998).

[127] Gruetter R, Weisdorf SA, Rajanayagan V, Terpstra M, Merkle H, Truwit CL, Garwood M, Nyberg SL, Ugurbil K. Resolution improvements in in vivo 1H NMR spectra with increased magnetic field strength. J Magn Reson. 135(1):260-4. (1998).

[128] Tkac I, Henry PG, Andersen P, Keene CD, Low WC, Gruetter R. 'Highly resolved in vivo 1H NMR spectroscopy of the mouse brain at 9.4 T'. Magn Reson Med. 52(3):478-84. (2004).

[129] Geppert C, Dreher W, Leibfritz D. 'PRESS-based proton single-voxel spectroscopy and spectroscopic imaging with very short echo times using asymmetric RF pulses'. MAGMA. 16(3):144-8, (2003).

[130] Marshall I, Wardlaw J, Graham C, Murray L, Blane A. 'Repeatability of long and short echo-time in vivo proton chemical-shift imaging'. Neuroradiology. 44(12):973-80, (2002).

[131] Naressi A, Couturier C, Castang I, de Beer R, Graveron-Demilly D. 'Java-based graphical user interface for MRUI, a software package for quantitation of in vivo/medical magnetic resonance spectroscopy signals'. Comput Biol Med; 31(4):269-286, (2001).

[132] Vanhamme L, van den Boogaart A, Van Huffel S. 'Improved method for accurate and efficient quantification of MRS data with use of prior knowledge'. J Magn Reson; 129:35-43, (1997).

[133] Van Hecke P, Van Huffel S (editors), 'Special Issue: NMR Spectroscopy Quantitation'. NMR in Biomed 14(4) (2001).

[134] Isacson O, Bjorklund LM, Schumacher JM. ,Toward full restoration of synaptic and terminal function of the dopaminergic system in Parkinson's disease by stem cells'. Ann Neurol. 53 Suppl 3: 135-146, (2003).

[135] Sun ZH, Lai YL, Zeng WW et al. 'Mesencephalic progenitors can improve rota-tional behavior and reconstruct nigrostriatal pathway in PD rats'. Acta Neu-rochir Suppl. 87:175-180, (2003).

[136] Bjorklund LM, Sanchez-Pernaute R, Chung S et al. 'Embryonic stem cells develop into functional dopaminergic neurons after transplantation in a Parkinson rat model'. Proc Natl Acad Sci U S A. 99:2344-2349, (2002).

[137] Fukunaga A, Uchida K, Hara K et al. 'Differentiation and angiogenesis of central nervous system stem cells implanted with mesenchyme into ischemic rat brain'. Cell Transplant. 8:435-441, (1999).

[138] Modo M, Rezaie P, Heuschling P et al. 'Transplantation of neural stem cells in a rat model of stroke: assessment of short-term graft survival and acute host immunological response'. Brain Res. 958:70-82, (2002).

[139] Ben Hur T, Einstein O, Mizrachi-Kol R et al. 'Transplanted multipotential neural precursor cells migrate into the inflamed white matter in response to ex-perimental autoimmune encephalomyelitis'. Glia. 41:73-80, (2003).

[140] Bulte JW, Ben Hur T, Miller BR et al. 'MR microscopy of magnetically labeled neurospheres transplanted into the Lewis EAE rat brain'. Magn Reson Med. 50:201-205, (2003).

[141] Pluchino S, Quattrini A, Brambilla E et al. 'Injection of adult neurospheres induces recovery in a chronic model of multiple sclerosis'. Nature. 422:688-694, (2003).

[142] Check E. 'Parkinson's transplant therapy faces setback'. Nature. 424:987, (2003).

[143] Eskandar EN, Flaherty A, Cosgrove GR et al. 'Surgery for Parkinson disease in the United States, 1996 to 2000: practice patterns, short-term outcomes, and hospital charges in a nationwide sample'. J Neurosurg. 99:863-871, (2003).

[144] Lindvall O, Sawle G, Widner H et al. 'Evidence for long-term survival and func-tion of dopaminergic grafts in progressive Parkinson's disease'. Ann Neu-rol. 35:172-180, (1994).

[145] Renshaw PF, Owen CS, McLaughlin AC et al. 'Ferromagnetic contrast agents: a new approach'. Magn Reson Med. 3:217-225, (1986).

[146] Arbab AS, Bashaw LA, Miller BR et al. 'Intracytoplasmic tagging of cells with ferumoxides and transfection agent for cellular magnetic resonance imag-ing after cell transplantation: methods and techniques'. Transplantation. 76:1123-1130, (2003).

[147] Bowen CV, Zhang X, Saab G et al. 'Application of the static dephasing regime theory to superparamagnetic iron-oxide loaded cells'. Magn Reson Med. 48:52-61, (2002).

[148] Hinds KA, Hill JM, Shapiro EM et al. 'Highly efficient endosomal labeling of pro-genitor and stem cells with large magnetic particles allows magnetic reso-nance imaging of single cells'. Blood. 102:867-872, (2003).

[149] Frank JA, Miller BR, Arbab AS et al. 'Clinically applicable labeling of mammalian and stem cells by combining superparamagnetic iron oxides and transfec-tion agents'. Radiology. 228:480-487, (2003).

[150] Lewin M, Carlesso N, Tung CH et al. 'Tat peptide-derivatized magnetic nanoparti-cles allow in vivo tracking and recovery of progenitor cells'. Nat Biotech-nol. 18:410-414, (2000).

[151] Moore A, Weissleder R, Bogdanov A, Jr. 'Uptake of dextran-coated monocrystal-line iron oxides in tumor cells and macrophages'. J Magn Reson Imaging. 7:1140-1145, (1997).

[152] de Laquintane BD, Dousset V, Solanilla A et al. 'Iron particle labeling of haemato-poietic progenitor cells: an in vitro study'. Biosci Rep. 22:549-554, (2002).

[153] Fleige G, Nolte C, Synowitz M et al. 'Magnetic labeling of activated mi-croglia in experimental gliomas'. Neoplasia. 3:489-499, (2001).

[154] Bulte JW, Zhang S, van Gelderen P et al. 'Neurotransplantation of mag-netically labeled oligodendrocyte progenitors: magnetic resonance tracking of cell migration and myelination'. Proc Natl Acad Sci U S A. 96:15256-15261, (1999).

[155] Bulte JW, Douglas T, Witwer B et al.' Monitoring stem cell therapy in vivo using magnetodendrimers as a new class of cellular MR contrast agents'. Acad Radiol. 9 Suppl 2:S332-S335, (2002).

[156] Bulte JW, Duncan ID, Frank JA. 'In vivo magnetic resonance tracking of magneti-cally labeled cells after transplantation'. J Cereb Blood Flow Me-tab. 22:899-907, (2002).

[157] Modo M, Cash D, Mellodew K et al. 'Tracking transplanted stem cell mi-gration using bifunctional, contrast agent-enhanced, magnetic resonance imaging. Neuroimage'. 17:803-811, (2002).

[158] Hill JM, Dick AJ, Raman VK et al. 'Serial cardiac magnetic resonance imaging of injected mesenchymal stem cells'. Circulation. 108:1009-1014, (2003).

[159] Kraitchman DL, Heldman AW, Atalar E et al. 'In vivo magnetic resonance imag-ing of mesenchymal stem cells in myocardial infarction'. Circulation. 107:2290-2293, (2003).

[160] Hoehn M, Kustermann E, Blunk J et al. ‚Monitoring of implanted stem cell migra-tion in vivo: a highly resolved in vivo magnetic resonance imaging inves-tigation of experimental stroke in rat'. Proc Natl Acad Sci U S A. 99:16267-16272, (2002).

[161] Jendelova P, Herynek V, DeCroos J et al. 'Imaging the fate of implanted bone mar-row stromal cells labeled with superparamagnetic nanoparticles'. Magn Reson Med. 50:767-776, (2003).

[162] Zhang ZG, Jiang Q, Zhang R et al. 'Magnetic resonance imaging and neurosphere therapy of stroke in rat'. Ann Neurol. 53:259-263, (2003).

[163] Foster-Gareau P, Heyn C, Alejski A et al. 'Imaging single mammalian cells with a 1.5 T clinical MRI scanner'. Magn Reson Med. 49:968-971, (2003).

[164] Stroh A*, Faber C*, Neuberger T, Lorenz P, Sieland K, Jakob PM, Webb A, Pilgrimm H, Schober R, Pohl E, Zimmer C. 'In vivo detection limits of magnetically labeled embryonic stem cells in the rat brain using high-field (17.6 T) magnetic resonance imaging'. Neuroimage, 24, 635-645 (2005). (* equal contribution)

[165] Stroh A., Zimmer C. Gutzeit C. et al. ‚Iron-oxide-particles for molecular magnetic-resonance-imaging cause transient oxidative stress in rat macro-phages'. Free Radic Biol Med. 36(8):976-84, (2004).

[166] Kohler S, Hiller KH, Griswold M et al. 'NMR-microscopy with TrueFISP at 11.75T'. J Magn Reson. 161:252-257, (2003).

10 Danksagung

Die hier präsentierte Arbeit wäre ohne die Mithilfe und Zusammenarbeit vieler Personen nicht möglich gewesen, deshalb möchte ich mich hiermit bedanken bei:

Danksagung

- Und schliesslich bei meiner Familie, ohne deren Unterstützung dies alles sicherlich nicht möglich gewesen wäre.

Scientific Papers

T. Neuberger, N. Srenivasulu, M. Rokitta, H. Rolletschek, C. Gabel, T. Rutten, V. Radchuk, I. Feussner, U. Wobus, P. Jakob, A. Webb, L. Borisjuk *"Quantitative imaging of oil storage in developing crop seeds"* Plant Biotechnol J., 6(1):31-45 (2008). Epub 2007 Sep 25.

T. Neuberger, V. Gulani, A. Webb *"Sodium renal imaging in mice at high magnetic fields"* MRM, 58(5):1067-71 (2007)

B.A. Craven, **T. Neuberger**, E.G. Paterson, A.G. Webb, E.M. Josephson, E.E. Morrison, G.S. Settles *"Reconstruction and Morphometric Analysis of the Nasal Airway of the Dog (Canis familiaris) and Implications Regarding Olfactory Airflow"* Anat Rec (Hoboken), 290(11):1325-40 (cover story) (2007)

D. Gareis, **T. Neuberger**, V. C. Behr, P. M. Jakob, C. Faber, M. A. Griswold *„Transmit-Receive Coil-Arrays at 17.6T, Configurations for 1H, 23Na and 31P MRI"* Concepts Magn Reson Part B- Magn Reson Eng, 29B (1): 20-27 (2006)

Weber T, Vroemen M, Behr V, **Neuberger T**, Jakob P, Haase A, Schuierer G, Bogdahn U, Faber C, Weidner N. *"In vivo high-resolution MR imaging of neuropathologic changes in the injured rat spinal cord"* AJNR, 27(3):598-604 (2006)

V. Gulani, T. Weber, **T. Neuberger**, A. G. Webb: *„Improved time efficiency and accuracy in diffusion tensor microimaging with multiple echo acquisition".* J Magn Reson, 177(2): 329-35 (2005)

KH Hiller, C Faber, **T Neuberger**, S Kohler, A Stroh, C Zimmer, P Jakob: *„Magnetic resonance tomography: potentials of molecular imaging".* Z Med Phys, 15(3):155-62 (2005)

L. Borisjuk, T. H. Nguyen, **T. Neuberger**, H. Tschiersch, T. Rutten, B. Claus, I. Feussner, P. Jakob, A. G. Webb, H. Weber, H. Rolletschek: *„ Regulation of lipid biosynthesis in soybean seeds: shift from photosynthesis to storage is a gradient coordinated with trans-differentiation of plastids".* New Phytol., 167(3):761-76 (2005).

A. Stroh*, C. Faber*, **T. Neuberger**, P. Lorenz, K. Sieland, P. M. Jakob, A. Webb, H. Pilgrimm, R. Schober, E. Pohl, and C. Zimmer. *„In vivo detection limits of magnetically labeled embryonic stem cells in the rat brain using high-field (17.6 T) magnetic resonance imaging".* Neuroimage, 24: 635-645 (2005). (* equal contribution)

A. Steinbrecher, T. Weber, **T. Neuberger**, A. Mueller, X. Pedre, G. Giegerich, U. Bogdahn, P. Jakob, A. Haase, and C. Faber. *„Experimental autoimmune encephalomyelitis in the rat spinal cord: lesion detection with high-resolution MR microscopy at 17.6 T.".* Am. J. Neuroradiol. 26: 19-25 (2005)

T. Neuberger, A. Greiser , M. Nahrendorf, C. Faber, and A. Webb. *„23Na microscopy of the mouse heart in vivo using density weighted chemical shift imaging"*, MAGMA, 17: 196-200 (2004)

A. Purea, **T. Neuberger**, A.G. Webb „Simultaneous NMR microimaging of multiple single-cell samples" Concepts Magn Reson Eng 22B (1): 7-14 (2004)

V.C. Behr, T. Weber, **T. Neuberger**, M. Vroemen, N. Weidner, U. Bogdahn, A. Haase, P.M. Jakob, C. Faber, *"High-resolution MR imaging of the rat spinal cord in vivo in a wide-bore magnet at 17.6 Tesla"*, MAGMA 17: 353-358 (2004)

H. Schneider, B. Manz, M. Westhoff, S. Mimietz, M. Szimtenings, **T. Neuberger**, C. Faber, G. Krohne, A. Haase, F. Volke, and U. Zimmermann. *„The impact of lipid distribution, composition and mobility on xylem water refilling of the resurrection plant Myrothamnus flabellifolia",* New Phytol, 159: 487-505 (2003)

Nahrendorf M, Hiller KH, Greiser A, Kohler S**, Neuberger T**, Hu K, Waller C, Albrecht M, Neubauer S, Haase A, Ertl G, Bauer WR. Chronic coronary artery stenosis induces impaired function of remote myocardium: MRI and spectroscopy study in rat. Am J Physiol Heart Circ Physiol. 285(6): H2712-21 (2003)

Nahrendorf M, Hiller KH, Greiser A, Köhler S, **Neuberger T**, Hu K, Waller C, Ertl G, Haase A, Bauer WR, 2003. Magnetic resonance fusion imaging of chronic myocardial ischemia. Magnin et al. (Eds.) LNCS (Lecture Notes in Computer Science) 2674, FIMH (Functional Imaging and Modeling of the Heart) 2003: 272-277.

Invited Speaker:

"High field sodium imaging of rodents". 16.Feb 2006, International Symposium on Biomedical Magnetic Resonance Imaging and Spectroscopy at Very High Fields, Wuerzburg, Germany

"High resolution 23Na imaging at 17.6 T". 16.Oktober 2003, Wellcome Trust Center, Oxford, UK.

Abstracts

A.C. Ailiani, **T. Neuberger**, G. Banco, N. Barrie Smith, J.G. Brasseur, A.G. Webb *"Analysis of segmental gastrointestinal Motion in an Animal Model using dynamic MRI and Active Shape Models"* Proc. 15th ISMRM, # 626, Berlin, Germany 2007

T. Neuberger, V. Gulani, A.G. Webb *"Sodium Chemical Shift Imaging of induced Diuresis in a Mouse Renal Model"* Proc. 15th ISMRM, # 1328, Berlin, Germany 2007

T. Neuberger, K. Paralikar, X. Zhang, R.S. Clement, A.G. Webb *"Monitoring Brain Dimpling and Intracortical Micro-Electrode Arrays with High Resolution MRI in Rats"* Proc. 15th ISMRM, # 2352, Berlin, Germany 2007

T. Neuberger, A.G. Webb, J. Olczak, N McBrier *"Quantitative MRI analysis of skeletal muscle injury and regeneration in a rat hindlimb model"* Proc. 15th ISMRM, # 2665, Berlin, Germany 2007

T.Neuberger , E.Semouchkina, V.Tyagi, M.Lanagan, A.Baker, A.Webb *"Ceramic Dielectric Resonators for High-Field Magnetic Resonance Imaging"* Proc 48th ENC, oral , Daytona Beach, Florida, USA 2007

B.A Craven, **T Neuberger**, G.S. Settles, E.G. Patterson, E.M. Josephson, E.E. Morrison, A.G. Webb *"Morphometric Analysis of the Nasal Airway of the Dog from high resolution magnetic resonance microscopy, and implications regarding Olfactory Airflow"* Proc 48th ENC, #98 , Daytona Beach, Florida, USA 2007

V.M. Uppalapati, **T. Neuberger**, A. G. Webb *"Use of super-resolution algorithms for increasing S/N in multi-slice sodium imaging"* Proc 48th ENC, #105 , Daytona Beach, Florida, USA 2007

T. Neuberger , G. Melkus , H. Rolletschek , Markus Rokitta , A.G. Webb , P.M. Jakob , U. Wobus, L. Borisjuk, *"Crop Seed Magnetic Resonance Imaging at Very High Field strengths"*,International Symposium on Biomedical Magnetic Resonance Imaging and Spectroscopy at Very High Fields, Wuerzburg, Germany, 2006

T. Neuberger, A. Webb, *"High Resolution Sodium Imaging of Rat and Mouse Models of Stroke at 17.6 T"*, Proc. 14th ISMRM, #1473, Seattle/Washington, USA, 2006

T. Neuberger, A. Webb, *"Measurement of T1 relaxation times of major metabolites in the mouse brain at 11.7 and 17.6 Tesla using voxel-localized proton magnetic resonance spectroscopy",* Proc. 14th ISMRM, #1490, Seattle/Washington, USA, 2006

T. Weber, V. C. Behr, **T. Neuberger**, S. Aussenhofer, C. Faber, P. M. Jakob, *"Quantification of in vivo T1 relaxation times in rat spinal cord at 17.6 Tesla"*, Proc. 13th ISMRM, #2538, Miami/Florida, USA, 2005

T. Weber, **T. Neuberger**, M. Vroemen, N. Weidner, V. C. Behr, I. Wieland, U. Bogdahn, A. Haase, P. Jakob, C. Faber, *"In vivo and In vitro High Field Imaging of Rat Spinal Cord Injury"*, Proc. 12th ISMRM, #1529, Kyoto, Japan, 2004

T. Wichmann, D. Gareis, M. Griswold, **T. Neuberger**, S. Wright, C. Faber, A. Webb, P. Jakob. "A *Four Channel Transmit Receive Microstrip Array for 17.6T"*, Proc. 12th ISMRM, #1578, Kyoto, Japan, 2004

T. Neuberger, A. Greiser, A. Haase, P. M. Jakob, C. Faber, A. G. Webb. *"23Na Microscopy of the Mouse Heart In Vivo"*, Proc. 12th ISMRM, #1693, Kyoto, Japan, 2004

T. Neuberger, A. Stroh, P. Lorenz, F. Marschinke, A. Haase, P. M. Jakob, A. G. Webb, C. Zimmer, C. Faber. *„In Vivo Detection of Small Numbers of Magnetically Labeled Embryonic Stem Cells"*, Proc. 12th ISMRM, #1737, Kyoto, Japan, 2004

D. Gareis, **T. Neuberger**, V.C. Behr, C. Faber, M. Griswold, A. Haase, P. Jakob, *"2-Channel Transmit Receive Phased-Array-Coils for Multi-Channel Multi-Nuclei 1H, 23Na and 31P MRI and MRS at 17.6 T"*, Proc. ESMRMB, #274, Copenhagen, Denmark, 2004 (MAGMA 17(s):156f., 2004)

T. Weber, V. Gulani, **T. Neuberger**, A. G. Webb. *„A robust method for simultaneous rapid Diffusion Tensor and T2* measurements"*, Proc. ESMRMB, #286, Copenhagen, Denmark, 2004 (MAGMA 17(s):166, 2004)

T. Neuberger, V. Gulani, A. Webb. *„Three dimensional 23Na renal imaging of the mouse in vivo"*, Proc. ESMRMB, #406, Copenhagen, Denmark, 2004 (MAGMA 17(s): 240f., 2004)

D. Gareis, T. Wichmann, M. Griswold, **T. Neuberger**, S. Wright, C. Faber, A. Webb, P. Jakob. *„A four channel transmit receive microstrip array for 17.6T"*,

Proc. ESMRMB, #388, Copenhagen, Denmark, 2004 (MAGMA 17(s): 226f., 2004)

C. Faber, **T. Neuberger**, A. Stroh, P. Lorenz, C. Zimmer, P. M. Jakob, A. G. Webb. *„In vivo detection of small numbers of iron-labeled embryonic stem cells in the rat brain at 17.6 Tesla".* Proc. 45th ENC, #P13 – 307, Asilomar, USA, 2004

V.C. Behr, D. Gareis, M. Oechsner, **T. Neuberger**, D. Haddad, C. Faber, A. Haase, *"Resonator Designs for Very High Field 1H and X-Nuclei in-vivo and ex-vivo Microscopic MRI Experiments"*, Proc. 11th ISMRM, #2360, Toronto, Canada, 2003

T. Weber, **T. Neuberger**, A. Müller, G. Giegerich, U. Bogdahn, A. Haase, A. Steinbrecher, C. Faber. *„White Matter Lesion Load Quantification in Autoimmune Encephalomyelitis by High Resolution MR Microscopy of Rat Spinal Cord at 17.6 T"*, Proc. 11th ISMRM, #2318, Toronto, Canada, 2003

V.C. Behr, M. Oechsner, D. Gareis, I. Wieland, **T. Neuberger**, A. Haase, C. Faber, *"First Evaluation of Very High Field Multi-Channel Probes for Double-Resonant- and Quadrature-Detection at 17.6 T."*, Proc. ICMRM, Snowbird/Utah, USA, 2003

T. Weber, **T. Neuberger**, N. Weidner, M. Vroemen, A. Müller, G. Giegerich, U. Bogdahn, A. Haase, A. Steinbrecher, C. Faber, *"Imaging of Spinal Cord Disease Models in the Rat Post Mortem at 17.6 T."*, Proc. ICMRM, Snowbird/Utah, USA, 2003

A. Purea, D. Haddad, **T. Neuberger**, A. Haase, A.G. Webb, *"The effects of chemical fixation on intracellular NMR relaxation times"*, Proc. ICMRM, Snowbird/Utah, USA, 2003

A.G.Webb, L.Ciobanu, A.Purea, **T.Neuberger,** C. Pennington, *"Relative signal-to-noise efficiencies of phase- and frequency-encoding methods in NMR micro-imaging"*, Proc. ICMRM, Snowbird/Utah, USA, 2003

T. Weber, **T. Neuberger**, V.Behr, I. Wieland, U. Bogdahn, A. Haase, A. Steinbrecher, C. Faber, *"Central nervous system in vivo MR microscopy at 17.6 T"*, Proc. ICMRM, C-17, Snowbird/Utah, USA, 2003

V. C. Behr, I. Wieland, M. Oechsner, D. Gareis, T. Weber, **T. Neuberger**, A. Haase, C. Faber, *"An improved Probebase and Resonator Setup for in-vivo*

body MR Imaging of small mammals at 17.6 T", Proc. ICMRM, P-67, Snow-bird/Utah, USA, 2003

V. C. Behr, I. Wieland, M. Oechsner, D. Gareis, **T. Neuberger**, D. Haddad, A. Haase, C. Faber, *"Resonator Designs and Results for Microscopic in-vivo and ex-vivo MRI at Highest Field Strengths up to 17.6 T"*, Proc. ICMRM, P-68, Snowbird/Utah, USA, 2003

J.C. Tsai, T. Weber, **T. Neuberger**, A. Purea, V. Behr, A. Haase, A. Webb, *"High Field Magnetic Resonance Microscopy of Pig Cartilage"*, Proc. ICMRM, P-69, Snowbird/Utah, USA, 2003

T. Neuberger, H. Schneider, D. Haddad, A. Purea, M. Westhoff, A. Haase, U. Zimmermann, C. Faber, and A. Webb. *„NMR microscopy of the lipid distribution in air-dry branches of the resurrection plant Myrothamnus flabellifolia"* , Proc. ICMRM, P-67, Snowbird/Utah, USA, 2003

J.C. Tsai, T. Weber, **T. Neuberger**, A. Purea, V. Behr, A. Haase, A. Webb, *"High Field Magnetic Resonance Microscopy of pig cartilage"*, Proc. ESMRMB, #75, Rotterdam, Netherlands, 2003 (MAGMA 16(s):39, 2003)

Volker C. Behr, M. Oechsner, D. Gareis, I. Wieland, **T. Neuberger**, A. Haase, C. Faber, *"Multi-channel resonators for experiments at 17.6T"*, Proc. ESMRMB, #157, Rotterdam, Netherlands, 2003 (MAGMA 16(s):83, 2003)

Volker C. Behr, I. Wieland, M. Oechsner, D. Gareis, **T. Neuberger**, D. Haddad, A. Haase, C. Faber, *"Resonators for in-vivo and ex-vivo MRI at field strengths up to 17.6T"*, Proc. ESMRMB, #164, Rotterdam, Netherlands, 2003 (MAGMA 16(s):87f., 2003)

Volker C. Behr, I. Wieland, M. Oechsner, D. Gareis, T. Weber, **T. Neuberger**, A. Haase, C. Faber, *"An improved probebase and coil design for in-vivo body MRI of small mammals at 17.6T"*, Proc. ESMRMB, #165, Rotterdam, Netherlands, 2003 (MAGMA 16(s):88f., 2003)

T. Neuberger, A. Greiser, M. Nahrendorf, A. Haase, C. Faber, A. Webb. *„Improved High Resolution 23Na Imaging of the mouse heart"*; Proc. ESMRMB, #338, Rotterdam, Netherlands 2003

T. Weber, **T. Neuberger**, N. Weidner, M. Vroemen, V. Behr, I. Wieland, U. Bogdahn, A. Haase, C. Faber, *"In vivo MR imaging of spinal cord injury at 17.6 Tesla"*, Proc. ESMRMB, #410, Rotterdam, Netherlands, 2003 (MAGMA 16(s):216, 2003)

Nahrendorf M, Hiller KH, **Neuberger T**, Greiser A, Köhler S, Hu K, Haase A, Ertl G, Bauer WR, 2003. *„Fusion imaging in chronic coronary artery stenosis of the rat by phosphorus spectroscopy and magnetic resonance coronary angiography"*. J American College Cardiology 41 (6), Supplement A, Abstract 1075A-MP-207.

A. Greiser, **T. Neuberger**, S. Köhler, M. Nahrendorf, W. Bauer, M. Von Kienlin, A. Haase. *„1H Coronary Angiography and Quantitative Mapping of Reduced 31P Metabolites by 3D awCSI in a Coronary Artery Stenosis Model of the Isolated Rat Heart"*, Proc. 10th ISMRM, #688, Honolulu, Hawaii, 2002

A. H. Greiser, **T. Neuberger**, S. Aussenhofer, M. von Kienlin, C. Faber, A. Haase; *"Density-weighted 23Na Chemical Shift Imaging of the mouse heart at 17.6T"*, Proc. ESMRMB, #64, Cannes, France , 2002 (MAGMA 15(s): 27f., 2002)

T. Neuberger, A. Greiser, S. Aussenhofer, C. Faber, A. Haase; *"Density-weighted 23Na Chemical Shift Imaging of the rat brain at 17.6T "*,Proc. ESMRMB, #65, Cannes, France , 2002 (MAGMA 15(s): 28, 2002)

T. Neuberger, A. Greiser, S. Köhler, M. Nahrendorf, W. R. Bauer, M. von Kienlin, A. Haase; *"Fusion of quantitative 31P metabolite maps and 1H TOF Angiography in a coronary artery stenosis model of the isolated rat heart"*, Proc. ESMRMB, #228, Cannes, France , 2002 (MAGMA 15(s): 108, 2002)

T. Weber, **T. Neuberger**, C. Faber, A. Müller, G. Giegerich, U. Bogdahn, A. Steinbrecher, A. Haase; *„Lesion detection in autoimmune encephalomyelitis by high resolution MR microscopy of rat spinal cord at 17.6 T"* , Proc. ESMRMB, #386, Cannes, France , 2002 (MAGMA 15(s): 186, 2002)

T. Weber, **T. Neuberger**, C. Faber , A. Müller, G. Giegerich, U. Bogdahn, A. Steinbrecher,

A. Haase. *„ MR-Mikroskopie am Rattenhirn und –rückenmark bei 17,6T"*, Deutsche Sektion der ISMRM Jahrestagung 2002, Hamburg

Nahrendorf M, Hiller KH, **Neuberger T**, Greiser A, Köhler S, Hu K, Waller C, Haase A, Bauer WR, 2002. *„Fusionsbildgebung am Modell der chronischen Koronarstenose"*. . Zeitschrift für Kardiologie, 91 (Suppl. 1): 638.

Nahrendorf M, Hiller KH, **Neuberger T**, Greiser A, Köhler S, Hu K, Ertl G, Bauer WR, 2002. *„Fusion imaging in chronic coronary artery stenosis by magnetic*

resonance phosphorus spectroscopy and 3D coronary angiography". European Heart Journal 4 (suppl.): 175.

S Köhler, JUG Streif, V Herold, M Szimtenings, TE Lanz, M Nahrendorf, F Wiesmann, A Greiser, **T Neuberger**, E Rommel, C Waller, KH Hiller, WR Bauer, A Haase. *„Charakterisierung der Funktion von Kleintierherzen mit MR-Methoden".*

17. Physiologen / Kardiologen Workshop, Würzburg (2001)

J. Schneider, **T. Neuberger**, E. Fekete, T. Lanz, C. Weidensteiner, F. Fidler, S. Neubauer, A. Haase, M. von Kienlin. *„Simultaneous detection of phospho-creatin- and creatinsignal during hypoxia in isolated rat heart: an interleaved 1H/31P-study"*, Proc. ESMRMB, #207, Paris, France , 2000 (MAGMA 11(s): 79f., 2000)

T. Neuberger, A. Greiser, J. Schneider, C. Heindl, T. Lanz, A. Haase, M. von Kienlin. *„Fast absolute quantification of metabolite concentrations with slice-selective 31P MR spectroscopy in the perfused rat heart"*, Proc. ESMRMB, #208, Paris, France , 2000 (MAGMA 11(s): 80f., 2000)

<u>EHRENWÖRTLICHE ERKLÄRUNG</u>

Gemäß §5, Abs. 2, Ziff. 2 und 5
der Promotionsordnung der
Fakultät für Physik und Astronomie der
Universität Würzburg

Hiermit erkläre ich ehrenwörtlich, dass ich die vorliegende Dissertation selbständig und ohne die Hilfe eines kommerziellen Promotionsberaters angefertigt und keine anderen als die angegebenen Quellen und Hilfsmittel benutzt habe.
Die Dissertation wurde bisher weder vollständig noch teilweise weder einer anderen Hochschule noch in einem anderen Prüfungsfach mit dem Ziel, einen akademischen Grad zu erwerben, vorgelegt.

Würzburg, 24. Februar 2008

(Thomas Neuberger)